Reiwa 2nd academic year

Nagaoka University of Technology,

Graduate School of Engineering Academic Dissertation for

Doctor of Philosophy

Development of circular cylinder blade wind turbine driven by longitudinal vortex

（縦渦により駆動される円柱翼風車の開発）

Major: Science of Technology Innovation

Name: Kasumi NAKAJIMA

Student ID number: 14303886

Supervisor: Tsutomu Takahashi

ABSTRACT

The objective of this dissertation is to develop the practical circular cylinder blade wind turbine driven by the steady lift force of the longitudinal vortex. The mechanism of the driving force generation is demonstrated, and the rotation, output torque, and axial drag characteristics are investigated in the wind tunnel experiments. In addition, several methods for improving performance are investigated and the prediction method for performance is proposed.

In Chapter 1, the background and the outline in this dissertation are summarized. **In Chapter 2**, the structure and important parameters of the wind tunnel system and the cylinder blade wind turbine are described. The procedures of experiments and the measurement instruments are summarized. **In Chapter 3**, the process of formation and shedding of the necklace vortex (NV), which is one of longitudinal vortices, at the intersection of the rotating circular cylinder blade and ring-plate is observed by the smoke visualization. **In Chapter 4**, the effect of basic structural parameters on the rotational and torque characteristics of a single cylindrical blade wind turbine is investigated. A method to estimate the lift and drag coefficients acting in the direction of rotation of the cylindrical blade by the NV is proposed, and the performance of the wind turbine is predicted by these coefficients. **In Chapter 5**, the effect of the blade configuration of the stepped circular cylinder blade wind turbine on the rotation and torque characteristics is investigated, and the optimal installation conditions are clarified. By setting the effective length of the circular cylinder blade equal to the formation region of NV, the resistance to rotation is reduced without decreasing the lift force of the NV and the torque improved. When the pitch ratio t/d, which is normalized by blade diameter d for the pitch t between circular cylinder blades, is around $t/d = 2$, the lift force acting on per circular cylinder blade is maximized. **In Chapter 6**, the effects of the configurations and structural parameters of the rotating circular cylinder blade wind turbine on the axial drag characteristics are investigated. When the NV forms steadily, a large axial drag force acts in the mainstream direction at the same time. The axial drag coefficient shows a complex behavior for the continuous increase in the flow velocity. **In Chapter 7**, in order to enhance the performance of the circular cylinder blade wind turbine, the two different diameter ring-plates (dual ring-plates) are installed in the upstream of the circular cylinder blade and this effect is investigated. The optimum gap between the two ring-plates, which the maximum output torque is obtained, is determined as one-circular cylinder blade diameter. The dual ring-plate could be more effective for improving the performance at large N. **In Chapter 8**, the characteristics of rotation, torque and power, obtained from the experimental results in each chapter are summarized, and the basic knowledge for the application and improvement of drive systems powered by LVs, such as the cylinder blade wind turbines, is outlined.

List of contents

Nomenclature

A	Swept area of rotating cylinder blade [mm^2]
A_V	Cross-sectional area of necklace vortex [mm^2]
C_D	Total drag coefficient of effective region [-]
$C_{D.U}$	Axial drag coefficient [-]
C_L	Total lift coefficient [-]
C_{la}, C_{lb}	Coefficients for C_L [-]
C_p	Power coefficient [-]
C_z	Fluid force coefficient [-]
d	Diameter of cylinder blade [mm]
d'	Diameter of supporting rod [mm]
D	Center diameter of ring plate [mm]
D_{large}	Diameter of outside ring-plate of dual ring [mm]
D_{small}	Diameter of inside ring-plate of dual ring [mm]
D_v	Equivalent diameter of the cross-section of a Necklace vortex
F_{drag}	Drag force by fluid resistance [N]
F_{fric}	Mechanical friction force [N]
F_{NV}	Lift force by necklace vortex [N]
F_N	Fluid force [N]
$F_{D.U}$	Axial drag force [N]
l	Effective length of cylinder blade [mm]
l'	Length of supporting rod [mm]
l_{drag}	Spanwise length of occurring region of fluid resistance [mm]
l_F	Separation length of two flanges [mm]
l_{NV}	Spanwise length of shedding region of necklace vortex [mm]
l_P	Protruding length of cylinder blade from ring-plate rims [mm]
l_{total}	Total length of cylinder blade [mm]
m	Total mass of cylinder blade, hub, and driving shaft [kg]
m_{blade}	Mass per stepped cylinder blade [kg]
m_{shaft}	Mass of hub and driving shaft [kg]
n	Rotational speed of cylinder blade [rpm]
n_{max}	Maximum rotational speed at loaded experiments [rpm]
n_{min}	Minimum rotational speed at loaded experiments [rpm]
N	Number of blades [-]
R	Radius of ring-plate [mm]

r_{drag}	Distance between the acting point of resistance force of effective region and the rotation axis [mm]
$r_d{}'$	Distance between the acting point of resistance force of supporting rod and the rotation axis [mm]
r_{NV}	Distance between the acting point of driving force of effective region and the rotation axis [mm]
r_{shaft}	Radius of driving shaft [mm]
Re	Reynolds number [-]
s	Gap between upstream and downstream bodies [mm]
t	Installation interval between cylinder blades [mm]
T_{brake}	Load torque [N·m]
T_{drag}	Fluid resistance torque [N·m]
T_{fric}	Friction torque [N·m]
T_{NV}	Driving torque [N·m]
T_z	Cross flow torque [N·m]
U	Flow velocity [m/s]
U_{min}	Minimum velocity for rotation [m/s]
U_{start}	Calculated minimum velocity for rotation [m/s]
V	Rotational velocity of cylinder blade [m/s]
VR	Velocity ratio of upstream cylinder in numerical simulation [-]
W	Width of ring-plate [mm]
W_{ring}	Gap between ring-plates [mm]
α	Relative attack angle [deg]
λ	Velocity ratio of upstream cylinder blade [-]
λ_{ope}	Operating velocity ratio of cylinder blade in loaded experiments [-]
μ	Friction coefficient [-]
ρ	Density of air at 20°C [kg/m^3]
ω	Angular velocity [rad/s]

1. Introduction

The importance and trends of wind power generation in renewable energy will be explained, and the many types of wind turbines and each application will be shown. The innovative research on wind turbines in Japan and Japan's world-leading offshore wind power generation will be summarized. The mechanism of vortex shedding that appears in the downstream of a blunt body placed in a uniform flow is introduced. The vortex-induced vibration that occurs when a blunt body is elastically supported, a serious accident which was occurred by the vortex-induced vibration, and several techniques of suppression and control the vortex shedding are reviewed. The passive method of fluids engineering laboratory in Nagaoka University of Technology by adding a secondary body such as the circular cylinder or the strip-plate to downstream in cruciform arrangement is introduced regarding the applications of the longitudinal vortex (LV) that suppresses or induces vibration. A conversion mechanism of the periodic formation of the LV to the steady formation in a certain direction is explained and the process of development and the characteristics of an innovative wind/water turbine driven by the steady lift force of the LV is desribed. The numerical study is carried out to clarify the mechanism of steady formation of the LV and the generation of steady lift force is reviewed. The objectives of this research work and the outline of each chapter are presented.

1.1 Wind power generation

1.1.1 Background

The use of wind has a history of thousands of years. Since the oil crisis of the early 1970s, wind power technology has transitioned from a low-level experimental technology primarily used to charge batteries to mainstream of power technology in just two decades. Today, wind power has become one of the fastest growing renewable energy sources. Wind power is cost-free and infinite. The cost of electricity generated by wind is comparable to the cost of electricity generated by conventional fossil-based power plants [1]. The global wind power reached 650.8GW by the end of 2019 and covered 6% of the world's total electric power demand, which is equivalent to more than the annual electric power demand of Japan. China, the United States, and Germany were the top list and these three countries accounted about half of the world's total adoption. In Japan, the Ministry of Economy, Trade and Industry (METI) has assumed an installed capacity of about 10GW by 2030, and the actual installed capacity of wind power in Japan at the end of 2019 was 3.9GW [2,3]. The wind power produces 2.4% of the total electricity in Europe. The EU's decision to make the wind power a major source of electricity has explicitly stated that it will gain 12% market share by 2020 and 20% by 2030 [1]. Also, WindEurope, the Europe-based business organization for wind power industry, explicitly stated at the international conference "Offshore 2019" in Copenhagen in November 2019 that it will increase European offshore wind power capacity to 450 GW by 2050, providing 30% of total electric power demand in Europe [4,5].

1.1.2 Types and characteristics of wind turbines

As shown in Fig. 1-1, wind turbines are classified into two main types according to the direction of the rotation axis: the horizontal axis type and the vertical axis type. In addition, based on the rotating principle and the mode of generating torque, wind turbines are classified into two types: the lift type, which uses the lift force acting on the blades of the wind turbine, and the drag type, which uses the drag force. The drag type wind turbines rotate at a circumferential speed below the mainstream speed acting on the wind turbine, whereas the lift type wind turbines rotate at a higher circumferential speed, which is more than twice the mainstream speed [6]. Fig. 1-2 summarizes the types of wind turbines and their applications [7]. The characteristic coefficients used to evaluate the performance of various wind turbines include the power coefficient, torque coefficient, and tip speed ratio as shown in Fig. 1-3. Propeller type wind turbines and Darrieus type wind turbines have a small torque coefficient but a large power coefficient, and they are suitable for high speed and low torque power generation. On the other hand, Savonius and multiblade type wind turbines have a small power coefficient but a large torque coefficient. They are low speed and high torque types suitable for driving a pump and other applications.
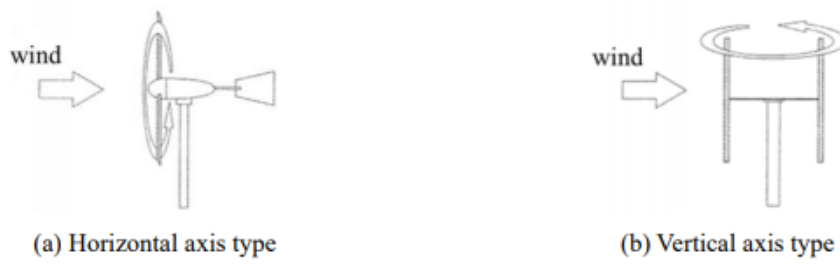
10

(a) Horizontal axis type

(b) Vertical axis type

Fig. 1-1 Categorization by direction of rotation of wind turbine [6].
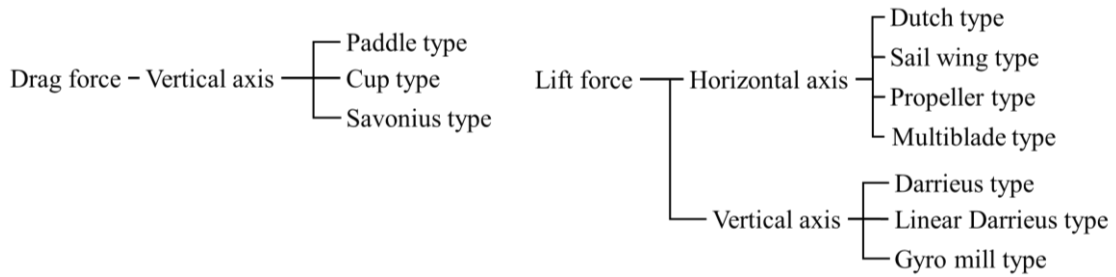
Fig. 1-2 Categorization of various wind turbines [7].
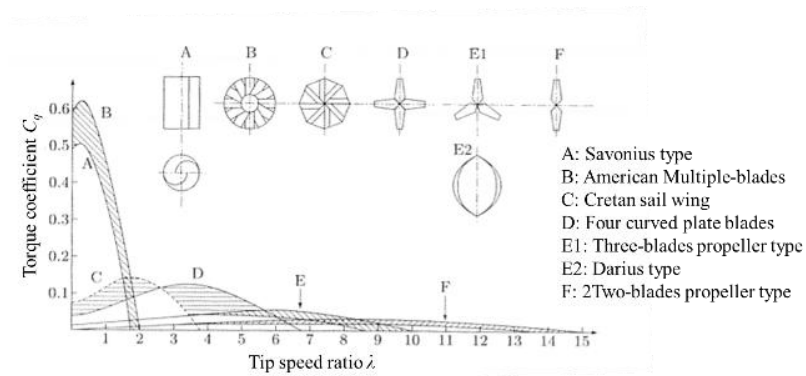
(a) Torque coefficient
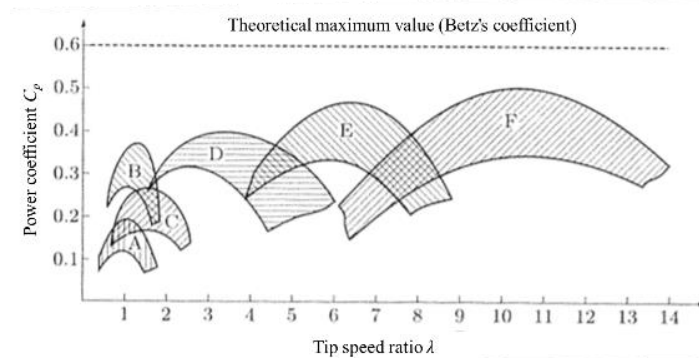
(b) Power coefficient

Fig. 1-3 Performance of various wind turbines [7].

11

1.1.3 Recent studies

As the energy self-sufficiency rate of Japan is low, accelerated expansion of renewable energies is extremely important. Wind power generation can be used wherever the wind blows, and it can be built inexpensively, even in Japan's mountainous terrain. Furthermore, in Japan, which is surrounded by the sea, the floating offshore wind power generation, which the wind turbines are installed over the ocean, is leading the world.

The studies on wind turbines in Japan are described in this section. Fig. 1-4(a) shows a wind turbine with a diffuser with a brim at the outlet, called "wind lens". The purpose of this brimmed diffuser is to increase the wind speed since the electric power generation is proportional to the third power of the wind speed. The vortex-forming plate called "brim" attached to the outside of the outlet of the diffuser generates a low-pressure section near the diffuser outlet by its strong vortex formation, and the wind flows into the low-pressure section. And a large speed-up effect is achieved near the diffuser inlet [8]. A significant increase in wind speed and power has been achieved by optimizing the shape of the diffuser [9]. The wind tunnel experiments were conducted on the vortex stabilization plates placed on the outer surface of the diffuser and the various shapes of brims, and the effect on the power coefficient was investigated [10]. This wind-lens wind turbine is already in use as a human- and environment-friendly wind turbine. It can be installed in any location, and has been installed in parks and along roadsides, as well as a 25-kW mini-wind farm, as shown in Fig. 1-5 [11].

(a) Prototype wind turbine (500 W class)   (b) Effect of power coefficients
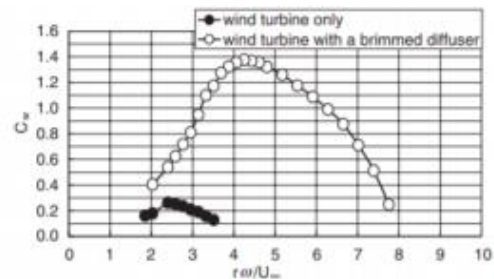
Fig. 1-4 The wind turbine with a brimmed diffuser shroud [9].

Fig. 1-5 Wind farm of wind turbines with a brimmed diffuser at Kyushu University [11].

A vertical axis wind turbine called "butterfly wind turbine (BWT)" is shown in Fig. 1-6. This is a vertical axis type wind turbine that has a butterfly wing shape, and the blades have an airfoil cross-section. In addition, BWT has the looped blades, there are no arms or blade tips which are inevitable for the vertical axis type wind turbines with conventional straight blades. This simple blade shape and structure significantly reduces noise and fluid resistance. The effect of the cross-sectional shape of the blade on the power characteristics of a micro-BWT with a small profile of 0.4m in diameter and 0.3m in height was investigated. The cambered airfoil with the blade warped to follow the curvilinear flow formed by rotation produced a higher power compared to symmetrical airfoils [12]. In addition, a method to control the increase in rotational speed at high wind speeds by providing an over-speed control system with the blades was developed. At low rotational speeds, the looped blades rotate so that the vertical portion of each blade is perpendicular to the flow. When the rotational speed exceeds a certain value, centrifugal force twists the blades, as shown in Fig. 1-6(b) [13]. Fig. 1-7 shows a comparison of the theoretically predicted electric power for the BWTs with a radius of 3.5m with and without an over-speed control system. The electric power with an over-speed control system was almost the same up to 10m/s as that without the system and became lower at higher wind speeds. However, it was predicted that a wind turbine could generate about 3kW of power with a system even at a wind speed of 13m/s or higher when the wind turbine without a system stopped. This over-speed control system will lead the improvement of the operating rate and reduce the cost of wind turbines.

(a) no-twist state   (b) twist state (η=30deg)
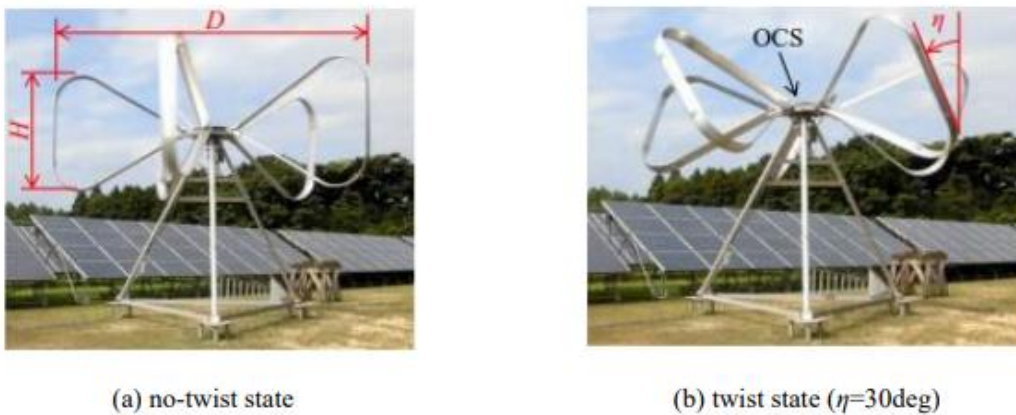
Fig. 1-6 Prototype of the butterfly wind turbine (BWT) equipped with an over-speed control system for 5 looped blades [13].
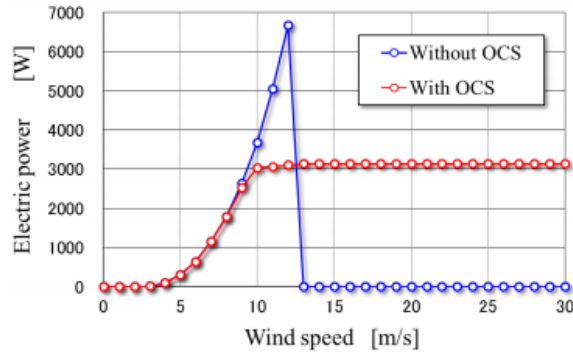
Fig. 1-7 Comparison of power between the BWTs with and without the over-speed control system [13].

The potential of offshore wind energy around Japan is large because of the wide distribution of suitable coastal areas (annual average wind speed of 7m/s or more). On the other hand, there are some problems, such as the cost of construction and maintenance management due to the small number of offshore wind turbine plant that have been installed, and the methods of environmental impact assessment have not been established. Currently, New Energy and Industrial Technology Development Organization (NEDO) is taking the lead in promoting offshore wind power generation in Japan. The development and research on offshore wind power generation facilities and offshore observation towers were conducted off the coast of Choshi, Chiba Prefecture on the Pacific side and off the coast of Kitakyushu City, Fukuoka Prefecture on the Sea of Japan sides in order to develop technologies for the design, construction, operation and maintenance of offshore wind power generation and environmental impact assessment, considering the meteorological and oceanographic conditions in Japan. Because the condition for offshore in Japan is different from those in Europe, the leading country in offshore wind power generation. The experimental facility off the coast of Choshi is shown in Fig. 1-8. The design and construction techniques of offshore wind turbines, observation towers and their foundations were developed and researched for the area off Choshi, which is subject to severe waves, and the area off Kitakyushu City, which is subject to strong typhoons. After the operation of the wind power generation facility, development and research were carried out on operation and maintenance techniques of wind turbines and observation towers, as well as methods for analyzing observation data [14].

Fig. 1-8 Demonstration facility of offshore wind turbine in off the coast of Choshi [14].

1.2 Vortex and vortex-induced vibration

1.2.1 Karman vortex street

When a blunt body such a circular cylinder is set in a uniform flow, the alternating flow separation on both surfaces of the body occurs and the vortex pattern appears in the downstream. This phenomenon is well known as the "Karman vortex street", and an example of visualization is shown in Fig. 1-9 [15].

The vortex shedding frequency f_v of the Karman vortex street for the circular cylinder is proportional to the flow velocity U and, is inverse to the cylinder diameter d. The dimensionless parameter of the vortex shedding frequency is well known as the "Strouhal number $St = f_v d/U$". Fig. 1-10 shows the relationship between the Strouhal number and the Reynolds number $Re = \rho dU/\mu$ for the circular cylinder [16]. The Strouhal number keeps an almost constant value as $St \simeq 0.2$ regardless the Reynolds number over the range of $200 < Re < 10^5$. By the value of the Reynolds number, the flow form and characteristic, Strouhal number, drag coefficient, and separation angle were changed as presented in Table 1-1 [17]. The alternative formation of the Karman vortex from both sides of the body generates the fluid force perpendicular to the flow acting on the body periodically, and cause vibration and sound. Several examples of the phenomena are sound from an electric wire in the flow, or the wind noise from a swung thin rod.
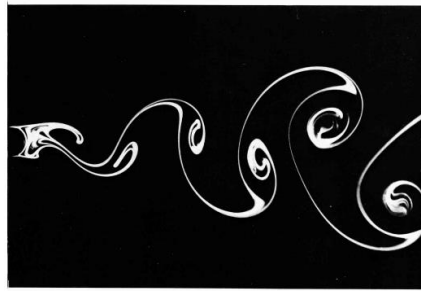

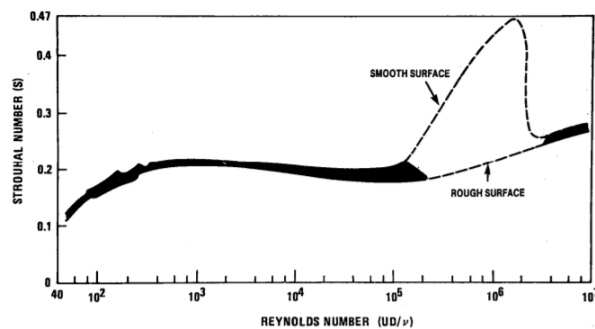Fig. 1-9 Karman vortex street behind a circular cylinder at $Re = 140$ [15].

Fig. 1-10 Relationship between Strouhal number and Reynolds number for a circular cylinder [16].

15

Table 1-1 Flow regimes at a circular cylinder (incompressible flow) [17].

Reynolds number regime	Flow regime	Flow form	Flow characteristic	Strouhal number Sr	Drag coefficient c_D	Separation angle Θ_S
$Re \rightarrow 0$	Creeping flow		Steady, no wake	–	see Fig. 1.12	–
$3-4 < Re < 30-40$	Vortex pairs in wake		Steady, symmetric separation	–	$1.59 < c_D < 4.52$ (Re = 30) (Re = 40)	$130° < \Theta_S < 180°$ (Re = 35) (Re = 5)
$\frac{30}{40} < Re < \frac{80}{90}$	Onset of Karman vortex street		Laminar, unstable wake	–	$1.17 < c_D < 1.59$ (Re = 100) (Re = 30)	$115° < \Theta_S < 130°$ (Re = 90) (Re = 35)
$\frac{80}{90} < Re < \frac{150}{300}$	Pure Karman vortex street		Karman vortex street	$0.14 < Sr < 0.21$		
$\frac{150}{300} < Re < \frac{10^5}{1.3 \cdot 10^5}$	Subcritical regime		Laminar, with vortex street instabilities	$Sr = 0.21$	$c_D \approx 1.2$	$\Theta_S \approx 80°$
$\frac{10^5}{1.3 \cdot 10^5} < Re < 3.5 \cdot 10^6$	Critical regime		Laminar separation Turbulent reattachment Turbulent separation Turbulent wake	No preferred frequency	$0.2 < c_D < 1.2$	$80° < \Theta_S < 140°$
$3.5 \cdot 10^6 < Re$	Supercritical regime (transcritical)		Turbulent separation	$0.25 < Sr < 0.30$	$c_D \approx 0.6$	$\Theta_S \approx 115°$

1.2.2 Vortex-induced vibration and wake control

By the periodically shedding of the vortex, both fluctuating lift and drag force acts on the blunt body. The amplitude of the fluctuating lift force is larger than that of the drag force. In particular, the amplitude of lift force is large and when the blunt body is elastically supported so that it can vibrate perpendicular to the flow, i.e., in the cross-flow direction, a large vibration is generated when the frequency of the lift force coincides with the natural frequency of the blunt body. This phenomenon is well known as "Vortex-Induced Vibration: VIV" and it causes the serious accidents. A typical example of an accident by the VIV is the collapse of the Tacoma Narrows Bridge on the west coast of the United States in 1940 (Fig. 1-11). This accident was triggered by the "Karman Vortex-Induced Vibration: KVIV" of the bridge which induced a torsional flutter, and the bridge collapsed at a small flow velocity (19m/s) well below the design limit [18].

The VIV has caused not only the above example but also many accidents. Many researchers have focused on control the wake and vortex suppression. As an example, VIV is suppressed by attaching a piece of additional equipment to the upstream cylinder body without external energy as shown in Fig. 1-12 [16]. This is called passive methods. On the other hand, in active method, the vortex street is controlled by the external energy such as jet injection or suction flow in Fig. 1-13 [19], plasma control in Fig. 1-14 [20], and thermal effect [21].
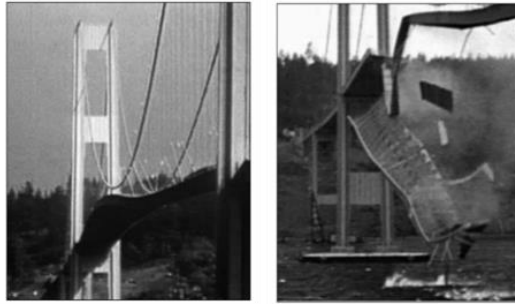
Fig. 1-11 Collapse of Tacoma Barrows Bridge [18].
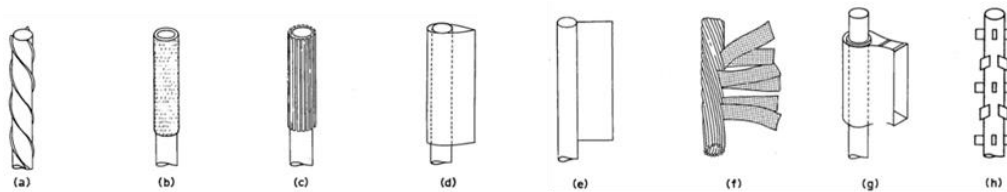
Fig. 1-12 Add-on devices for suppression of vortex induced vibration of cylinders: (a) helical strake; (b) shroud; (c) axial slats; (d) streamlined fairing; (e) splitter; (f) ribboned cable; (g) pivoted guiding vane; (h) spoiler plates [16].
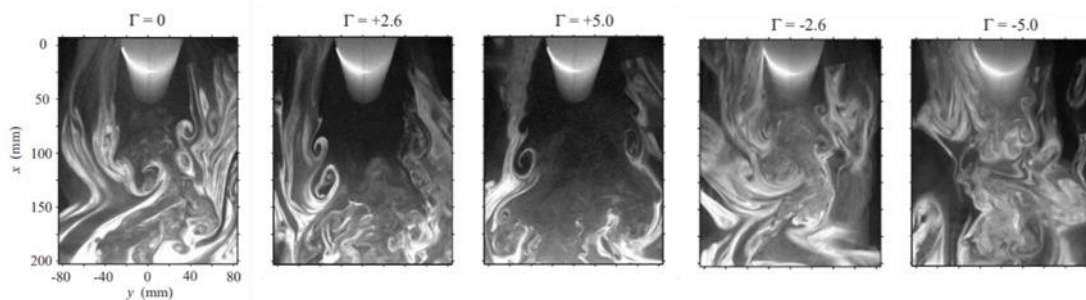
Fig. 1-13 Instantaneous flow visualization images in wake of a porous cylinder subject to continuous suction or blowing for $Re = 3300$. Γ is suction and blowing rates $\Gamma = 100(V/U_\infty)$, where V is velocity through the porous cylinder negative for suction and positive for blowing, and U_∞ is oncoming streamwise velocity [19].
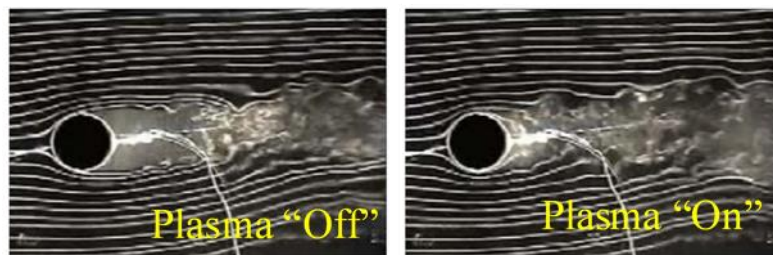
Fig. 1-14 Wake control by applying plasma actuation [20].

1.2.3   Longitudinal vortices and their control

The author's group investigated a passive method of suppressing VIV by placing another object in the downstream of the upstream cylinder body without contacting. The KVIV was effectively suppressed by employing a secondary cylinder body placed behind the upstream cylinder in a cruciform arrangement with a certain gap [22]. The Karman vortex street disappears due to the arrangement of the secondary structure in the downstream, but a necklace type or trailing type vortex is formed near the intersection. The formation of these longitudinal vortices (LVs) and their shapes in the cruciform two-cylinders system have been reported [23, 24, 25]. Fig. 1-15 shows a schematic diagram of trailing vortex (TV) and necklace vortex (NV) in the circular-cylinder/strip-plate system which the downstream circular-cylinder is plated to the strip-plate [26]. It has also been reported that the LVs are formed in the same way in a rectangular-cylinder/strip-plate system which is replaced the upstream circular-cylinder with a rectangular-cylinder and the downstream circular-cylinder with a strip-plate [27].

The LVs formed in the cruciform system fixed in a uniform flow alternate formation and disappearance at diagonally backwards of upstream cylinder body, like Karman vortex street. These formation and disappearance of the LV is highly periodic, and its frequency is affected by the flow velocity and shape factor. The LVs in Fig. 1-15 are formed in the upper part of the diagonal backward direction of the upstream cylinder. In the next instant, a LV is formed at a symmetrical position with respect to the horizontal plane including the central axis of the cylinder, i.e., the lower part of the diagonal backward. A fluctuating lift force acts on the upstream cylinder body synchronously with the formation and disappearance of the LV, and this vibration force is greater than the fluctuating lift force due to the periodic shedding of Karman vortex street. The author's group found that the phenomenon of vibration by LVs, or "longitudinal vortex-induced vibration: LVIV", occurs when a upstream cylinder body is elastically supported so that it can move perpendicular to the mainstream (cross-flow) direction [28,29,30]. The VIV is a resonance phenomenon that occurs when the natural frequency of the system coincides with the shedding frequency of the vortex. Since the shedding frequency of the Karman vortex street is proportional to the flow velocity, the KVIV occurs only in a narrow range of flow velocity where the two frequencies have coincided each other. The power generation system VIVACE using Karman vortex induced vibration covers the narrow range of flow velocity range where KVIV occurs by targeting the flow with small velocity fluctuations such as ocean currents [31]. For the practical application of the KVIV power generation, methods such as to actively control the natural frequency to match the vortex shedding frequency is considered, these methods have complicated structures and have problems with cost and durability. The shedding frequency of the LV increases as the flow velocity increases, and thus the oscillation phenomenon due to the resonance occurs in a specific flow velocity region, but the three-dimensional structure of the LV changes autonomously and the shedding frequency matches the natural frequency of the system and the oscillation continues even if it deviates greatly from the original resonant flow velocity. Although, phenomenon is also observed in KVIV, the synchronous velocity range of the LVs is much wider than that of Karman vortices, and the range is

extended to tens-times in the case of circular-cylinder/strip-plate systems [29]. The authors' group presented a LVIV power generation system that uses advantage of the strength of the vibration force, the wide range of synchronous flow velocity and the simplicity of the structure [32]. This power generation system does not require complex mechanisms and enables power generation over a wide range of flow velocities, which is advantageous for the practical application of VIV power generation.
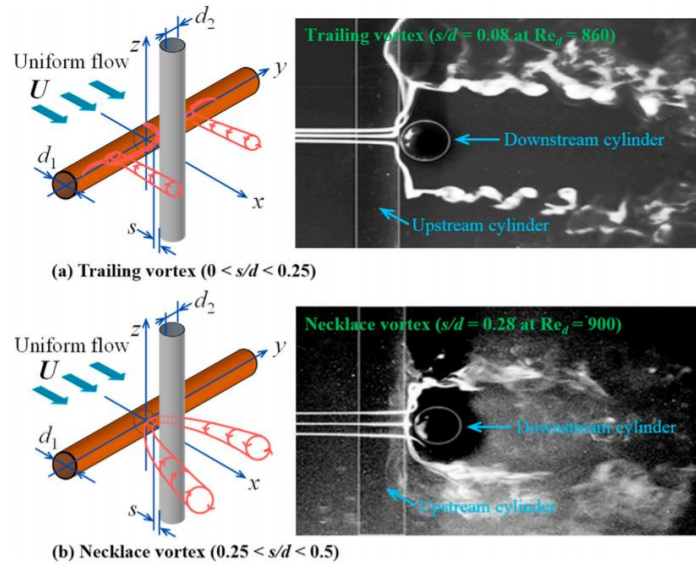
Fig. 1-15 Configurations of adding a secondary cylinder in downstream in cruciform arrangement, and visualization of the longitudinal vortices [26].

1.2.4 Steady lift force generation by longitudinal vortex

The LV gives a very strong vibration force to the upstream cylinder, and periodically forms and disappears diagonally behind the upstream cylinder in the gap with the downstream cylinder body, similarly to the Karman vortex. The LV causes a fluctuating lift force acting on the upstream cylinder body which is time-averaged to zero, i.e., no steady lift force is generated. Therefore, the LVs do not act as a power source to move the cylinder body in one direction only. Our research group got the idea to use the LV that generate the strong excitation force to exert a steady lift force on the upstream cylinder body, particularly on the circular cylinder, and successfully stabilized the LV at a certain position. We proposed a new driving system of wind turbine shown in Fig. 1-16 as an example of their results [33, 34]. As a method of stationary formation of the LV on one side of the cylinder in order to obtain a steady lift force, giving a relative attack angle to the flow field was focused. When the upstream cylinder moves in parallel along with the downstream strip-plate at a constant speed, the flow field around the cylinder has a relative attack angle, and the LV stationary forms on the opposite side of the moving direction. In the wind turbine apparatus, in order to maintain continuous movement in one direction, the cylinder was fixed to the driving shaft at the center of the

spanwise length and was enabled rotation. The strip-plate was replaced with a ring-shaped flat plate having a width W. The motion of the cylinder blade wind turbine with a width ratio of $W/d = 1$ was confirmed by a wind tunnel experiment with a constant flow velocity of $U = 10$m/s. When the gap ratio was $s/d \geq 0.325$, the cylinder blade rotates continuously in the initial direction.

This cylinder blade wind turbine is consisted by simple shaped parts such as a circular cylinder and a ring-plate and is easier to manufacture and more robust than the conventional propeller type wind turbine. This wind turbine has been miniaturized and enlarged as shown in Fig. 1-17 by our research group, and continuous rotation has been confirmed.

(a) Photograph of structure

(b) Schematic diagram and each parameter
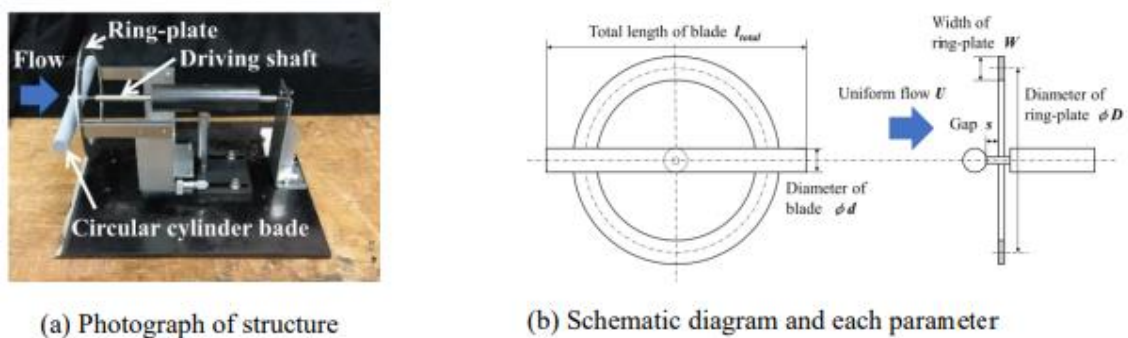
Fig. 1-16 Photograph of trial test instrument of new turbine with circular cylinder blade. $d = 20$mm, $l_{total} = 220$mm, $W = 20$mm, $D = 155$mm, $s = 7$mm ($s/d = 0.35$) [34].

Fig. 1-17 Miniaturized cylinder blade wind turbine.

In order to confirm the phenomenon of the stationary formation of the LV by the motion of the upstream cylinder and the generation of lift force due to it, the flow field around the cylinder which constantly rotates or translates, and the lift force acting on the cylinder were investigated by numerical calculation [35].

For a cruciform cylinder/strip-plate system, when the cylinder translates in the spanwise direction of the strip-plate at a constant speed, both NV and TV form near the intersection as shown in Figs. 1-18 and 1-19. In particular, the NV which stationary forms behind the moving direction of the cylinder induced a strong

suction (negative pressure) region in front of the cylinder and generated the driving force (lift force) to the cylinder [36]. Using this cruciform cylinder/strip-plate system, the aerodynamic characteristics around the cylinder and the effects of the structural parameters of the wind turbine such as the gap ratio s/d, width ratio W/d, and protrusion length ratio l_e/d were investigated. The distribution of fluid force and pressure around the cylinder each experimental condition was investigated, and it is concluded that combination of structural parameters of s/d = 0.3-0.4, W/d = 1.5-2.5, and l_e/d = 1.5 in Fig. 1-20 was the most effective for the lift force formation [35]. In order to improve the lift force acting on the cylinder, the end plates of several shapes were attached to the free end of the cylinder and evaluated their effect. For the evaluation, the conditions of W/d = 1 and the cylinder length ratio of l/d = 4 which is generated a negative lift force against to the moving direction shown in Fig. 1-21 were used, and a pair of circular end plates of $d_e > d$ and semi-circular end plates having a rectangular bent at downstream were attached. It was shown that the attachment of the semi-circular end plate improved the negative lift force, whereas the circular end plate did not. The dimensionless number of end plate diameters was recommended to be d_e/d = 2.5 [36].

In the Longitudinal Vortex Wind Turbine: LV-WT model, numerical calculations are conducted using same structure and parameters of the actual cylinder blade wind turbine in the wind tunnel experiment, the calculation results coincided well with the experimental results [37]. In addition, in order to improve the efficiency characteristics of the wind turbine, the unnecessary regions on the cylinder blade where negative lift force is generated were removed, and the three-dimensional effect of LV was evaluated [38].
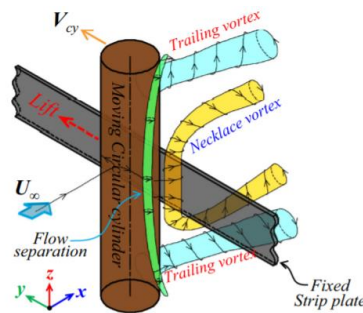
Fig. 1-18 Schematic diagram of the LVs near crossing of a moving cylinder with a fixed strip-plate set downstream in cruciform arrangement. The cylinder is moving on the y-axis (in depth direction), and the NV and TV form on the opposite direction (in front direction) of the moving of the cylinder [36].
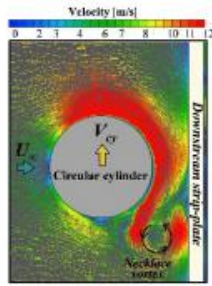
(a) Velocity vector field around circular cylinder   (b) Pressure contour
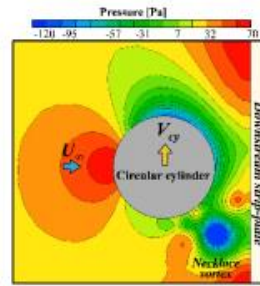
Fig. 1-19 Visualization of the NV on the plane of symmetry ($z = 0$ cross-section) for circular-cylinder/strip-plate system with $d = 20$mm, $l/d = 4$, $W/d = 1$, $s/d = 0.35$ at $U = 10$m/s when the upstream cylinder is moving with velocity V_{cy} parallel to the strip-plate. The velocity ratio $VR = V_{cy}/U = 0.1$ [36].
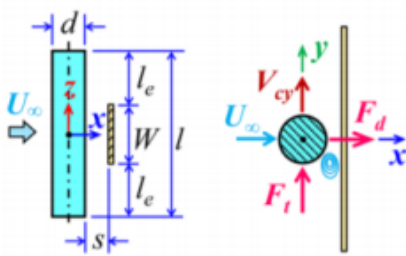
Fig. 1-20 Relevant parameters for CFD simulation [35, 36].
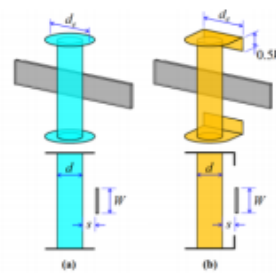
Fig. 1-21 Tip-end configurations: (a) circular endplate; (b) semi-circular plate with a rectangle bent 90° downward in the downstream [36].

1.3 Objectives of study

The objective of the research work is to develop a cylinder blade wind turbine which is driven by steady lift force of the LV and rotates steadily. The wind tunnel experiments are carried out to investigate the rotation, output torque, and performance characteristics of a cylindrical blade wind turbine, which are still largely unknown at this stage. The purpose of major experiments and contents are shown below.

1. The characteristics of stational forming and shedding of the LV are investigated by the visualization of the NV near the intersection and measuring the axial drag force acting on the cylinder blades.

2. By the evaluations of the rotational speed at free-rotating conditions without load to the driving shaft, and the output torque and power at loaded condition, the influence of the basic structural parameters of a cylindrical blade wind turbine are investigated.

3. The effects of multi-blade and blade configuration on the steady formation of LVs are elucidated, and guidelines for improving the performance of cylinder blade wind turbines is obtained.

4. The dual ring-plate is installed to the cylinder blade wind turbine as a new idea to improve the performance, and the installation conditions of the dual ring-plate and cylinder blades are optimized.

Based on the above research results, the guideline for the practical application of cylinder blade wind turbines is obtained and the basic knowledge for further applications and performance improvement of new driving systems powered by LVs is clarified. In addition, the performance characteristics, advantages and problems are compared with those of the conventional wind turbines, and the status of cylinder blade wind turbines in the field of wind power and wind turbines is identified.

1.4   Organization of dissertation

This dissertation consists of eight chapters and main contents of each chapter are existed as follows:

Chapter 1 Introduction

The vortex shedding and vortex induced vibration, and their suppression and control methods were described. The research work on steady lift force by LV in our research group were introduced with some examples. The objectives of the study were clarified.

Chapter 2 Experimental conditions and procedures

The structure and important parameters of the wind tunnel system and the cylinder blade wind turbine are described. The procedures of experiments and the measurement instruments are summarized.

Chapter 3 Visualization of longitudinal vortex

The cross-section of NV at the intersection of the cylinder blade and the ring-plate are observed by the smoke and the effect of the installation conditions of cylinder blades are evaluated.

Chapter 4 Basic characteristics of the single circular cylinder blade wind turbine

The effects of basic structural parameters on the rotational characteristics and output torque characteristics are investigated. The method for estimating the lift coefficient by NV and the drag coefficient against the rotational motion is proposed and the performance of the wind turbine is predicted by above coefficients.

Chapter 5 Effect of blade configurations of the stepped circular cylinder blade wind turbine

Using the stepped cylinder blade wind turbine in which unnecessary regions of the cylinder blade for formation of LVs are removed, the effect of cylinder blade configuration such as effective length, number, and diameter on rotation and output torque characteristics is evaluated. Based on the visualization results in Chapter 3, the optimum condition for maximizing the performance is determined.

Chapter 6 Axial drag force in mainstream direction

The characteristics of axial drag acting in the mainstream direction is investigated by varying the structural parameters of the cylinder blade and the experimental conditions. The effect of stepped cylinder blades on reducing of the axial drag force is evaluated.

Chapter 7 Effect of ring-plate configuration on the performance enhancement

Based on the inference that the performance improves as the number of forming of NVs increases, the dual ring-plate with different center diameters is attached downstream of the cylinder blade and its effect is evaluated. The optimum value of the distance between two ring-plates and the effect of blade number are investigated.

Chapter 8 Conclusions

The characteristics of rotation, output torque, and power, obtained from the experimental results in each chapter are summarized, and the basic knowledge for the application and improvement of drive systems powered by LVs, such as the cylinder blade wind turbines, is clarified. The status of cylinder blade wind turbine in field of the wind power generation and its prospects are discussed.

References

[1] Munteanu, I., Bratcu, A. I., Cutululis, N. A., Ceanga, E., 2008. Optimal Control of Wind Energy Systems, Springer Verlag, Berlin Germany, pp.1-7.

[2] Press Releases of WWEA, 2020. World wind capacity at 650.8 GW, Corona crisis will slow down markets in 2020, renewables to be core of economic stimulus programmes,

https://wwindea.org/blog/2020/04/16/world-wind-capacity-at-650-gw/ (accessed November 26, 2020)

[3] 日本経済新聞, 2019. 欧州の洋上風力, 2050 年に現在の 20 倍「達成可能」,

https://www.nikkei.com/article/DGXMZO52652120W9A121C1TJC000 (accessed November 26, 2020)

[4] 日経クロステック, 2020. 主役は陸上から海上に, 風力版の北海油田計画も,

https://xtech.nikkei.com/atcl/nxt/column/18/01267/00053/ (accessed November 26, 2020)

[5] RECHARGE, 2019. The official show dailies Day one, Press release of international conference of WindEurope Offshore 2019,

https://windeurope.org/offshore2019/media-and-press/recharge-dailies/ (accessed November 26, 2020)

[6] 牛山泉, 2013. 風車工学入門 第 2 版-基礎理論から運用のノウハウまで, 森北出版株式会社, pp. 1-5, 46-65.

[7] Yamamoto, M., Oota, Y., Niizeki, Y. and Miyagawa, K., 2018. Fluid machinery -From fundamental theory and applications-, Kyoritsu Shuppan Co., Ltd, pp.197-205 (In Japanese).

[8] Ohya, Y., Hasegawa, M., Iba, S., Karasudani, T., Watanabe, K., 2006. Development of a Shrouded Wind Turbine Equipped with a compact brimmed diffuser, Proceedings of the 19th Wind Engineering Symposium, pp.163-168.

[9] Ohya, Y., Karasudani, T., Sakurai, A., Inoue, M., 2006. Development of a high-performance wind turbine equipped with a brimmed diffuser shroud, Transactions of the Japan Society for Aeronautical and Space Sciences, Vol. 49, Issue 163, pp.18-24.

[10] Watanabe, K., Ohya, Y., Uchida, T., 2019. Power Output Enhancement of a Ducted Wind Turbine by Stabilizing Vortices around the Duct, Energies, Vol. 12, Issue 16, en12163171.

[11] Windlens, Inc., http://windlens.com/ (accessed Octorber 9, 2020)

[12] Hara, Y., sumi, T., Emi, T., Yokoyama, M., Akimoto, H., Kawamura, T., Nakamura, T., 2015. Effects of Blade Section on Performance of Butterfly Wind Turbines as Double-Blade VAWTs, Journal of Fluid Science and Technology, Vol. 10, Issue 1 (2015), p. JFST0003.

[13] Hara, Y., Shiozaki, A., Nishiono, H., Saito, S., Shioya, K., Sumi, T., Matsubara, Y., Yasumoto, Y., Takagaki, K., Kogo, S., 2016, Experiment and numerical simulation of an aluminum circular-blade butterfly wind turbine, Journal of Fluid Science and Technology, Vol. 11, Issue 2 (2016), p. JFST0010.

[14] Guidebook for the Introduction of Land-Based Offshore Wind Turbines (Final Version), New Energy and Industrial Technology Development Organization, March 2018.

[15] Milton Van Dyck, 1982. An Album of Fluid Motion, 12th edition, Parabolic Press, Inc., US.

[16] Robert D. Blevins, 1990. Flow Induced Vibration, Van Nostrand Reinhold Inc., U.S.

[17] Schlichting, H., Gersten, K., 2017. Boundary layer theory, 9th edition. ed. Springer Verlag, Berlin Germany.

[18] Robert G. Fuller, Charles R. Lang, Roberta H. Lang, 2000. Twin Views of the Tacoma Narrows Bridge Collapse, American Association of Physics Teachers, US.

[19] Fransson, J. H. M., Konieczny, P., Alfredsson, P. H., 2004. Flow around a porous cylinder subject to continuous suction or blowing, J. Fluids Struct. 19, 1031-1048.

[20] Sung, Y., Kim, W., Mungal, M. G., Cappelli, M. A., 2006. Aerodynamic modification of flow over bluff objects by plasma actuation, Exp. Fluid. 41, 479-486.

[21] Lecordier, J. C., Browne, L. W. B., Le Masson, S., Dumouchel, F., Paranthoen, P., 2000. Control of vortex shedding by thermal effect at low Reynolds numbers, Exp. Therm. Fluid Sci. 21, 227-237.

[22] Bae, H. M., Takahashi, T. and Shirakashi, M., 1993. Suppression of Karman vortex excitation of a circular cylinder by another cylinder located downstream in cruciform arrangement, Transactions of the JSME Series B, Vol. 59, No. 557(1993), pp.1-7 (In Japanese).

[23] Fox, T. A., 1990. Flow visualization at the center of a cross composed of tubes, International Journal of Heat and Flow, Vol. 11, Issue 2(1990), pp. 160-162.

[24] Fox, T. A., 1991. Wake characteristics of two circular cylinders arranged perpendicularly to each other, ASME Journal of Fluids Engineering, Vol. 113, Issue 1(1991), pp.45-50.

[25] Bae, H. M., Takahashi, T. and Shirakashi, M., Characteristics of longitudinal vortices shedding from two circular cylinders in cruciform arrangement, Transactions of the JSME Series B, Vol. 58, No. 549(1992), pp.1572-1579 (In Japanese).

[26] Takahashi, T., Baranyi, L., Shirakashi, M., 1999. Configuration and frequency of longitudinal vortices shedding from two cylinders in cruciform arrangement, Journal of the Acoustical Society of Japan, Vol. 19, Issue 75, 328-336.

[27] Kawabata, Y., Takahashi, T., Haginoya, T. and Shirakashi, T., 2011. Interference effect of downstream strip plate on the crossflow vibration of a square cylinder, Transactions of the JSME Series B, Vol. 77, No. 775(2011), pp.647-658 (In Japanese).

[28] Kato, N., Koide, M., Tahkahashi, T., Shirakashi, M., 2012. VIVs of a circular cylinder with a downstream strip-plate in cruciform arrangement, Journal of Fluids and Structures, Vol. 30, 97-114.

[29] Koide, M., Ootani, K., Yamada, S., Takahashi, T. and Shirakashi, M., 2006. Vortex excitation caused by longitudinal vortices shedding from cruciform cylinder system in water flow, JSME International Journal Series B, Vol. 49, No. 4(2006), pp.1043-1048.

[30] Koide, M., Takahashi, T., Shirakashi, M., Salim, S. A. Z. B. S., 2017. Three-dimensional structure of longitudinal vortices shedding from cruciform two-cylinder systems with different geometries, Journal of Visualization, Vol. 20, Issue 4, 753-763.

[31] Bernitsas, M. M., Raghavan, K., Ben-Simon, Y., and Garcia, 2008. E. M. H., VIVACE(Vortex Induced Vibration Aquatic Clean Energy): a new concept in generation of clean and renewable energy from fluid

flow, Journal of Offshore Mechanics and Arctic Engineering, Vol. 130, Issue 4(2008), 041101.

[32] Koide, M., Sekizaki, T., Yamada, S., Takahashi, T. and Shirakashi, M., 2011. Prospect of micro power generation utilizing VIV in small stream based on verification experiments of power generation in water tunnel, Transactions of the JSME Series B, Vol. 77, No. 775(2011), pp.702-714 (In Japanese).

[33] Takahashi, T., Yoshitake, Y., Komata, N. and Ueki, Y., Rotary device for fluid power generation and fluid power generation Device, 2016-111209, WO/2016/111209, 2015-1-7 (In Japanese).

[34] Takahashi, T., Yoshitake, Y., Sakamoto, K. and Hemsuwan, W., An innovative wind/water turbine with circular propeller driven by longitudinal vortex, Proceedings of the 15th WWEC2016 TOKYO conference (2016), PS-A-5.

[35] Hemsuwan, W., 2018. Numerical study of steady lift force generation on a circular cylinder by longitudinal vortex, Dissertation of the degree of Doctor of Engineering, Nagaoka University of Technology.

[36] Hemsuwan, W., Sakamoto, K., Takahashi, T., 2018. Lift force generation of a moving circular cylinder with a strip-plate set downstream in cruciform arrangement: flow field improving using tip ends, International Journals of Aeronautical and Space Sciences, Vol. 19, Issue 3, 606-617.

[37] Hemsuwan, W., Sakamoto, K., Nakada, S., Takahashi, T., 2018. A longitudinal vortex wind turbine: numerical study, Journal of Wind Engineering and Industrial Aerodynamics, Vol. 180, 213-230.

[38] Hemsuwan, W., Sakamoto, K., Takahashi, T., 2019. A longitudinal vortex wind turbine: effect of the blade lengths, Springer, Fluid-Structure-Sound Interactions and Control, 117-123.

2. Experimental conditions and procedures

The overview of the wind tunnel and the test section used in all the experiments in this dissertation are shown. Three types of circular cylinder blade wind turbine with different conditions for the circular cylinder blade and the ring-plate (single circular cylinder blade wind turbine, stepped circular cylinder blade wind turbine, and dual ring-plate) are described. The procedures of the experiments (visualization, fluid force measurement, un-loaded experiment, loaded experiment, and axial drag force measurement) and the measurement instruments used in each experiment are summarized.

2.1 Wind tunnel and test section

The wind tunnel used in all experiments is the blowdown type, and a test section with length of 1200mm and square-cross-section of 320mm is placed at the outlet. The velocity range is U = 2-40m/s and the turbulence intensities are 0.6% at the flow velocity U = 2m/s, which decreases to less than 0.3% at $U \geq$ 11.2m/s [1]. The flow velocity U is measured by the ring-type velocimeter [2] of which hot-wire probe is placed 200mm downstream from the inlet of the test section. The wind turbine is installed in the test section as shown in Fig. 2-1. The wind receiving surface of the circular cylinder blade is located 840mm measured from the inlet of the test section and the driving shaft is set at the position coincident with the center of square cross-section.
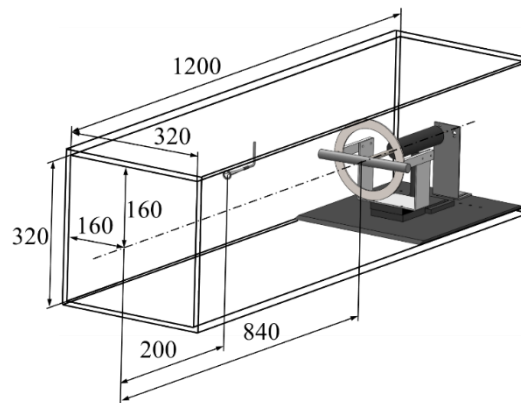

Fig. 2-1 Schematic diagram of test section and wind turbine setting. The unit of dimension is mm.
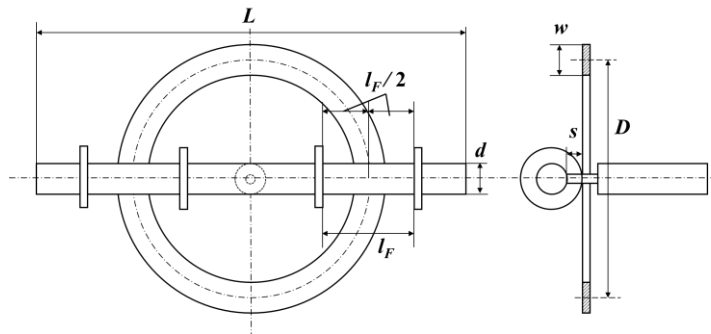
2.2 Circular cylinder blade wind turbine

2.2.1 Single circular cylinder blade wind turbine

A photograph and a schematic diagram of the circular cylinder blade wind turbine are shown in Fig. 1-16. A polyvinyl chloride pipe with closed ends with a diameter d = 20mm and a length l_{total} = 220 or 280mm is adopted as the rotor blade. The cylinder is fixed to the driving shaft at the span-wise center. A ring-plate with a 3mm thickness, a center diameter D = 155mm and a width W between 15-60mm is placed downstream of the circular cylinder blade with a gap s. The gap between the circular cylinder blade and the ring-plate is set arbitrarily in the range of s = 0 to 15 mm. For the performance enhancement, two pairs of flanges with a 40mm diameter and a 3mm thickness are attached to the longer cylinder blade (l_{total} = 280mm) with a separation length l_F as shown in Fig. 2-2.

The important parameters of the single circular cylinder wind turbine and their values in Chapter 4 are summarized in Table 2-1. A circular cylinder blade wind turbine with the basic structural parameters used in Chapter 4 is defined as the prototype model, and the structural parameters are d = 20mm, l_{total} = 220mm, W = 20mm, and D = 155mm.

The important parameters of the single circular cylinder wind turbine and their values in Chapter 6 and 7 are summarized in Table 2-2.

Schematic diagram of wind turbine with flange attachment

Fig. 2-2 Photograph and schematic diagrams of the single circular cylinder blade wind turbine.

Table 2-1 Parameters of wind turbine and experimental conditions in Chapter 4.

	Without flanges	With flanges	Prototype model
Cylinder blade diameter d [mm]	20		
Cylinder blade length l_{total} [mm]	220	280	220
Separation length ratio l_F/d [-] (l_F [mm])		3-7 (60-140)	
Width ratio of ring-plate W/d [-] (W [mm])	0.75-3 (15-60)	1 (20)	1 (20)
Ring-plate diameter D [mm]	155		
Gap ratio s/d [-] (s [mm])	0-0.5 (0-10)	0.35 (7)	
Total mass of the rotating shaft and circular cylinder blade m [kg]	0.23	0.24	0.23
Friction coefficient of ball bushing μ [-]	0.002 [3]		

Table 2-2 Parameters of single circular cylinder blade wind turbine and experimental conditions in Chapter 6 and 7.

	Chapter 6	Chapter 7
Cylinder blade diameter d [mm]	20	
Cylinder blade length l_{total} ($l_{total}/2$) [mm]	220 (110)	
Ring-plate width W [mm]	15, 20, 30	20, 40
Ring-plate diameter D [mm]	155	
Gap ratio s/d [-]	0.2-0.5	0.35

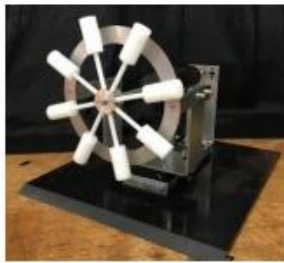**2.2.2**   Stepped circular cylinder blade wind turbine

A photograph and a schematic diagram of the stepped circular cylinder blade wind turbine with blade number $N = 8$ are shown in Fig. 2-3. The dimensions of downstream ring-plate are determined such as the center diameter $D = 155$mm, the width $W = 20$mm and the thickness 3 mm. And the gap between the stepped circular cylinder blade and the ring-plate is set arbitrarily in the range of $s = 0$ to 15 mm. The stepped circular cylinder blades are made of Teflon-rod, and they are attached to a hub with a 30mm diameter and a 20mm thickness fixed to the driving shaft at equal intervals, up to the maximum number of the blade $N = 12$. The diameter of the supporting rod part is $d' = 6$mm, and the protruding length of the effective part from rims of the ring-plate l_P is equal between inside and outside the ring-plate.

The important parameters of the stepped circular cylinder blade wind turbine are the blade length and diameter of effective region l and d, and the number of blades N. The important parameters of the stepped circular cylinder wind turbine and their values in Chapter 5 are summarized in Table 2-3. A prototype model of the stepped circular cylinder blade in Chapter 5 is defined as follows: the cylinder diameter of the

effective region where the lift force of NV acts is set to $d = 20$mm, its length $l = 60$mm ($l/d = 3$), the total length is $l_{total} = 215$mm, and the protruding length is $l_P = 20$mm. Influence of the number of blades is investigated for this prototype model by varying N in the range of $N = 2$-12. In order to investigate the influence of effective blade length, the five different effective lengths, i.e., $l = 40, 50, 70, 80, 90$ mm are tested with $N = 2$ turbine. The total blade lengths in their case are $l_{total}/2 = 97.5$-122.5mm. In order to investigate the influence of effective blade diameter, the four different effective diameters, i.e., $d = 23, 25, 28, 30$ mm with the effective length of $l = 60$mm are tested with $N = 2, 4, 8, 10$ turbines.
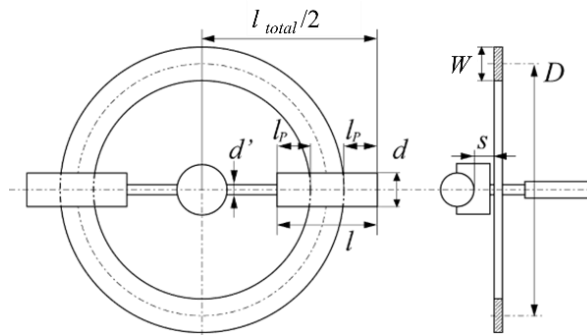
The important parameters of the stepped circular cylinder wind turbine and their values in Chapter 3, 6 and 7 are summarized in Table 2-4.

(a) Photograph of stepped circular cylinder blade wind turbine for d=20mm, l=60mm and N=8

(b) Structure of rotation mechanism at un-loaded condition for d=20mm, l=60mm and N=8

(c) Schematic diagram and parameters at $N = 2$

Fig. 2-3 Photographs and schematic diagrams of stepped circular cylinder blade wind turbine

Table 2-3 Dimensions of stepped circular cylinder blades and parameters of wind turbine and experimental conditions in Chapter 5.

Blade diameter d [mm]	20	23	25	28	30
Supporting rod diameter d' [mm]	6				
Effective length l [mm]	40-90	60			
Protruding length l_P [mm]	10-35	20			
Cylinder blade length $l_{total}/2$ [mm]	97.5-122.5	107.5			
Number of blades N [-]	2-12 for l = 60mm 2 for other l's	2-10			
Ring-plate width W [mm]	20				
Ring-plate diameter D [mm]	155				
Gap ratio s/d [-] (s [mm])	0.2-0.7 (6-15)				

Table 2-4 Parameters of stepped circular cylinder blade wind turbine and experimental conditions in Chapter 3, 6 and 7.

|	Chapter 3	Chapter 6	Chapter 7
Cylinder blade diameter d [mm]	20, 28	20	
Effective length l [mm]	40		50
Protruding length l_p [mm]	10		15
Cylinder blade length l_{total} [mm]	195		205
Number of blades N [-]	2 for d = 20mm 2, 4, 8 for d = 28mm	2, 8	2, 4, 6, 8
Ring-plate width W [mm]	20		
Ring-plate diameter D [mm]	155		
Gap ratio s/d [-]	0.35	0.2-0.5	0.35

2.2.3　Dual ring-plate

A photograph and a schematic diagram of the circular cylinder blade wind turbine with the deal ring-plate are shown in Fig. 2-4. Seven different diameters of ring-plate of D = 80-130 and 180 mm are used in the dual ring-plate. The center diameter of the ring-plate attached to the outside is D_{large}, and the inside ring-plate is D_{small}. D_{large} is fixed to 180mm and D_{small} is changed between 80 and 130mm. Therefore, the gap between ring-plates is determined as W_{ring} (= $D_{large}/2$-$D_{small}/2$-W) = 5-30mm. The gap ratio s/d is set so that the inside and outside ring-plates are equal, and s/d is fixed at 0.35.

For the single circular cylinder blade wind turbine, the long cylinder blade with d = 20mm and l_{total} =

220mm is used. In the experiments for the stepped circular cylinder blade wind turbine, the effective length is set between $l = 75$ and 100mm so that l_P is fixed to15mm in all condition of W_{ring}. This $l_P = 15$mm is equal to the protruding length of $l = 50$mm, which is the maximum rotational speed at un-loaded condition is obtained, for the stepped circular cylinder blade wind turbine with $W = 20$mm as shown in Chapter 5. That is, $l_P = 15$mm is a condition where the fluid resistance region for rotation at both ends of the circular cylinder blade is minimized. Since D_{large} is fixed to180mm, the total blade length is fixed at $l_{total} = 230$mm. In order to investigate the effect of the blade number at $W_{ring} = 10$, 20mm, 8-stepped circular cylinder blades with effective lengths of $l = 80$, 90mm are prepared. And 2-stepped circular cylinder blades are prepared at other l. Table 2-5 shows the conditions of structural parameter for each circular cylinder blade wind turbine with the dual ring-plate.
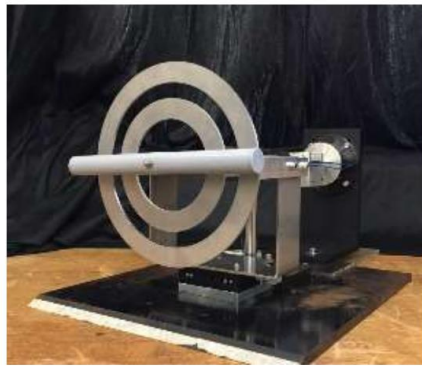
(a) Setting of dual ring-plate on single cylinder blade type wind turbine
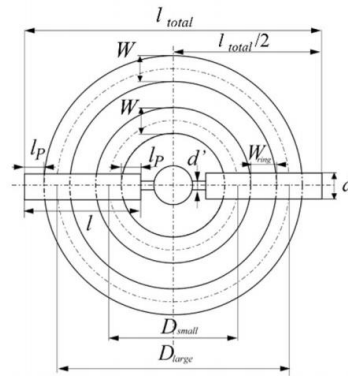
(b) Schematic diagram and parameters of dual ring-plate on stepped circular cylinder blade type wind turbine

Fig. 2-4 Photographs and schematic diagrams of dual ring-plate.

Table 2-5 Parameters of experiments for dual-ring plate.

Wind turbine type	Single circular cylinder	Stepped circular cylinder
Cylinder blade diameter d [mm]	20	
Effective length l [mm]		80 and 90 for $N = 2$-8 75-100 for $N = 2$
Protruding length l_p [mm]		15
Cylinder blade length l_{total} ($l_{total}/2$) [mm]	220 (110)	230 (115)
Number of blades N [-]	(2)	2, 4, 6, 8
Ring-plate width W [mm]	20	
Outside ring-plate diameter D_{large} [mm]	180	
Inside ring-plate diameter D_{small} [mm]	80-130	
Gap between ring-plates W_{ring} [mm]	5-30	
Gap ratio s/d [-]	0.35	

2.3 Experimental procedures

2.3.1 Visualization experiment

The equivalent diameter D_V of NV is obtained from the visualization result in each experimental condition and the results are evaluated. A schematic of the visualization experiment is shown in Fig. 2-5(a). In order to straighten the flow from the wind tunnel, a honeycomb with a height of 320mm, a width of 320mm, and a thickness of 50mm shown in Fig. 2-5(b) is placed 100mm away from the circular cylinder blades. The smoke from the fog generator (Porta smoke PS-2006, Dainichi Co., Ltd.) flows out through a φ5mm pipe and flows from the upstream to the downstream of the honeycomb. A high-speed camera (FASTCAM SA, Photron Ltd.) is used to take the movies of the smoke motion and a LED light is used to observe the smoke clearly. A few images in which the cross-section of the NV is clearly visible are selected from the movies, and the area of the inside of NV (A_V) is detected by an image analysis software, Image J [3]. The equivalent diameter of the NV (D_V) is calculated by Eq. (2-1).

$$D_V = 2\sqrt{\frac{A_V}{\pi}} \qquad (2-1)$$

(a) Outline of visualization   (b) Photograph of honeycomb
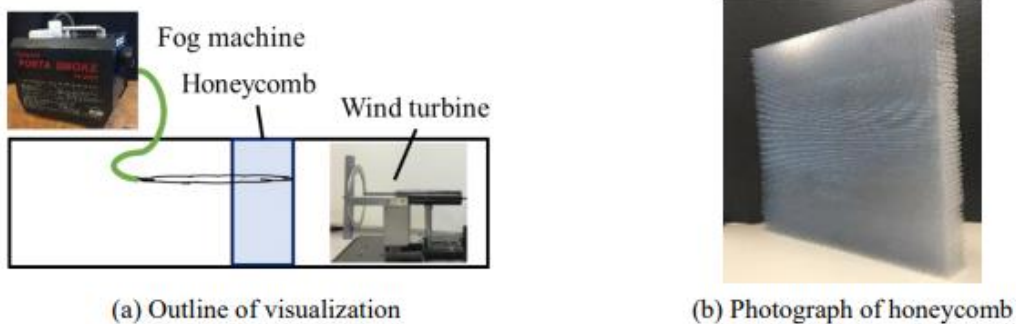
Fig. 2-5 Photograph of honeycomb installed in the test section.

2.3.2 Fluid force measurement

An overview of the measurement apparatus for fluid force is shown in Fig. 2-6(a). A single circular cylinder blade wind turbine is rotated at a given rotational speed to set an attack angle, and the lift force, which is the force in the cross-flow direction acting on the single circular cylinder blade, is measured. The single circular cylinder blade rotates forcibly at an arbitrary speed n by a motor (BLM230HP-5S, Oriental Motor Co., Ltd.) attached to the end of the driving shaft. As shown in Fig. 2-6(b), a torque meter is connected between the motor and driving shaft holder (ball bushing). The force in the flow direction is measured as the fluid torque T_z, and the fluid force coefficient C_z is calculated. When a cylinder in a cylinder/strip-plate cruciform system moves in the cross-flow direction, the flow velocity U and the cylinder moving velocity V are composed as shown in Fig. 2-7(b), and the cylinder receives a relative flow

velocity U_r with an attack angle of α with respect to the mainstream. The fluid force F_z applied to a cylinder is lead as

$$F_z = \frac{1}{2} C_z \rho d l U^2, \tag{2-2}$$

where ρ is the density, and d and l are the diameter and length of the cylinder. The relative attack angle α determined by the flow velocity U and the moving velocity of cylinder V is lead as

$$\alpha = \tan^{-1}\left(\frac{V}{U}\right) \cdot \frac{180}{\pi}. \tag{2-3}$$

The moving velocity in the cross-flow direction of the single circular cylinder blade at the intersection V is determined by the rotation speed of the single circular cylinder blade n and the ring-plate diameter D, as

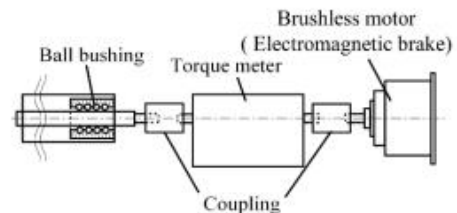$$V = \frac{D}{2} \cdot \frac{2\pi n}{60}. \tag{2-4}$$

Considering that the point of application of the fluid force F_z by the longitudinal vortex is two as shown in Fig. 2-7 (a), F_z is lead as

$$F_z = \frac{T_z/2}{D/2} \tag{2-5}$$

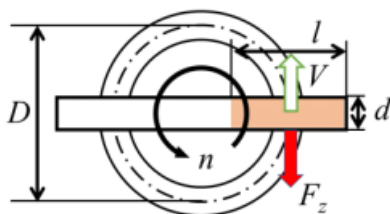and Cz is obtained by substituting F_z into Eq. (2-2).
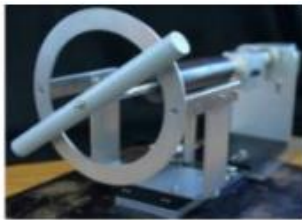
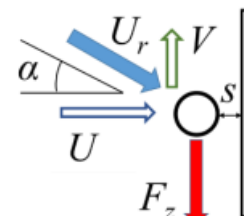(a) Photograph of measurement apparatus of fluid force

(b) Schematic of setup of measurement instrument

Fig. 2-6 Setup of measurement apparatus for measurement of fluid force.

(a) Front view

(b) Side view

Fig. 2-7 Schematic of flow velocity and force vectors on rotating cylinder.

2.3.3 Un-loaded experiment

The relationship between the terminal rotational speed n and the gap ratio s/d for fixed flow velocities U is measured under the un-loaded condition, i.e., the torque meter and the brake are not attached to the driving shaft shown in Fig. 1-16(a). And the relationship between n and U for fixed values of s/d is measured. The rotational speed of the driving shaft is measured by the non-contacting optical tachometer (AT-6, MK Scientific, Inc.). The driving shaft is held by the ball bushing that rotates and slides with small resistance in the rotational and axial directions. The downstream tip of the driving shaft used in the un-loaded experiments has a sharp needle-shape, and the downstream force due to the axial drag force acting on the circular cylinder blades is held by the tip of the needle of the driving shaft and a steel plate. That is, the axial drag does not affect the rotational load.

2.3.4 Loaded experiment

Both the rotational speed n and the output torque T_{brake} are measured from the driving shaft at $U = 10$m/s where the friction loss by the ball bushing is negligible. The motor shown in Fig. 2-6(b) is replaced with an electromagnetic brake (HB0.5, OGURA CLUTCH Co., Ltd.). The rotational speed n is decreased in steps until the rotational speed reaches $n = 0$ by increasing the load from the electromagnetic brake, and n and T_{brake} are measured by a torque meter.

2.3.5 Axial drag force measurement

2.3.5.1. Experimental apparatus

The axial drag force acting on the single circular cylinder blade $F_{D,U}$ is measured under the three conditions.
(1) The single circular cylinder blade and the ring-plate are attached, and the single circular cylinder blade freely rotates (rotating cylinder).
(2) The single circular cylinder blade and the ring-plate are attached, but the single circular cylinder blade is fixed and does not rotate (fixed cylinder).
(3) The ring-plate is removed and only the single circular cylinder blade is attached (cylinder only).
The photographs describing three conditions are shown in Fig. 2-8. As shown in Fig. 2-8(b), the cylinder is fixed by placing two thin rectangular rods with a 5mm cross-section on both sides of the single circular cylinder blade. The spanwise direction of the rectangular rods is parallel to the main flow. Since the rectangular rods do not affect the formation of NVs and TVs, they are placed close to the driving shaft for the single circular cylinder blade and at d' for the stepped circular cylinder blade.

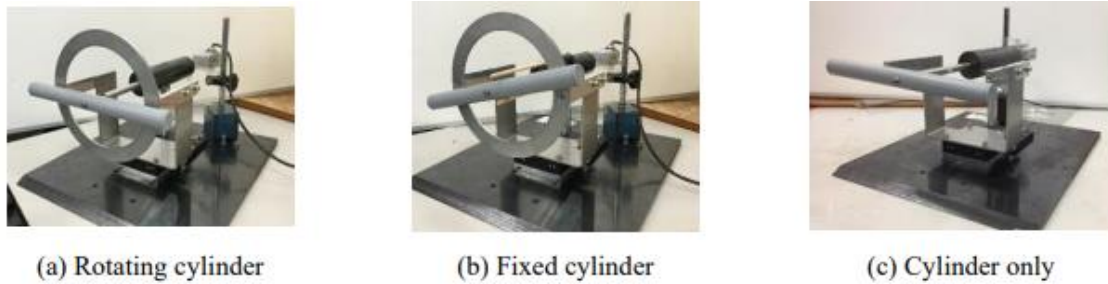(a) Rotating cylinder   (b) Fixed cylinder   (c) Cylinder only

Fig. 2-8 Setting methods for measurement of axial drag force.

2.3.5.2. Calibration and installation of load cell

Since the force acting on the tension/compression load cell (LTS-500GA, Kyowa Electronic Instruments Co., Ltd.) is output as the voltage, this output voltage needs to convert into the drag force by the calibration formula. The calibration was carried out for each experiment by the following procedure in order to derivate the calibration formula. It is assumed that the absolute values of the output of the voltages by applying the same force of tension and compression are equal.

1. The output voltage was measured for ten seconds and the average voltage was determined in the load cell fixed so that it would not slip. At this time, since the load is not applied to the load cell, both the output voltage and the force acting on the load cell are set to zero.

2. A scale pan with a weight of m_{plate} ($\simeq$ 19.4g) was attached at a right angle to the load cell via a pulley system as shown in Fig. 2-9. The tensile force of $m_{plate}*9.8*10^{-3}$ ($\simeq$ 0.19N) acts on the load cell. When the scale pan was the stationary state, the voltage was measured for ten seconds and the average voltage was determined.

3. The balance weights of 5, 10, 20, 50, 100, and 200g were placed on the scale pan and the average voltage was determined. The relationship between the tensile force F and the output voltage V was obtained by above measurements.

4. The relationship F and V obtained by the procedure 1-3 is shown as an example in Fig. 2-10. An approximation is determined from this relationship and this approximation was used as a calibration formula for drag force measurement.

As shown in Fig. 2-11, the measuring shaft of the load cell is attached to the tip of the driving shaft in parallel to the main flow.
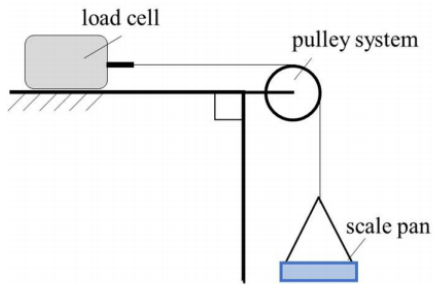
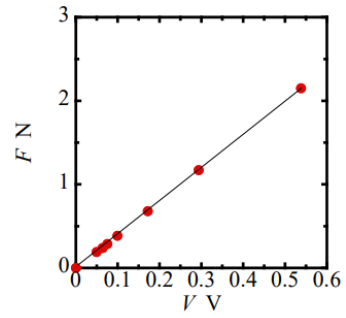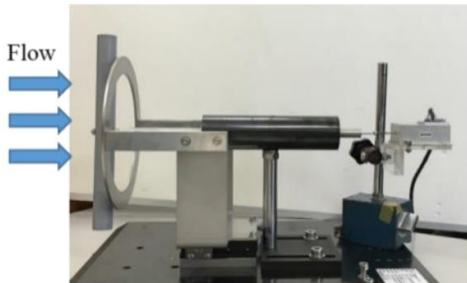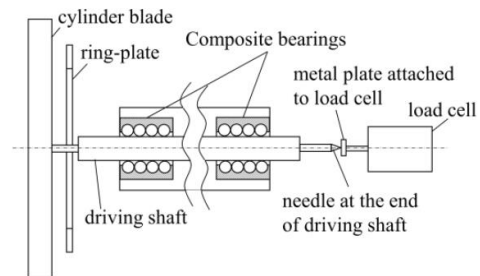Fig. 2-9 Schematic diagram of calibration of load cell.

Fig. 2-10 Example of calibration by using pulley system and weight. This linear approximate equation is $F=4.13V-0.0109$.

(a) Setting of load cell in experimental apparatus

(b) Schematic diagram of mechanism of experimental apparatus

Fig. 2-11 Setting method of load cell into wind turbine.

References

[1] Kato, N., Koide, M., Tahkahashi, T., Shirakashi, M., 2012. VIVs of a circular cylinder with a downstream strip-plate in cruciform arrangement, Journal of Fluids and Structures, Vol. 30, 97-114.

[2] Koide, M., Takahashi, T. and Shirakashi, M.,2001. Development of a ring-type vortex anemometer for low-velocity wind tunnel experiment, Transactions of the Japan Society of Mechanical Engineers Series B, Vol. 67, No. 657 (2001), pp. 1105-1111.

[3] NIPPON BEARING CO., LTD, Frictional resistance for required thrust, http://www.nb-linear.co.jp/english/technology/friction_thrust.html/(accessed 27 March 2019).

[4] Rasband, W. S., 1997-2012, "ImageJ", U. S. National Institutes of Health, Bethesda, Maryland, USA, http://rsb.info.nih.gov/ij/.

3. Visualization of longitudinal vortex

The process of formation and shedding of the necklace vortex (NV) at the intersection of rotating stepped circular cylinder blade and ring-plate is observed by the smoke visualization. By the evaluation of the cross-section diameter of the NV from the visualization results, the influence of the experimental conditions such as the diameter of the circular cylinder blade and the pitch between the circular cylinder blades on the formation of the NV is examined.

3.1 Visualization of necklace vortex

Figure 3-1 shows examples of visualization at the intersection between the cylinder blade and the ring-plate of the stepped circular cylinder blade wind turbine. The smoke flows from left to right, and the stepped circular cylinder blade rotates downward. Fig. 3-1(a) shows that a stepped circular cylinder blade just was about to pass through a streamline containing smoke. Vortices were not observed in front of the cylinder and the smoke was sucked into the gap between the stepped circular cylinder blade and the ring-plate. The three photographs of Fig. 3-1(b) show the visualization results where the streamline including smoke is behind the moving direction of the stepped circular cylinder blade. The cross-section of NV was observed in the gap between the stepped circular cylinder blade and ring-plate, as same as the numerical visualization shown in Fig. 1-19 in Chapter 1. The NV rotated clockwise and was fixed behind the stepped circular cylinder blade. The visualization of this series confirmed that the NV formed steadily in the gap on the opposite side of the moving direction of stepped circular cylinder blade which was consistent with the results of the numerical analysis [1].

(a) Suction flow forward in the rotational direction

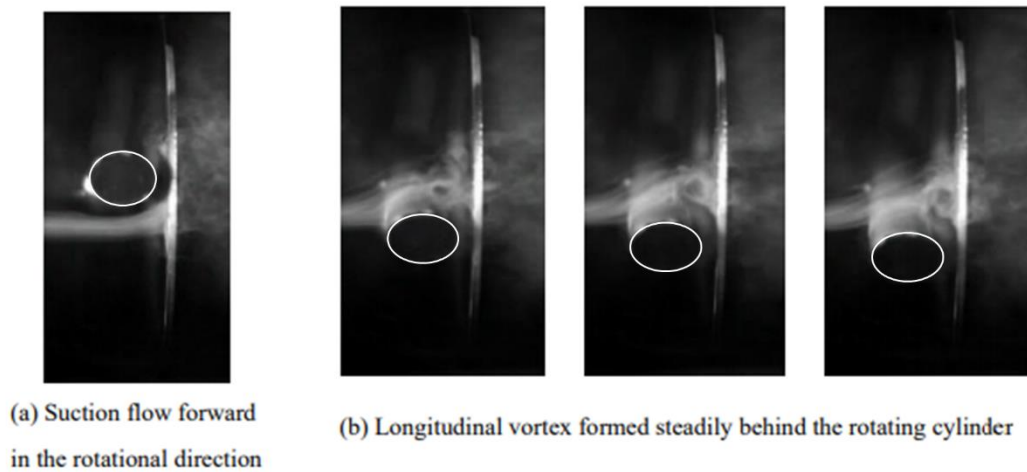(b) Longitudinal vortex formed steadily behind the rotating cylinder

Fig. 3-1 Visualization of flow around cross-section of stepped circular cylinder blade and ring-plate. Stepped circular cylinder blade rotates downward (d = 20mm, l = 40mm, l_P = 10mm, l_{total} = 195mm, N = 2, W = 20mm, D = 155mm, s/d = 0.35). White circles show tip-end of stepped cylinder.

3.2 Effect of blade diameter

Figure 3-2 shows the examples of the visualization results of the NV at $N = 2$ and $d =20$, 28mm. The smoke flows from the left side to the right in each figure and the stepped circular cylinder blade rotates downward, therefore, the NV constantly formed in the upper right of the stepped circular cylinder blade while rotating clockwise. Table 3-1 shows the average ($D_{V\,Ave}$) and its standard deviation (SD), maximum ($D_{V\,Max}$), minimum ($D_{V\,Min}$) of the equivalent diameter of NV, and the number of detected NVs from the movies. The results of $D_{V\,Ave}$, $D_{V\,Max}$, and $D_{V\,Min}$ at $d = 28$mm were larger than those of $d = 20$mm. The value of $D_{V\,Ave}$ of $d = 28$mm is about 1.3 times larger than that of $d = 20$mm, i.e., $D_{V\,Ave\,28mm}/D_{V\,Ave\,20mm} \simeq 1.3$, and is almost coincides with the diameter ratio of stepped circular cylinder blade, which is $d_{28mm}/d_{20mm} = 1.4$. The above results infer that D_V of the NV increases linearly with the increase in the cylinder blade diameter while keeping similarity of their geometric shape. This linear increase of D_V is considered to occur only specific N in which the flow fields around adjacent cylinder blades do not interfere with each other. The value of SD at $d = 28$mm is larger than that at $d = 20$mm, and it infers that the deformation of the NV and fluctuation of the lift force easily occur at larger d.

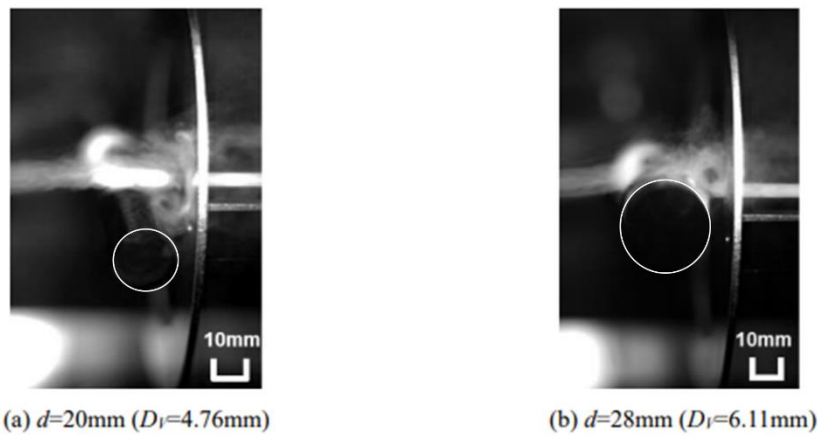(a) $d=20$mm ($D_I=4.76$mm)   (b) $d=28$mm ($D_I=6.11$mm)

Fig. 3-2 Visualization of the longitudinal vortex forming behind the stepped circular cylinder blades ($d = 20$, 28mm, $l = 40$mm, $l_P = 10$mm, $l_{total} = 195$mm, $N = 2$, $W = 20$mm, $D = 155$mm, $s/d = 0.35$, $U = 3\text{-}4$m/s). White circles show tip-end of stepped cylinder.

Table 3-1 Equivalent diameter of the longitudinal vortex obtained by image analysis at each stepped circular cylinder blade diameter at $N = 2$.

	$D_{V\,Ave}$ mm	SD	$D_{V\,Max}$ mm	$D_{V\,Min}$ mm	Number of NV
$d = 20$mm	4.82	0.372	5.44	4.24	13
$d = 28$mm	6.31	0.487	6.91	5.56	11

3.3　Effect of blade number

Figure 3-3 shows the examples of the visualization results at $N = 4$, 8 and $d = 28$mm. The visualization result for $d = 28$ mm and $N = 2$ in Fig. 3-2(b) is also shown for comparison. The movement states of smoke, stepped circular cylinder blade, and NV are same as those shown in Fig. 3-2. The calculated $D_{V\,Ave}$, SD, the number of detected NVs in each N are shown in Table 3-2. $D_{V\,Ave}$ was almost constant through all N and it showed that $D_{V\,Ave}$ is not dependent on N. When $N = 8$ shown in Fig. 3-3(c), the formation of NV and the suction flow occur next to each other. In the observations and the results, the values of SD at $N = 2$ and $N = 8$ were almost the same and the disturbance of the formation of NV or suction flow was not observed. However, it is assumed that by the pitch distance between the stepped circular cylinder blades becomes narrower, the flow fields around the adjacent cylinder blades interfere with each other, and it causes the disturbance of the formation of NV and leads reduction of the lift force.
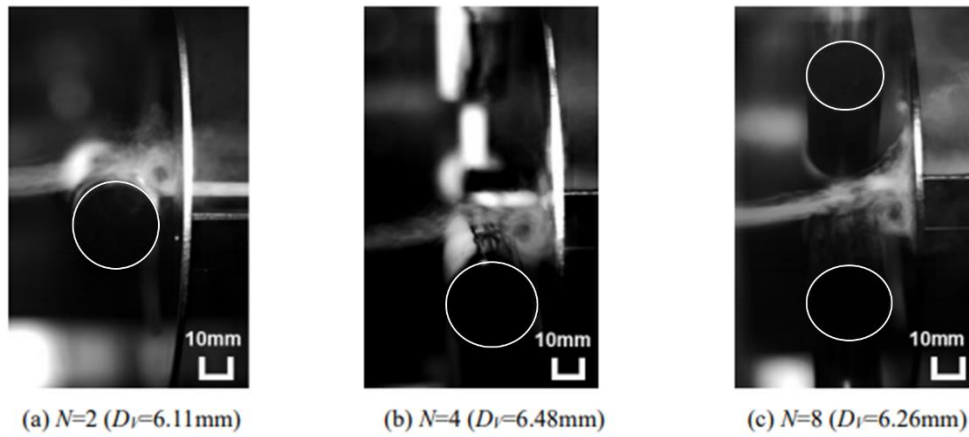

(a) N=2 (D_l=6.11mm)　　　(b) N=4 (D_l=6.48mm)　　　(c) N=8 (D_l=6.26mm)

Fig. 3-3 Visualization of the longitudinal vortex forming behind the stepped circular cylinder blades ($d = 28$mm, $l = 40$mm, $l_P = 10$mm, $l_{total} = 195$mm, $N = 2, 4, 8$, $W = 20$mm, $D = 155$mm, $s/d = 0.35$, $U = 3$-4m/s). White circles show tip-end of stepped cylinder.

Table 3-2 Equivalent diameter of the longitudinal vortex obtained by image analysis at each stepped circular cylinder blade number at $d = 28$mm.

	$D_{V\,Ave}$ mm	SD	Number of NV	t mm
$N = 2$	6.31	0.487	11	215.5
$N = 4$	6.48	0.298	10	93.7
$N = 8$	6.37	0.482	9	32.9

3.4　Conclusions

In this chapter, the process of formation and shedding of necklace vortex (NV) at the cross-section of the rotating circular cylinder blade and ring-plate was observed by the visualization, and the influence of the diameter of the circular cylinder blade and the pitch between the circular cylinder blades on the size of NV was examined. The following conclusions were obtained from the experimental results and discussion.

1. The NV was stably formed in the gap on the opposite side of the moving direction of stepped circular cylinder blade, which agreed with the results of the numerical analysis.

2. The equivalent diameter of NV in cross-section increased linearly to the increase of blade diameter d at constant blade number N.

3. The equivalent diameter was almost constant through all N within the experimental condition for the constant d.

4. When the pitch between stepped circular cylinder blades is small, the formation of NV and the suction flow occurred next to each other. It is considered that the excessive decrease in the pitch causes the interference of the flow fields around the adjacent cylinder blades.

Reference

[1] Hemsuwan, W., Sakamoto, K., Takahashi, T., 2018. Lift force generation of a moving circular cylinder with a strip-plate set downstream in cruciform arrangement: flow field improving using tip ends, International Journals of Aeronautical and Space Sciences, Vol. 19, Issue 3, 606-617.
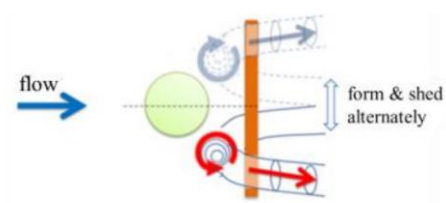
4. Basic characteristics of the single circular cylinder blade wind turbine

The steady lift forces acting on a cylinder blade is measured by using single circular cylinder blade wind turbine with the simplest structure, and the relationship between the relative attack angle and lift force is investigated. The basic rotational and output torque characteristics are also examined. The lift and drag coefficients acting on the rotating direction are estimated from the torque of the rotating single circular cylinder blade. The important structural parameters that characterize single circular cylinder blade wind turbines are identified, and the effects of these parameters on the performance of wind turbines are clarified based on the experimental results.
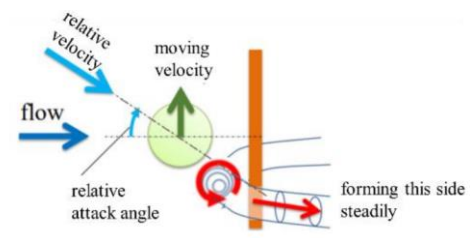
4.1 Consideration of the stabilization of longitudinal vortex that forms and disappears alternately

The longitudinal vortex (LV) is formed near the intersection of the cruciform circular-cylinder/strip-plate system, which is placed in the uniform flow, as shown in Fig. 1-15. The LV alternately forms and disappears behind the cylinder body diagonally in a uniform flow, such as the Karman vortex street (KV). The formation and disappearance of LV are highly periodic, and the shedding frequency is strongly affected by the flow velocity and shape factors. In the case of the necklace vortex (NV), the location of NV alternates the upper and lower sides of the upstream cylinder in the gap with the downstream strip-plate at the intersection, as shown in Fig. 4-1(a). The periodic change of the position of the LV causes periodic fluid forces in the cross-flow direction to act on the cylinder. If it is possible that the LV is constantly formed on either the upper or lower side of the cylinder, the steady lift in the cross-flow direction acts on the cylinder. As a method to stabilize the positions of the LV, the creation of the relative attack angle was tried by moving cylinder in the cross-flow direction. As shown in Fig. 4-1(b), the situation in which a cylinder moves upward along the strip-plate at a constant speed was considered. The cylinder has a relative attack angle due to the composition of the flow velocity and the moving velocity of the cylinder. When the strip-plate is installed with a certain gap with the cylinder, the flow field between the cylinder and the strip-plate becomes asymmetrical due to the occurrence of the relative attack angle. It was assumed that the NV is formed stably on the wide gap side which is opposite to the moving direction of the cylinder, and the steady lift force acts on the cylinder.

This assumption is verified by the simple model shown in Fig. 1-16. Instead of parallel moving of the cylinder along the strip-plate, the driving shaft is attached to the center of the span-wise direction of the cylinder so that it rotates like a propeller, and the strip-plate is modified to ring-shaped and installed in the downstream so that it is concentric with the cylinder driving shaft. When the diameter of the ring-plate is large enough, the flow near the intersection will be like the schematic diagram in Fig. 4-1(a). The flow field shown in Fig. 4-1(b) is provided by applying an initial velocity to the cylinder in either direction. When the velocity of mainstream is low, the cylinder is given an initial speed in either direction and continues to rotate in that direction. Then the rotation accelerates angularly until it reaches a predetermined rotational speed and reaches a steady state. When the mainstream velocity exceeds about 3m/s, the cylinder can begin to rotate independent of a resting state without giving an initial velocity. At high mainstream velocity, the cylinder starts to rotate in one direction instantly, but at low velocities, the cylinder may start to accelerate in one direction after it starts to rotate from a resting state while changes the direction of rotation one or two times.

(a) Fixed cylinder system   (b) Parallel moving cylinder with a constant moving velocity

Fig. 4-1 Necklace vortices at cross-section of cruciform system of upstream circular cylinder and downstream strip-plate.

4.2 Rotation characteristics

The relative attack angle α was changed by rotating the single circular cylinder blade wind turbine of the prototype model at a given rotational speed at a constant flow velocity $U = 10$m/s, and the fluid force coefficient C_z was calculated from the torque acting on the driving shaft T_z measured by torque meter. Fig. 4-2 shows the relationship between α and C_z for the gap ratios $s/d = 0.1$ and 0.4. In the case of $s/d = 0.1$, C_z increased monotonically with increasing α and was positive at all α. These results mean that the force is opposite to the direction of rotation of the single circular cylinder blade, i.e., the force that restrains the rotation acts on the single circular cylinder blade, and this force becomes stronger when the rotational speed is increased. This force suggests that the rotation of the single circular cylinder blade stops even when the initial velocity is applied at $s/d = 0.1$. On the other hand, In the case of $s/d = 0.4$, C_z showed a negative value at $\alpha \le 11$deg. This negative value of C_z means that the single circular cylinder blade receives a force in the rotation direction when the single circular cylinder blade starts rotating, and accelerates. The smaller the value of C_z becomes, the larger the force acting on the single circular cylinder blade becomes. When α becomes larger than 11deg, C_z turned to a positive value and the force acted in the direction that suppresses the increase in the rotational speed.

In order to investigate the relationship between the experimental results shown in Fig. 4-2 and the behavior of the single circular cylinder blade, the terminal rotational speeds of the single circular cylinder blade were measured when the gap ratio was increased step-wisely within the range of $s/d = 0$ to 0.5 at a constant flow velocity $U = 10$ m/s. This experiment was conducted without load in which the motor and the torque meter were removed from the tip of the driving shaft. Fig. 4-3 shows the measured rotational speed n of the single circular cylinder blade and the relative attack angle α calculated from the rotational speed at each s/d. The rotation stopped even if the initial velocity was applied in the range of $0 \le s/d < 0.35$, including $s/d = 0.1$. For $s/d = 0.4$, the rotational speed was $n = 245$rpm, i.e., the single circular cylinder blade rotated steadily so that the relative attack angle keeps about $\alpha = 11.5$deg. This value of α agreed well with the value of α in Fig. 4-2 where the sign of C_z was inverted at $s/d = 0.4$. This agreement shows that the rotational speed is determined so that C_z becomes zero when the single circular cylinder blade rotates freely due to the mainstream when the load, such as frictional resistance by the ball bushing, is negligibly small. The single circular cylinder blade began to rotate steadily and independently at $s/d = 0.35$, and n decreased monotonically with the increasing of s/d. This result shows that $s/d = 0.35$ is the critical condition that the force acts in the rotational direction by the LV, and the value of α where $C_z = 0$, changes with s/d. This critical condition $s/d = 0.35$ is also the condition for the formation of NV, as shown in Fig. 1-15 in Subsection 1.2.3. Therefore, the driving force for rotation of the single circular cylinder blade is provided by the lift force of the NV.

The terminal rotational speed of the single circular cylinder blade was measured for a stepwise increase in the flow velocity U with an optimum gap ratio of $s/d = 0.35$ under un-loaded conditions. The relationship between U and n is shown in Fig. 4-4. In addition, the relationship between the relative attack angle α and

U is shown in Fig. 4-5. The relationship between U and n did not pass through the origin as shown in Fig. 4-4, but n increased linearly with the increase in U after the start of rotation (cut-in). The result shows up to $U = 12$m/s, but this linear relationship continued until $U = 35$m/s, which is the limit of the measurement system of wind tunnel, in subsequent experiments. The fact that this line of U and n does not pass through the origin is thought to be due to the initial load of the experimental apparatus caused by mechanical friction such as the ball bushings. Considering the change of the flow velocity U_{min} in which the wind turbine starts rotation caused by the mechanical friction, the converted relative attack angle α' was calculated from the relationship between n and the converted flow velocity U' (= $U-U_{min}$) at which the wind turbine starts a steady rotation from $U \geq 0$. The value of α' shown in Fig. 4-5 was almost constant regardless of U and this result shows that the rotational speed is determined so that C_z becomes zero at un-loaded condition.
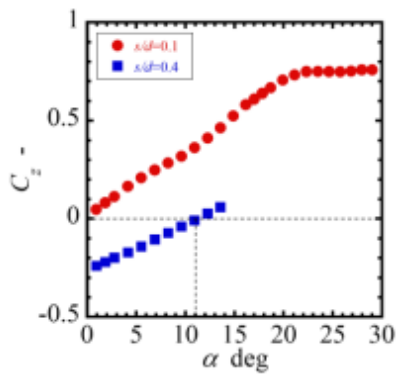
Fig. 4-2 Relationship between fluid force coefficient and relative attack angle in rotating circular cylinder blade at constant flow velocity. d=20mm, W=20mm, l_{total}=220mm, D=155mm, U=10m/s.
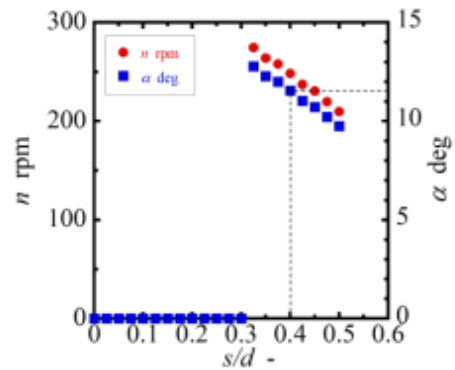
Fig. 4-3 Effect of gap ratio s/d on rotational speed n of circular cylinder blade wind turbine. d=20mm, W=20mm, l_{total}=220mm, D=155mm, U=10m/s, and s/d=0~0.5.
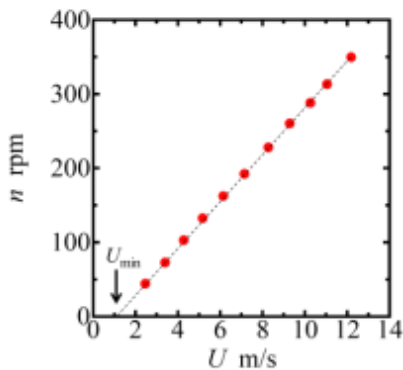
Fig. 4-4 Rotational speed vs. flow velocity d=20mm, W=20mm, l_{total}=220mm, D=155mm, and s/d=0.35
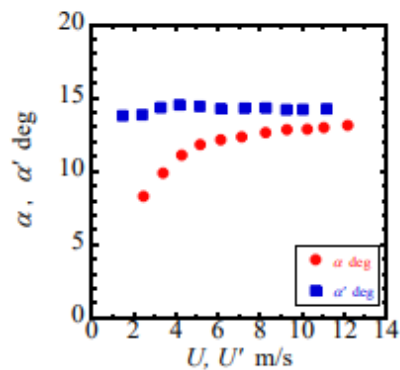
Fig. 4-5 Relative attack angle vs. flow velocity. d=20mm, W=20mm, l_{total}=220mm, D=155mm, and s/d=0.35.

4.3 Un-loaded and loaded experiments for prototype model

Figure 4-6 again shows the relationship between the rotational speed n and the flow velocity U obtained in un-loaded experiments for the prototype model with the gap ratio of $s/d = 0.35$ shown in Fig. 4-4. Open symbol shows the experimental result at $U = 10$m/s and $s/d = 0.35$ shown in Fig. 4-3 and the solid line shows the calculation by the method proposed in Section 4.5. The cross symbols on the U-axis shows the velocity for starting of rotation, U_{start}, calculated by the criterion given in Section 4.5. The single circular cylinder blade attained steady rotation at the minimum flow velocity of the wind tunnel, $U \simeq 2$m/s being much higher than U_{start}, and n increased almost proportionally to U.

Figure 4-7 shows the relationship between the load torque T_{brake} and rotational speed n obtained through the loaded experiments at $U = 10$m/s for the prototype model with $s/d = 0.35$. The open symbol shows the experimental result of un-loaded experiments at $U = 10$m/s and $s/d = 0.35$ shown in Fig. 4-3 and the solid line shows the calculation by the method proposed in Section 4.5. In this figure, as well as in Figs. 4-9, 4-10(b) and Fig. 4-13 for results of loaded experiments under various conditions, the maximum value of n at $T_{brake} = 0$, n_{max}, and the result of un-loaded experiments (open symbol) agreed well each other. Hence, the mechanical friction by the torque meter and the electromagnetic brake is confirmed to be negligibly small. T_{brake} increased linearly with the decrease of n and reaches maximum preceding the stopping of single circular cylinder blade rotation. The torque characteristics are similar to those of the Savonius wind turbines, which are drag type vertical axis wind turbines, as shown in Figs. 1-2 and 1-3. As described in the Section 4.5, the relationship between the lift coefficient acting on the single circular cylinder blade C_L and the tip speed ratio λ was predicted as shown in Fig. 4-19, based on this result of loaded experiments and the torque equilibrium acting on the steadily rotating single circular cylinder blade. The value of C_L was almost zero at $\lambda = \lambda_{max}$ and increased linearly with decreasing λ, reaching a maximum at $\lambda = 0$. From the relationship between C_z and α shown in Fig. 4-2, when C_z is smaller than 0, the fluid force of the LV increased with decreasing α and a larger rotational force acted on the single circular cylinder blade. This phenomenon was well shown in the change of C_L in Fig. 4-19. When the load is not applied by the electromagnetic brake and λ is at its maximum, C_z was zero, i.e., no rotational force was generated, and as the load increases and λ approaches zero, C_z became smaller and the rotational force increased.
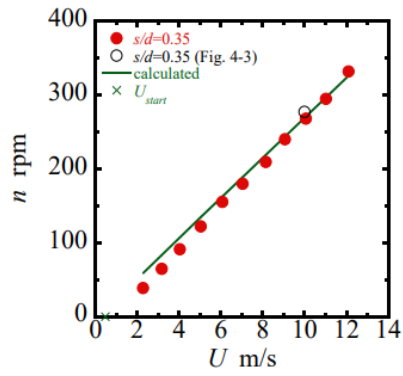
Fig. 4-6 Rotational speed vs. flow velocity for prototype model with s/d=0.35 (un-loaded experiment).
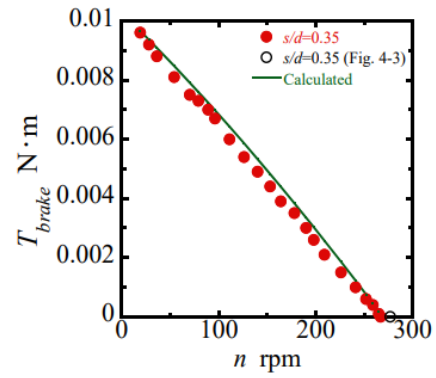

Fig. 4-7 Load torque vs. notational speed for prototype model with s/d=0.35 at U=10m/s (loaded experiment).

4.4 Influences of configuration factors on results of loaded and un-loaded experiments

4.4.1 Gap ratio s/d

Figure 4-8 shows the relationship between n and U when s/d is set at a certain value in the range $0.3 < s/d < 0.5$ obtained through the un-loaded experiments. The open symbols show the experimental results obtained in Fig. 4-3 and the solid lines show the prediction by the method proposed in Section 4.5. The cross symbols on the U-axis show U_{start} calculated in Section 4.5. The value of U_{start} was 0.47-0.5m/s for $s/d = 0.35$-0.5, which was lower than the minimum flow velocity of the wind tunnel. At $s/d = 0.3$, the rotational oscillation was observed as U increases, but the single circular cylinder blade did not attain the steady rotation over the whole range of U in this experiment. At $s/d = 0.35$-0.5, the steady rotation was obtained at the minimum flow velocity $U \simeq 2$m/s, and n increased almost proportionally to U. Over the whole range of U, n took maximum at $s/d = 0.35$ and decreased with the increase of s/d.

Figure 4-9 shows the relationship between T_{brake} and n at $U = 10$m/s for $s/d = 0.35$-0.5 obtained through the loaded experiments. The solid lines show the relationship predicted by the calculation and the open symbols on the n-axis ($T_{brake} = 0$) show the experimental results for respective values of s/d at $U = 10$m/s in Fig. 4-3. This relationship between T_{brake} and n was almost linear at $s/d = 0.35$ as mentioned in Section 4.3, but it deformed into slightly upward convex curve with the increase of s/d. T_{break} decreased over the whole region of n with the increase of s/d. $[T_{brake}]_{max}$ and n_{max} decreased with the increase of s/d, while n_{min} was almost constant regardless of s/d.
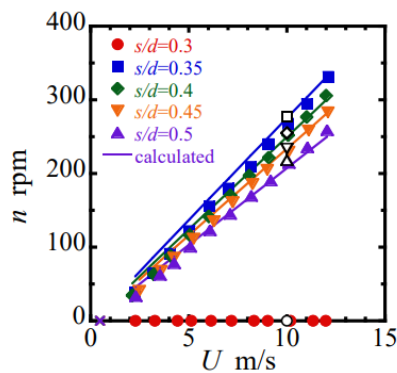

Fig. 4-8 Rotational speed vs. flow velocity for prototype model at each value of s/d, compared with calculation (un-loaded experiments).
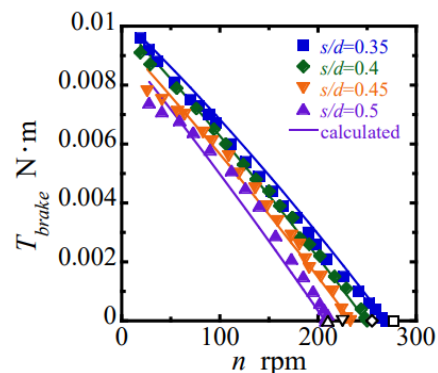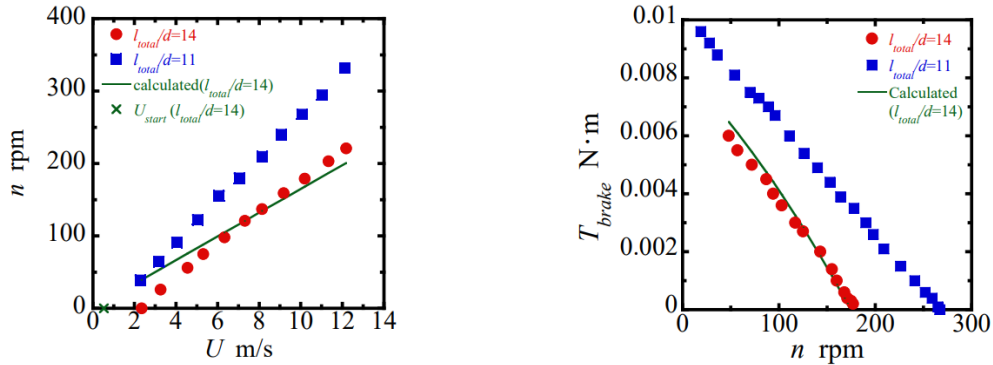
Fig. 4-9 Load torque vs. rotational speed for prototype model at $U = 10$m/s for each value of s/d, compared with calculation (loaded experiments).

4.4.2 Blade length ratio l_{total}/d

Figure 4-10 shows results of the un-loaded and the loaded experiments for the turbine with a blade longer, i.e., $l_{total}/d = 14$, than that of prototype model wind turbine. Blue symbols show the experimental results of the prototype model ($l_{total}/d = 11$) shown in Figs. 4-6 and 4-7 and the solid lines show the prediction by the

method to be proposed in Section 4.5. The cross symbol on the U-axis in Fig. 4-10(a) shows U_{start} calculated in Section 4.5. While the prototype model attained terminal rotation at the lowest flow velocity of wind tunnel $U \simeq$ 2m/s, the $l_{total}/d = 14$ wind turbine remained $n = 0$ at this velocity, started rotating near $U =$ 3m/s and then n increased linearly with U remaining considerably smaller than n of the prototype model over the whole range of U as seen in Fig. 4-10(a). The calculated value of U_{start} was larger than that of the prototype model shown in Fig. 4-6. The influence of cylinder blade length was more remarkable in the result of the loaded experiments at $U = 10$m/s as seen in Fig. 4-10(b). T_{brake} for the longer blade was considerably smaller over the entire region of $n_{min} < n < n_{max}$. n_{min} was much larger than and n_{max} was much smaller than those of the prototype model, making the range of n for $T_{brake} > 0$ quite narrower.

(a) Rotational speed vs. flow velocity (un-loaded experiments)

(b) Load torque vs. rotational speed (loaded experiments)

Fig. 4-10 Influence of the cylinder blade length ($s/d = 0.35$, $W/d = 1$). Blue symbol: Prototype model ($l_{total}/d = 11$), Red symbol: Long cylinder blade ($l_{total}/d = 14$).

4.4.3　Width ratio of ring-plate W/d

Figure 4-11 shows the relationship between n and U obtained through un-loaded experiments using various width ring-plates with $W/d = 0.75$-3. The linear increase of n with U was observed for all W/d's. The minimum flow velocity to sustain terminal rotation was $U = 6$m/s for $W/d = 0.75$, $U = 3$m/s for $W/d = 3$, and lower than the minimum flow velocity of the wind tunnel $U \simeq$ 2m/s for other W/d's. Fig. 4-12 shows the relationship between W/d and n at $U = 10$m/s obtained from Fig. 4-11. The rotational speed n increased almost linearly as W/d increases from 0.75 to 1.75, took the maximum at $W/d = 2$, and gradually decreased as W/d increases at $W/d \geq 2.5$.

Figure 4-13 shows influence of the width ratio on the relationship between T_{brake} and n at $U = 10$m/s by the loaded experiments. When $1.5 \leq W/d \leq 3$, n decreased linearly with the increase of T_{brake} and the value of T_{brake} was considerably larger over the whole range of measurement compared with the case of the

prototype model ($W/d = 1$). n_{max} for these ring-plates was also quite larger than that of the prototype model, while n_{min} was slightly affected by W/d. In the case of $W/d = 0.75$, the value of T_{brake} was much smaller than the other cases. n_{min} was remarkably larger and n_{max} was considerably smaller than those of the prototype model, resulting in a very narrow range of n for $T_{brake} > 0$. The relationships between $[T_{brake}]_{max}$, n_{min}, n_{max} and W/d are shown in Fig. 4-14. $[T_{brake}]_{max}$ increased rapidly at $W/d = 0.75$ to 1.25, took the maximum at $W/d = 1.25$, and decreased in the range of $W/d = 1.25$ to 3. While the plots for n_{min} were scattered and it was difficult to find a systematic dependence on W/d, although it seemed to take the maximum at $W/d = 0.75$. The tendency of dependence of n_{max} on W/d agreed well with that of n at $U = 10$m/s in un-load experiments shown in Fig. 4-12. The value of W/d which the maximum n_{max} obtained was larger than that which the maximum $[T_{brake}]_{max}$ obtained.

The above experimental results confirmed that the magnitude of the driving torque of NV strongly depends on W/d, and that $[T_{brake}]_{max}$ corresponding to the output load torque became maximum at $W/d = 1.25$, 1.3 times larger than that of the prototype model.
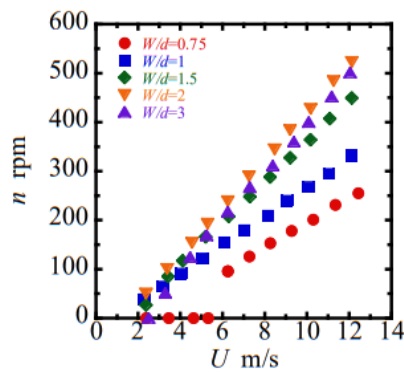

Fig. 4-11 Rotational speed vs. flow velocity for each value of W/d ($l_{total}/d = 11$, $s/d = 0.35$, un-loaded experiments).
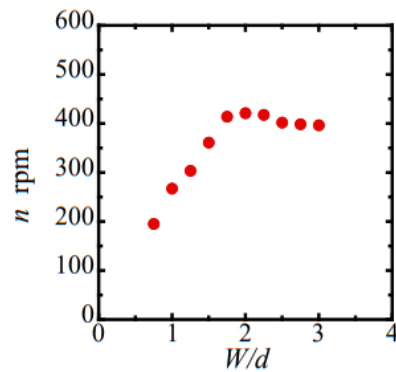
Fig. 4-12 Rotational speed vs. width ratio of ring-plate at $U = 10$m/s ($l_{total}/d = 11$, $s/d = 0.35$, un-loaded experiments).

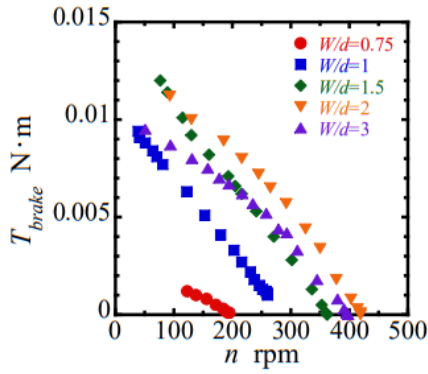Fig. 4-13 Load torque vs. rotational speed at U=10m/s for each value of W/d (l_{total}/d =11, s/d=0.35, loaded experiments).
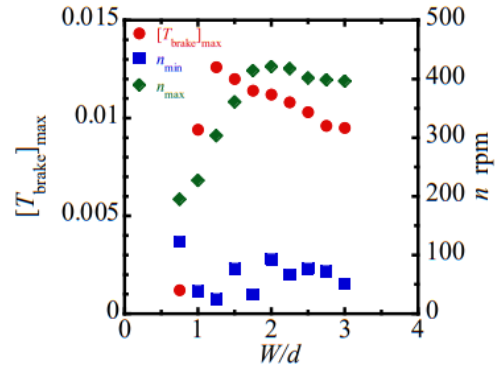
Fig. 4-14 $[T_{brake}]_{max}$, n_{min}, and n_{max} vs. width ratio at U=10m/s (l_{total}/d =11, s/d = 0.35, loaded experiments).

4.4.4　Flange separation length ratio l_F/d

The influence of the flanges attached to the longer cylinder blade ($l_{total}/d = 14$) was investigated through the un-loaded and the loaded experiments for the ring-plates with three selected values of $W/d = 1$, 1.5, and 2, while keeping the gap ratio fixed at $s/d = 0.35$. The separation of two flanges in a pair, l_F, was varied so as to make $l_F/d = 3$-6, and they were arranged at $\pm l_F/2$ from the center radius of the ring-plate $D/2$. The value $l_F = 3d$ was the minimum estimation of the span wise length of NV at $W/d = 1$. Fig. 4-15 shows the relationship between n and U in un-loaded experiments and Fig. 4-16 shows the relationship between T_{brake} and n at $U = 10$m/s in loaded experiments for $W/d = 1$ and the separation ratio $l_F/d = 3$-6. In these figures, the experimental results without flanges indicated as $l_F/d = \infty$ are also shown for comparison. The open symbols in Fig. 4-16 shows the results of the un-loaded experiments in Fig. 4-15 for respective values of l_F/d. As seen in Fig. 4-15, the rotational speed n increased linearly with U as the case without flanges, and influence of the flanges were significant but not so large, i.e., n was maximum at $l_F/d = 4$ over the whole velocity range of measurement. The influence of flanges on the relationship between T_{brake} and n in the loaded experiments was remarkable as seen in Fig. 4-16. Although T_{brake} was expressed as a linear decreasing function of n for all the values of l_F/d, it was definitely larger than the case without flanges when $l_F/d = 4$ and 5. $[T_{brake}]_{max}$ and n_{max} were also enhanced by the flanges with these two values of l_F/d, while n_{min} became lower by attaching the flanges for all the values of l_F/d.

In order to investigate influence of W/d on the effect of flanges, the loaded and un-loaded experiments for ring-plates with $W/d = 1.5$ and 2 were also conducted. These values of W/d were selected because n of unloaded experiments in Fig. 4-12 was maximum at $W/d = 2$ and $[T_{brake}]_{max}$ in Fig. 4-14 was maximum at $W/d = 1.5$. Fig. 4-17 shows the relationship between n at $U = 10$m/s in un-loaded experiments and l_F/d for the three values of W/d. The horizontal broken lines show the experimental results without flanges regarded

as $l_F/d = \infty$. In the case of $W/d = 1$, although it was minimum at $l_F/d = 5.5$ and maximum at $l_F/d = 4$ slightly deviating from the horizontal line for $l_F/d = \infty$, n depended on l_F/d only slightly, being nearly equal to the value without flanges. In the case of $W/d = 1.5$ and 2, the plots of n dropped around on the respective horizontal lines shown $l_F/d = \infty$ at $l_F/d > 5.5$-6, and n decreased rapidly with decreasing l_F/d.

In Figs. 4-18(a) and (b), $[T_{brake}]_{max}$, n_{min} and n_{max} obtained by loaded experiments shown in Fig. 4-17 are plotted against l_F/d for the three values of W/d, where the broken lines show the experimental results for the case without flanges ($l_F/d = \infty$). Fig. 4-18(a) shows that $[T_{brake}]_{max}$ at $W/d = 1$ and 1.5 increased with decreasing l_F/d from ∞ and reached the maximum value at a certain value of l_F/d depending on W/d, and then decreased with the decrease of l_F/d. These maximum values of $[T_{brake}]_{max}$ were significantly larger than that without flanges, especially for the case $W/d = 1$. Fig. 4-18(b) shows that the flanges had an effect to decrease n_{min}. The tendency of dependence of n_{max} on l_F/d in each W/d agreed well with that of n at $U = 10$m/s in un-load experiments shown in Fig. 4-17. For $W/d = 1.5$ and 2, n_{max} and n_{min} decreased with the decrease of l_F/d in a similar tendency. For $W/d = 1$, n_{min} became slightly lower when l_F/d is smaller, but both n_{max} and n_{min} kept, generally speaking, almost constant value equal to those without flanges irrespective of l_F/d.

The effect of flanges was most remarkable with the combination of $W/d = 2$ and $l_F/d = 6.5$, i.e. $[T_{brake}]_{max}$ was 3.7 times larger and the rotational speed range was 2.2 times larger as compared without flanges at $l_{total}/d = 14$ and $W/d = 1$. The value of $[T_{brake}]_{max}$ and rotation range of this combination were 2.3 times and 1.2 times respectively larger than those of the prototype model ($W/d = 1$, $l_{total}/d = 11$). The effects of flange attachment are considered to be brought by separating the single circular cylinder blade into the NV forming region and the drag affected region, and, by blocking the secondary flow induced by the centrifugal force. The attachment of flanges is expected to be a promising technique for performance enhancement by properly selecting the combination of values of W/d and l_F/d.
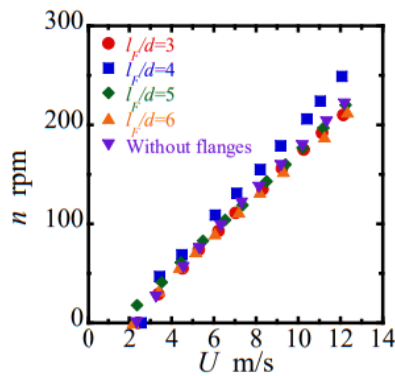

Fig. 4-15 Rotational speed vs. flow velocity for circular cylinder blade with flanges ($s/d = 0.35$, $l_{total}/d = 14$, $W/d = 1$, un-loaded experiments).
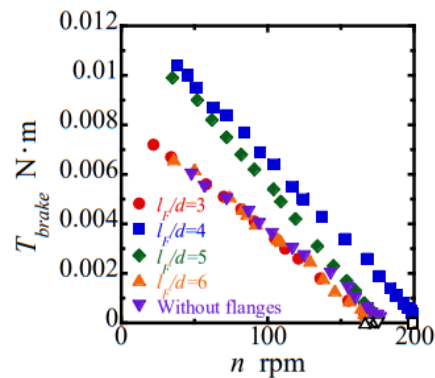
Fig. 4-16 Load torque vs. rotational speed for each value of l_F/d ($W/d = 1$, $s/d = 0.35$, $l_{total}/d = 14$, $U = 10$ m/s, loaded experiments).
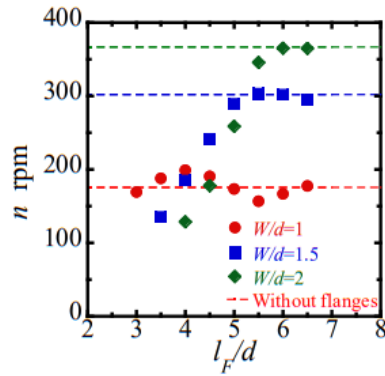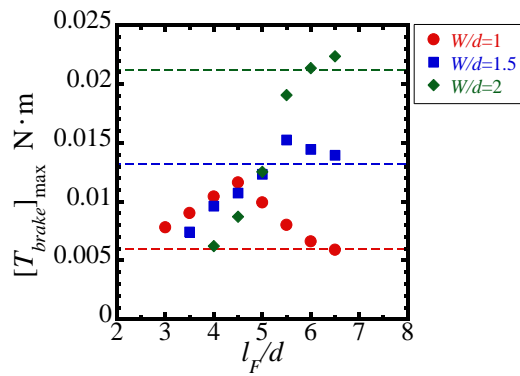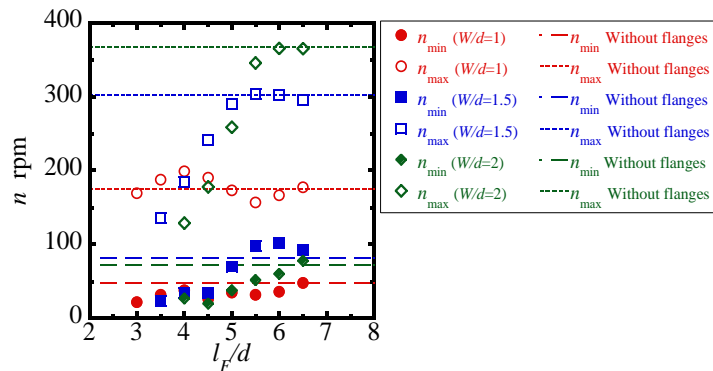
Fig. 4-17 Rotatinal speed vs. flange separation at U=10m/s in un-loaded experiments for ring-plates with various width ratio. Broken lines are for the case without flanges.

(a) Maximum brake torque vs. separation ratio

(b) n_{max} and n_{min} vs. separation ratio

Fig. 4-18 Influence of flange separation ratio under loaded condition for each value of W/d (s/d = 0.35, l_{total}/d = 14, U = 10m/s). Horizontal broken lines are for the case without flanges.

4.5 Prediction method for rotational speed and load torque

4.5.1 Equilibrium of torques acting on wind turbine

When the circular cylinder blade rotates at a constant rotation speed at the loaded condition, the equilibrium of torques acting on the wind turbine is expressed by Eq. (4-1).

$$2T_{NV} = 2T_{drag} + T_{fric} + T_{brake} \qquad (4-1)$$

Here, T_{NV} is the driving torque by the lift force of NV acting on one side of the circular cylinder blade, T_{drag} is fluid resistance torque to the rotational direction acting on one side of the circular cylinder blade, T_{fric}, is the friction torque by the ball bushing, and T_{brake} is the load torque added by the electromagnetic brake. Applying the equation proposed by Kato et al., (2012) [1] for the lift force F_{NV} of NV, T_{NV} is written as

$$T_{NV} = F_{NV} * r_{NV} = \frac{1}{2} C_L \rho d l_{NV} U^2 * r_{NV} , \qquad (4-2)$$

where ρ is the density of air, C_L is the lift coefficient of F_{NV}, l_{NV} is the span wise length of the forming region of NV on the circular cylinder blade, and r_{NV} is the distance to the point of application of F_{NV} from the rotation axis. The drag force F_{drag} is assumed to be proportional to the product of the dynamic pressure defined by the rotational velocity V and the frontal area expressed as $d * l_{drag}$. Here, l_{drag} is the span wise length of the area where the drag is acting on one side of the circular cylinder blade. Thus, T_{drag} is written as

$$T_{drag} = F_{drag} * r_{drag} = \frac{1}{2} C_D \rho d l_{drag} V^2 * r_{drag} . \qquad (4-3)$$

The representative velocity V is defined as the rotational velocity at the point of application of F_{drag} separated from the axis by a distance r_{drag}, i.e.

$$V = \frac{2\pi n r_{drag}}{60} . \qquad (4-4)$$

Note that the physical meanings of l_{NV}, l_{drag} and V are definite, but their definitions are more or less arbitrary.

The results of loaded experiments showed that frictions of the torque meter and the electromagnetic brake with zero load setting are negligible. Hence, the friction torque T_{fric} comes from the friction at the ball bushing and then is given by Eq. (4-5).

$$T_{fric} = F_{fric} * r_{shaft} = \mu m g * r_{shaft} , \qquad (4-5)$$

where μ is the friction coefficient of the ball bushing, m is the mass of the rotating shaft and circular cylinder blade, g is the gravitational acceleration, and r_{shaft} is the radius of the driving shaft. The nominal value of μ = 0.002 both for static and dynamic conditions [4]. Therefore, T_{fric} has a constant value regardless of the flow velocity U and the rotational speed of the circular cylinder blade n.

4.5.2 Estimation of lift and drag coefficient using results of loaded experiments

Generally speaking, C_L, l_{NV}, and r_{NV} in Eq. (4-2) and C_D, l_{drag}, and r_{drag} in Eq. (4-3) are considered to be

dependent on λ. The present authors conducted numerical simulation on a two cylinder blades wind turbine essentially equivalent to the prototype model of this study [3]. Fig. 4-19 shows the relationship between C_L and λ ($= V/U$) obtained by this simulation, where l_{NV} and r_{NV} in Eq. (4-2) are defined as

$$l_{NV} = 3d, \tag{4-6}$$

$$r_{NV} = \frac{D}{2}. \tag{4-7}$$

This relationship is approximated by a linear function of λ as Eq. (4-8),

$$C_L = C_{la} - C_{lb}\lambda, \tag{4-8}$$

where the value of C_{la} and C_{lb} are determined as $C_{la} = 0.901$ and $C_{lb} = 3.68$ by the least-square method.

In this chapter, it is assumed that Eq. (4-8) commonly applies to all the conditions and the values of above constants are determined by using the data of T_{brake} vs. n of the loaded experiments as follows.

The relationship between T_{brake} and n is approximated by a linear function and the value of T_{brake} at $n = 0$ ($[T_{brake}]_{n=0}$) is obtained by the extrapolation. Since $T_{drag} = 0$ and $\lambda = 0$ at $n = 0$, Eq. (4-9) leads

$$2[T_{NV}]_{\lambda=0} = [T_{brake}]_{n=0} + T_{fric}. \tag{4-9}$$

$[T_{NV}]_{\lambda=0}$ at the flow velocity U is determined from the result of loaded experiment in Fig. 4-7 and T_{fric} is estimated by Eq. (4-5). By applying this value of T_{NV} to Eq. (4-2), together with using Eqs. (4-6) and (4-7), the value of C_L at $\lambda = 0$, i.e., C_{la} in Eq. (4-8), is obtained. For the case of prototype model with $s/d = 0.35$, $[T_{NV}]_{\lambda=0}$ determined from the data in Fig. 4-7 and the experimental conditions in Table 2-1 lead

$$C_{la} = [C_L]_{\lambda=0} = 0.92. \tag{4-10}$$

Since this value of C_{la} is very close to that obtained by the above-mentioned numerical simulation, the value of C_{lb} is assumed also to be equal to that of numerical simulation, because there is no other way at the present stage. Thus, Eq. (4-8) is rewritten as

$$C_L = 0.92 - 3.68\lambda \tag{4-11}$$

for the prototype model with $s/d = 0.35$. The two functions for C_L are compared in Fig. 4-19, showing good agreement between them.

The value of C_D is determined by the following procedure using Eq. (4-11). When $T_{brake} = 0$, Eq. (4-1) gives

$$T_{drag} = T_{NV} - \frac{1}{2}T_{fric}. \tag{4-12}$$

Here, T_{NV} is calculated by Eqs. (4-2), (4-6), (4-7) and (4-11) since λ at $T_{brake} = 0$ is determined from $n_{\max}$ in Fig. 4-7, and T_{fric} by Eq. (4-5). The variables r_{drag} and l_{drag} in Eqs. (4-3) and (4-4) are defined as:

$$r_{drag} = \frac{D}{2} \tag{4-13}$$

and the effective length for the drag force on the single circular cylinder blade

$$l_{drag} = \frac{L}{2} - l_{NV}. \tag{4-14}$$

By assuming that $l_{NV} = 3d$ as Eq. (4-6), the following value of C_D is obtained for the prototype model.

$$C_D = 2.73 \, . \tag{4-15}$$

The above value of C_D is quite larger than the drag coefficient of a single circular cylinder in uniform flow. This is because: 1) the representative velocity V defining C_D is lower than the velocity near the tip-end, 2) the effect of tip-end of single circular cylinder blade is neglected, and 3) the definition of the span wise length of acting region of drag force on the single circular cylinder blade (l_{drag}) depends on l_{NV} which is determined arbitrary. In this study, C_D is assumed to be constant although it can depend on λ based on the dimensional analysis.
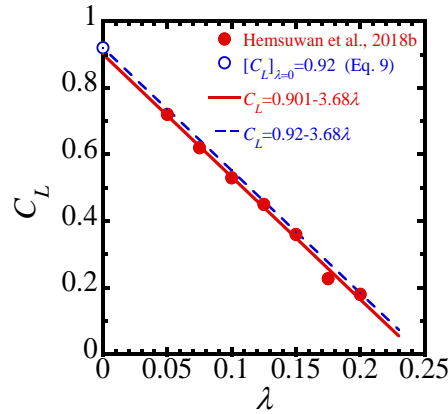
Fig. 4-19 Lift coefficient vs. velocity ratio by experimental estimation compared with numerical result.

4.5.3 Prototype model

The relationship between n and T_{brake} of loaded experiment at $U = 10\text{m/s}$ calculated by the expressions and values for C_L and C_D given in Subsection 4.5.2 is presented in Fig. 4-7 compared with the measurement result. The relationship between U and n of un-loaded test is also calculated and shown in Fig. 4-6 to compare with the measurement, where the flow velocity U_{start} at which the single circular cylinder blade starts rotating is calculated by applying the criterion

$$2T_{NV} \geq T_{fric} = \mu M g * r_{shaft} \, . \tag{4-16}$$

The good agreement between the calculated and measured results in Figs. 4-6 and 4-7 indicates that the Eq. (4-8) and values of C_{la}, C_{lb}, and C_D are proper and appropriate.

4.5.4 Gap ratio s/d

It is considered that the lift coefficient C_L depends strongly on s/d while the drag coefficient C_D is affected only slightly by s/d. Therefore, it is assumed that Eq. (4-8) for the lift coefficient applies but values of the constants C_{la} and C_{lb} are dependent on s/d and that the drag coefficient is equal to that of the case $s/d = 0.35$ as given by Eq. (4-15). For a value of s/d, C_{la} and C_{lb} are determined from the result of loaded experiments

by the following procedure.

(1) C_{la} is determined from $[T_{brake}]_{n=0}$ by the same way as that for $s/d = 0.35$, where Eqs. (4-6) and (4-7) are applied for the representative values of l_{NV} and r_{NV}.

(2) V and λ at $T_{brake} = 0$ are calculated from n_{max}, defined as V_{max} and λ_{max} respectively.

(3) T_{drag} at V_{max} is determined by Eqs. (4-3), (4-4) and (4-13) using $C_D = 2.73$, and T_{NV} at λ_{max} is determined from $T_{NV} = T_{drag} + (1/2)T_{fric}$ obtained by putting $T_{brake} = 0$ in Eq. (4-1).

(4) $[C_L]_{\lambda=\lambda max}$ is calculated applying T_{NV} thus determined to Eq. (4-2) using Eqs. (4-6) and (4-7).

(5) C_{lb} is determined by C_{la} and $[C_L]_{\lambda=\lambda max}$.

In Fig. 4-20, C_{la}, C_{lb} and $\lambda_{max} = C_{la}/C_{lb}$ calculated by this procedure are plotted against s/d, where λ_{max} obtained from n_{max} of the load experiments are also plotted for comparison. Although calculated value of λ_{max} was larger than that obtained from the results of load experiments, the difference was only slight over the entire range of s/d. C_{la} was almost constant while C_{lb} increased with the increase of s/d. Therefore, C_L decreases with increasing s/d over the whole range of λ. The relationships between n and U under un-loaded condition, and between T_{brake} and λ under loaded condition were calculated for each value of s/d by applying C_{la} and C_{lb} in Fig. 4-20. The results are shown in Fig. 4-8 and Fig. 4-9 as the solid lines. For the relationship between n and U in Fig. 4-8, the calculated values agreed well with the experimental results for all s/d. The flow velocity U_{start} at which the single circular cylinder blade starts rotating was calculated by Eq. (4-16) using C_L at $\lambda = 0$, i.e., C_{la} shown in Fig. 4-20. The agreement was fairly well also for the relationship between T_{brake} and n in Fig. 4-9, but deviation of the calculated curve from the experimental value became more significant in the middle range of n when s/d is larger.

The good agreement between the experimental results and the prediction values by calculation for various s/d proves that the assumptions for F_{NV} and F_{drag} are reasonable.
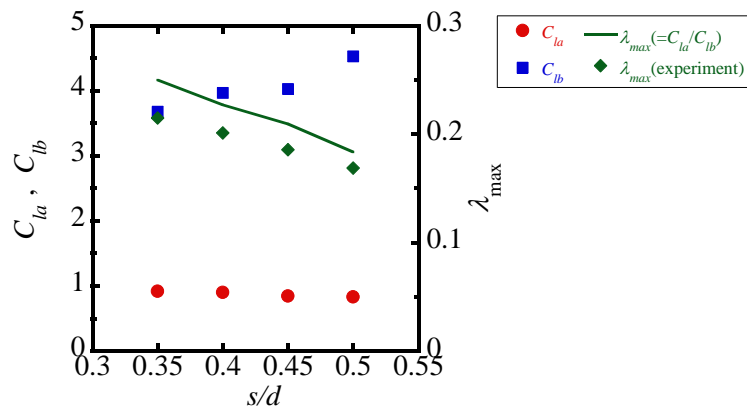

Fig. 4-20 Constants in Eq. (4-8) and λ_{max} vs. gap ratio.

4.5.5 Blade length ratio l_{total}/d

When the single circular cylinder blade is longer while using the same ring-plate with the equal gap ratio, i.e., $W/d = 1$ and $s/d = 0.35$, F_{drag} increases because the region exposed to the drag force becomes larger, and the rotational velocity near the tip of single circular cylinder blade becomes higher and the tip end induces larger additional resistance. While influence of blade length on the lift force F_{NV} is not clear but considered to be significant because of increase of secondary flow due to centrifugal force. Therefore, the values of constants in Eq. (4-8) for C_L and C_D for the longer cylinder blade ($l_{total}/d = 14$) are determined by applying the same procedure to the result of the loaded experiments in Fig. 4-7 as applied for the prototype model with $s/d = 0.35$. As the result, $C_L = 0.74\text{-}3.68\lambda$ and $C_D = 8.1$ were obtained for the lift and the drag coefficient of the $l_{total}/d = 14$ cylinder blade. Comparing the values of these coefficients with the respective counterparts of the prototype model given by Eqs. (4-11) and (4-15), C_D was three times larger for the longer blade while C_L was a slightly smaller. The relationships between n and U under un-loaded condition, and, between T_{brake} and n under loaded condition were calculated by using the above values for the coefficients, and the results are shown in Figs. 4-10(a) and (b) as the solid lines. Good agreement between the calculated and measured results was obtained both for the un-loaded and the loaded experiments. The most significant deviation of calculation was observed in low velocity region of Fig. 4-10(a) for un-loaded experiments.

4.6 Evaluation of performance

4.6.1 Influence of gap ratio on the performance of prototype model

In order to evaluate the efficiency of the wind turbine, the power coefficient C_p for converting the wind energy to the mechanical power defined by Eq. (4-17) is generally used.

$$C_p = \frac{\omega T_{brake}}{0.5\rho A U^3},\qquad (4-17)$$

where ω (= $2\pi n/60$) is the angular velocity of the driving shaft and A (= $\pi l_{total}^2/4$) is the swept area of the rotating cylinder blade. Another measure for the performance of wind turbine is the operation range of the velocity ratio given by λ_{min} and λ_{max}.

Figure 4-21 shows the relationship between C_p and λ (= V/U) for the prototype model with s/d = 0.35 obtained from the experimental results shown in Fig. 4-7, compared with the prediction calculated by using the prediction method. The maximum value of C_p ([C_p]$_{max}$) was 0.0031 at λ (= $\lambda_{[Cp]max}$) around 0.11, which is about 1/2 of λ_{max}, the upper limit of the operation range of velocity ratio. The prediction agreed well with the measurement, showing the approximation of C_L and C_D are appropriate, although the predicted $\lambda_{[Cp]max}$ was slightly larger than the experimental value.

In Fig. 4-22, the maximum power coefficient [C_p]$_{max}$, $\lambda_{[Cp]max}$, λ_{min} and λ_{max} are plotted against s/d, compared with the calculated predictions. There was no significant change in λ_{min} while λ_{max} decreases with the increasing of s/d, that is, the operation range of λ where C_p > 0 became narrower with the increasing of s/d. Both [C_p]$_{max}$ and $\lambda_{[Cp]max}$ decreased with the increasing of s/d. The prediction of [C_p]$_{max}$ was larger than the experimental result at s/d = 0.35, but was smaller than the experimental result at s/d = 0.45 and 0.5. The calculated value of $\lambda_{[Cp]max}$ was less than the experimental for all the cases of s/d.
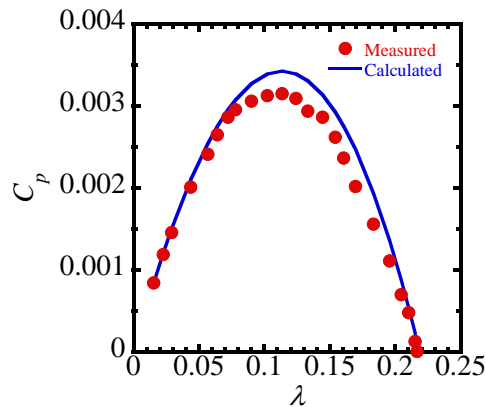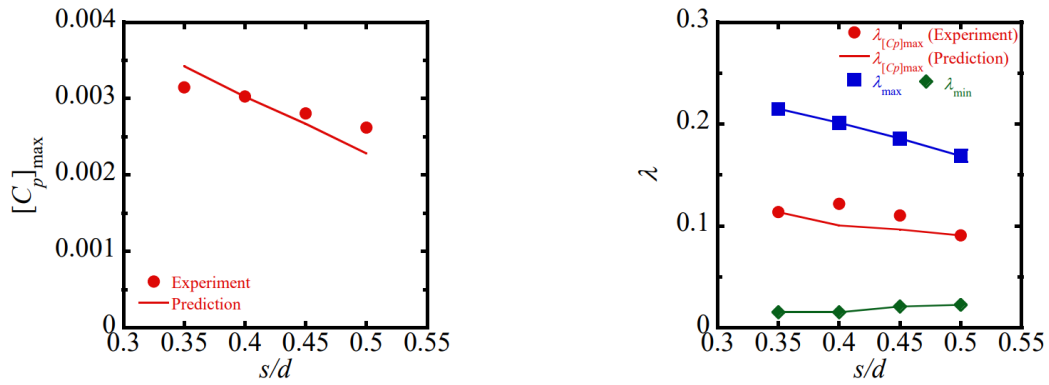

Fig. 4-21 Power coefficient vs. velocity speed ratio for prototype model, with s/d = 0.35 comparing experimental result and predicted result.

(a) Maximum power coefficient vs. gap ratio (b) Operation range of velocity ratio vs. gap ratio

Fig. 4-22 Effect of the gap ratio on performance characteristics.

4.6.2　Effect of width ratio of ring-plate

Figure 4-23 shows the relationship between C_p and λ for the ring-plates with various width ratio with s/d=0.35 obtained from the result of the loaded experiments in Fig. 4-13. In Fig. 4-24, λ_{max}, λ_{min}, $[C_p]_{max}$, and $\lambda_{[Cp]max}$ obtained from Fig. 4-23 are plotted against W/d. These figures show that the operation range of λ became wider by the increase of λ_{max} with the increase of W/d and reached maximum at W/d=2, 1.6 times larger than that of the prototype model (W/d=1). There was no systematic change in λ_{min}. Both $[C_p]_{max}$ and $\lambda_{[Cp]max}$ reached maximum at W/d=2, and $[C_p]_{max}$ became 2.6 times larger than that of the prototype model.
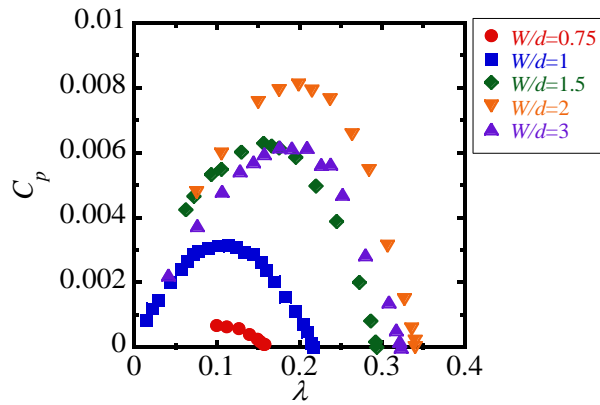
Fig. 4-23 Power coefficient vs. velocity speed ratio for each value of W/d ($l_{total}/d = 11$, $s/d = 0.35$).

65
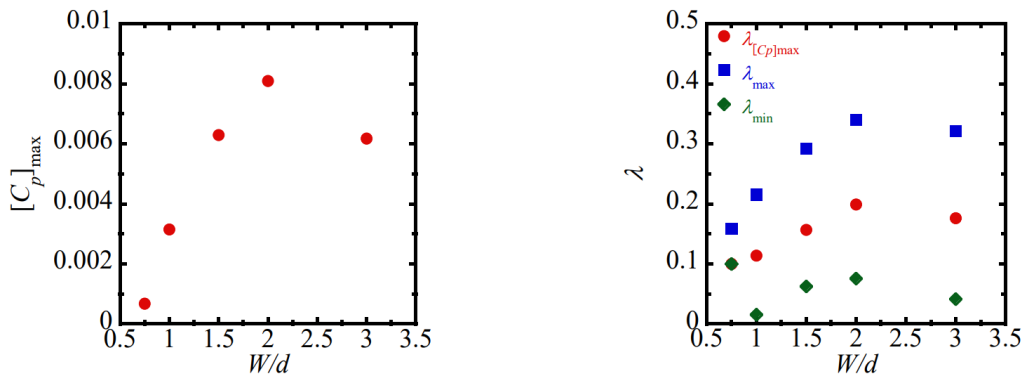
(a) Maximum power coefficient vs. width ratio   (b) Operation range of velocity ratio vs. width ratio

Fig. 4-24 Effect of the width ratio on performance characteristics.

4.6.3 Effect of flange separation length ratio

Effect of the flanges attached to the longer cylinder blade is shown in Figs. 4-25 and 4-26, where the symbol for $l_F/d = \infty$ is the result without flanges shown in Fig. 4-10(b). Fig. 4-25 shows the relationship between C_p and λ calculated from the results of the loaded experiments in Fig. 4-17 for various separation length ratios. There was no significant change of λ_{max} over the measurement range of l_F/d. λ_{min} became maximum at $l_F/d = 4$ but kept almost constant at $l_F/d \geq 4$. Therefore, the operation range of λ did not change at $l_F/d \geq 4$. The maximum value of $[C_p]_{max}$ was also obtained at $l_F/d = 4$, around 1.7 times larger than that without flanges.
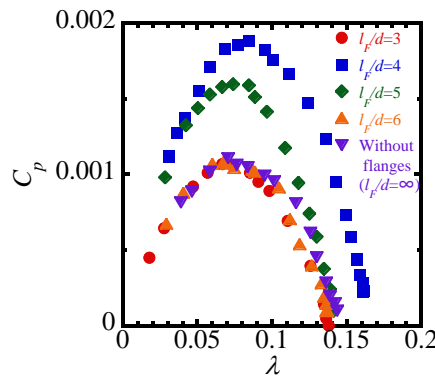
Fig. 4-25 Power coefficient vs. velocity ratio for each value of l_F/d.
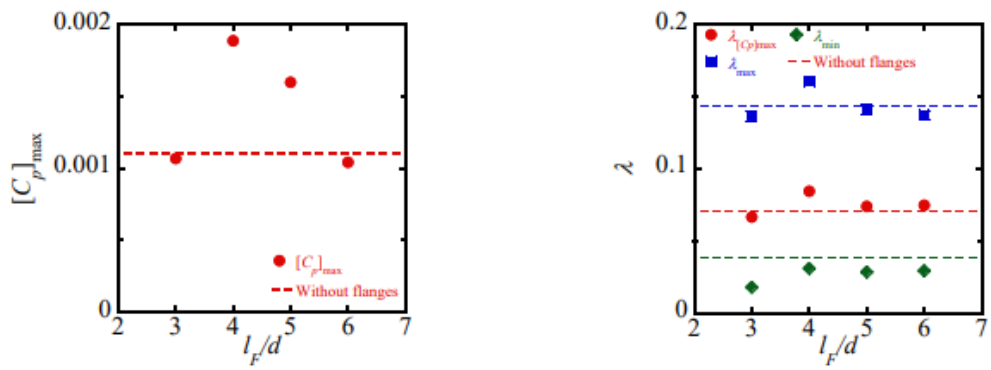
(a) Maximum power coefficient vs. separation length ratio

(b) Operation range of velocity ratio vs. separation length ratio

Fig. 4-26 Effect of flange separation length ratio on performance characteristics of longer cylinder blade turbine ($l_{total}/d = 14$, $s/d = 0.35$).

4.7　Conclusions

A prototype model of the single circular cylinder blade wind turbine was used to measure steady lift forces acting on the circular cylinder blade, and the relationship with the relative attack angle was clarified. The basic rotation and output torque, and performance characteristics of the cylinder blade wind turbine driven by longitudinal vortex (LV) were investigated through wind tunnel experiments, and the effects of several structural parameters were investigated for the development of a practical wind turbine in the future. The conclusions are summarized as follows.

(1) The fluid force coefficient C_z acting on the single circular cylinder blade increased monotonically with the increase of the relative attack angle, which is geometrically determined by the moving velocity of single circular cylinder blade and mainstream velocity. When the gap ratio s/d between the single circular cylinder blade and the ring-plate is less than 0.35, C_z was positive regardless of α, and the rotation stopped by a force acting in a opposite direction that suppresses the rotation even after the initial motion was applied. When s/d is 0.35 or higher, C_z was negative in a given range of α and single circular cylinder blade accelerated in the rotating direction when an initial motion was given. The attack angle increased with the rotational speed and when C_z is reached 0, the acceleration became zero and the single circular cylinder blade rotated steadily.

(2) The terminal rotational speed n of the free-rotating single circular cylinder blade for the increasing flow velocity U was determined to be a constant α in which C_z is 0 regardless of U.

(3) The lift coefficient C_L of NV was well approximated by a decreasing linear function of the velocity ratio λ, and the drag coefficient C_D against the rotation was assumed to be constant by properly defining the span wise lengths of their acting region on the single circular cylinder blade.

(4) By using C_L and the drag coefficient C_D determined from the result of loaded experiments, the relationships between n and U under un-loaded condition, and, between the power coefficient C_p and the velocity ratio λ were fairly well predicted for the widely varying conditions of this chapter.

(5) The wide ring-plate and attachment of the flanges were shown to be promising technique to improve the performance of the wind turbine. At the present stage, the best performance of the wind turbines was obtained for $s/d = 0.35$, $W/d = 2$, and $l_F/d = 4$ with $l_{total} = 280$mm and $d = 20$mm single circular cylinder blades.

References

[1] Kato, N., Koide, M., Tahkahashi, T., Shirakashi, M., 2012. VIVs of a circular cylinder with a downstream strip-plate in cruciform arrangement, Journal of Fluids and Structures, Vol. 30, 97-114.

[2] Koide, M., Takahashi, T. and Shirakashi, M.,2001. Development of a ring-type vortex anemometer for low-velocity wind tunnel experiment, Transactions of the Japan Society of Mechanical Engineers Series B, Vol. 67, No. 657 (2001), pp. 1105-1111.

[3] Hemsuwan, W., Sakamoto, K., Nakada, S., Takahashi, T., 2018b. A longitudinal vortex wind turbine: numerical study, Journal of Wind Engineering and Industrial Aerodynamics, Vol. 180, 213-230.

[4] NIPPON BEARING CO., LTD, Frictional resistance for required thrust, http://www.nb-linear.co.jp/english/technology/friction_thrust.html/(accessed 27 March 2019).

5. Effect of blade configurations of the stepped circular cylinder blade wind turbine

The optimum condition for the stepped circular cylinder blade wind turbine, which has a practical wind turbine configuration, is determined. The effect of the effective length l, number and diameter (N and d) of the stepped circular cylinder blade on the rotation, output torque, and performance characteristics are investigated based on the information obtained from the study of the single circular cylinder blade wind turbine shown in Chapter 4. By setting the effective length of the cylinder blade equal to the formation region of NV and reducing the diameter of the supporting rod between the effective part of the cylinder blade and driving shaft, the output torque and performance is considered to be improved. The driving force of NV acting per stepped circular cylinder blade is investigated by increasing of number of cylinder blades N. The effects of the blade pitch ratio t/d on each characteristic are extensively investigated by combining the conditions of blade number N and blade diameter d.

5.1 Experimental results and discussion

5.1.1 Influence of effective length

The un-loaded and the loaded experiments using the stepped circular cylinder blade wind turbine with blade number $N = 2$ are carried out for the effective blade lengths of l = 40-90mm (l/d = 2-4.5). The experimental results are compared with the cases of the single circular cylinder (Fig. 5-1(a)) and the single circular cylinder blade attached with a pair of flanges (Fig. 5-1(b)) presented in Chapter 4. The stepped circular cylinder blade with an effective length $l \simeq l_{NV}$ and the flange-attached single circular cylinder blade with a separation length $l_F = l$ are expected to show similar flow features such as: i) NV generating the lift force is formed without formation of TVs, ii) the secondary flow by the rotation is suppressed. The following differences between them should be taken into consideration: i) the diameter of the supporting part d' of the stepped circular cylinder blade is much smaller than the blade diameter d of the flanged circular cylinder blade, ii) the outer end of the stepped circular cylinder blade is cut off corresponding to outside the flange for the flanged circular cylinder blade.

Figure 5-2 shows the relationship between the rotational speed n and the flow velocity U when the effective length is set at l = 40-90mm (l/d = 2-4.5) obtained through the un-loaded experiments for the stepped circular cylinder blade wind turbine with N = 2, d = 20mm. Solid black circles show the experimental result of the single circular cylinder blade wind turbine presented in Chapter 4 ($l_{total}/2$ = 140mm). The rotational speed n increased almost proportionally with the flow velocity U for all l, being larger than n of the single circular cylinder blade over the whole range of U where the steady rotation was obtained. The minimum flow velocity at which the steady rotation (minimum flow velocity for rotation: $U_{\min}$) is obtained was $U_{\min} \simeq$ 4m/s for the shortest blade (l = 40mm, l/d = 2), and $U_{\min} \simeq$ 3m/s for all the others. For the single circular cylinder turbine, $U_{\min}$ was 3.3m/s. Fig. 5-3 shows the relationship between $U_{\min}$ and l obtained from Fig. 5-2. The broken line shows the result of single circular cylinder blade ($U_{\min}$ = 3.3m/s) and the blue symbols show the relationship between $U_{\min}$ and l_F of the flanged circular cylinder blade. $U_{\min}$ of the stepped circular cylinder blade was $U_{\min}$ = 3.2m/s at almost l except $U_{\min}$ = 4.3m/s at l = 40mm (l/d = 2). The value of $U_{\min}$ = 3.2m/s was almost the same as those for the single and flanged circular cylinder blade excluding l_F = 90, 100mm (l_F/d = 4.5, 5). Fig. 5-4 shows the relationship between n and l at U = 10m/s obtained from Fig. 5-2. The results of the single and flanged circular cylinder blade are also shown for comparison. A remarkable effect of the stepped circular cylinder blade to enhance the rotation speed was confirmed, i.e., n was about 1.6 times larger at l = 50mm (l/d = 2.5) than that of the single circular cylinder blade shown by the horizontal broken line. The relationship between n and l_F deviated only slightly from that of the single circular cylinder blade, i.e., within ±10% from the horizontal broken line over the range of l_F = 60-130mm (l_F/d = 3.0-6.5). It is considered that the stepped circular cylinder blade with an optimum value of l/d, says 2.5-3, keeps the lift force by NV while largely reduces the fluid resistance force against rotation and/or the mechanical friction force as compared with the single circular cylinder blade.

The experimental results in Fig. 5-4 corresponded well with the results of numerical simulation by the

present authors [1], where it was shown that the lift force by NV is maximum at $l/d \simeq 3$. Compared with the single circular cylinder blade wind turbine, the total length of the stepped circular cylinder blade is shorter, and the diameter of the supporting rod d' is smaller than d. These configurations reduced the drag force against rotation and contributed to the increase of n. The same effect is expected in the flanged circular cylinder blade by suppressing the secondary flow. However, since the attachment of the flanges and the long circular cylinder blade generated the drag force against rotation, the above effect was considered to be cancelled.

(a) Without flange attachment   (b) With flanges
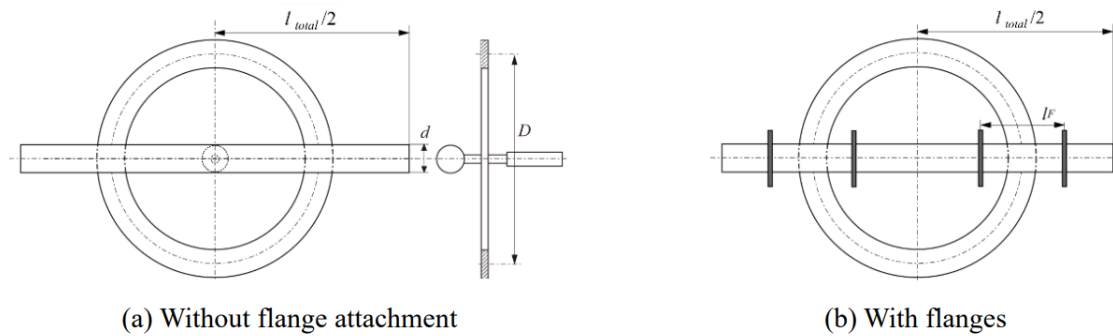
Fig. 5-1 Schematic diagram and parameters of single and flanged circular cylinder blades ($d = 20$mm, $l_{total}/2 = 140$mm).
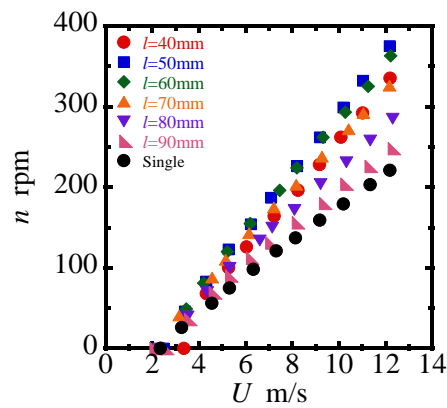
Fig. 5-2 Rotational speed vs. flow velocity through un-loaded experiments for stepped circular cylinder blade turbine ($N = 2$) with various effective length of cylinder blade, compared with single circular cylinder blade.
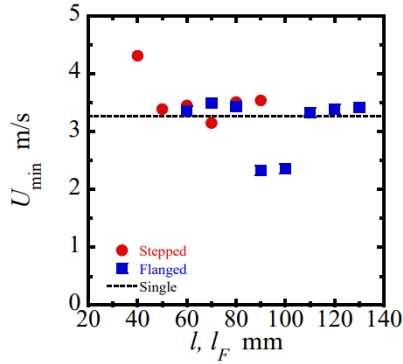
Fig. 5-3 Minimum flow velocity for rotation vs. effective length of stepped cylinder blade turbine (N=2) through un-loaded experiment, compared with $U_{min} \sim l_F$ of flanged circular cylinder blade.
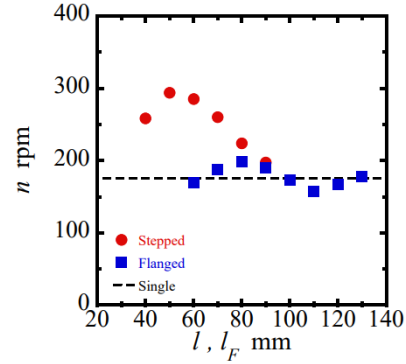
Fig. 5-4 Rotational speed at U=10m/s vs. effective length through un-loaded experiment for stepped cylinder blade turbine (N=2), compared with $n \sim l_F$ of flanged circular cylinder blade.

Figure 5-5 shows influence of l on the relationship between T_{brake} and n at $U = 10$m/s obtained by the loaded experiments. The experimental results of the single circular cylinder blade ($l_{total}/2 = 140$mm) are also shown for comparison. T_{brake} of each l for the same n was larger than that of the single circular cylinder blade, and it was the largest at $l = 60$mm. The relationships of T_{brake} and n were well approximated by linear functions with an almost equal gradient for all l. In Figs. 5-6, 5-7, and 5-8, $[T_{brake}]_{max}$, n_{min}, and n_{max} are plotted against l. The results of the single and flanged circular cylinder blade are also shown. $[T_{brake}]_{max}$ of the stepped circular cylinder blade was larger than that of single circular cylinder and became maximum at $l = 60$mm, which was about 1.7 times larger. $[T_{brake}]_{max}$ of the flanged circular cylinder blade was maximum at $l_F = 90$mm ($l_F/d = 4.5$) and it was about 30% larger than that of the stepped circular cylinder blade. The formation of TVs was prevented for both stepped and flanged circular cylinder blades. However, for stepped circular cylinder blade, when $l \geq 80$mm, TVs were formed near the both tip-ends of the effective region and the lift force acting on the stepped circular cylinder blades reduced. As a result, the maximum value of $[T_{brake}]_{max}$ and the corresponding l_F for the single circular cylinder and flanged circular cylinder blade are considered to be larger than those for the stepped circular cylinder blade. n_{min} of the stepped and flanged circular cylinder blade was lower compared with the single circular cylinder blade. Since n_{min} indicates the rotational speed at which the driving force by NV is formed, the stepped circular cylinder blade made the rational speed for the stationary formation of NV lower than the single circular cylinder blade. However, the values of n_{min} were scattered and the systematic change with respect to l was not confirmed. The variation of n_{max} with l agreed well with the relationship between n and l at $U = 10$m/s shown in Fig. 5-4. This coincidence indicates that the friction torque of the torque meter and the brake is negligibly small when the load of the electromagnetic brake is set to 0.

By using the results of Figs. 5-7 and 5-8, the maximum and the minimum velocity ratio were obtained by the following equations:

$$\lambda_{\max} = \frac{2\pi n_{\max} R}{U} \, , \tag{5-1}$$

$$\lambda_{\min} = \frac{2\pi n_{\min} R}{U} \, , \tag{5-2}$$

where the representative radius R is defined as $R = D/2$. Then, the velocity ratio range over which the wind turbine operates λ_{ope} was obtained as

$$\lambda_{\mathrm{ope}} = \lambda_{\max} - \lambda_{\min} \, . \tag{5-3}$$

Figure 5-9 shows the relationship between λ_{ope} and l, compared with $\lambda_{\mathrm{ope}} \sim l_F$ of the flanged circular cylinder blade. λ_{ope} of the stepped circular cylinder wind turbine was larger than that of singe and flanged circular cylinder blade, and reached maximum at $l = 50$mm, kept the same level at $l/d = 2.5$-3.5 and then decreased with the increase of l/d.

Considering the results of the un-load experiment in Fig. 5-4 and the loaded experiment in Figs. 5-6 and 5-9, the optimum effective length of the stepped circular cylinder blade was obtained in the range of $l = 50$-60mm ($l/d = 2.5$-3, $l_{total}/2 = 102.5$-107.5mm). In this study, the optimum effective length is assumed to be $l/d = 3$, and hence $d = 20$mm, $d' = 6$mm, $l/d = 3$ ($l = 60$mm) and $l_{total}/2 = 215$ mm are used as the dimensions of the prototype stepped circular cylinder blade wind turbine, which was also used in the numerical simulation [2].
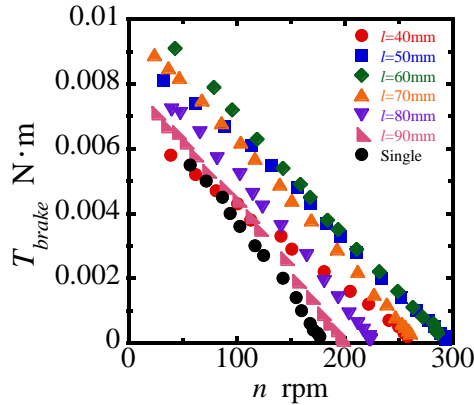
Fig. 5-5 Load torque vs. rotational speed at $U = 10$m/s through loaded experiments for each value of effective length of stepped circular cylinder blade turbine ($N = 2$), compared with single circular cylinder blade turbine.
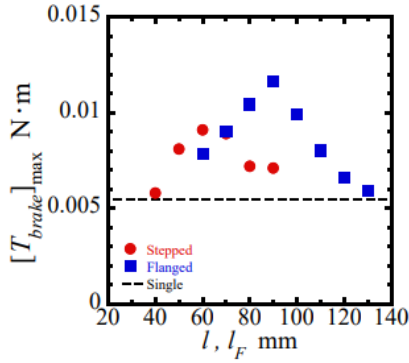
Fig. 5-6 $[T_{brake}]_{max}$ vs. effective length at U=10m/s, compared with single circular cylinder and flanged circular cylinder.
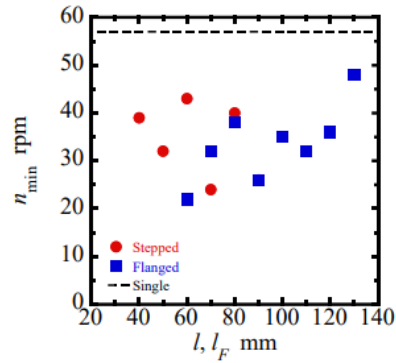
Fig. 5-7 n_{min} vs. effective length at U=10m/s, compared with single circular cylinder and flanged circular cylinder.
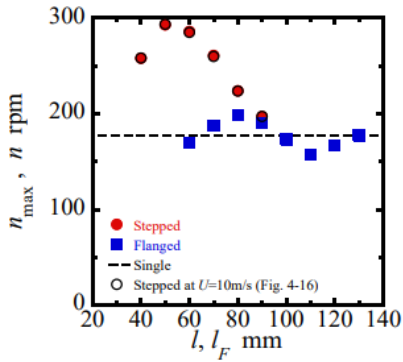
Fig. 5-8 n_{max} vs. effective length at U=10m/s, compared with single circular cylinder and flanged circular cylinder.

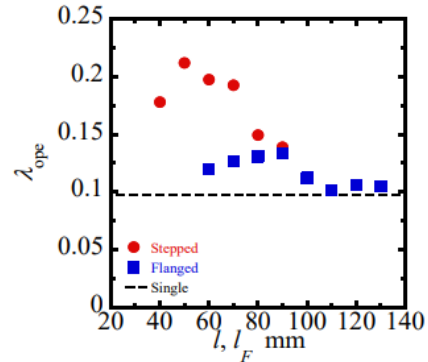Fig. 5-9 Operating velocity ratio at unloaded experiment, compared with single circular cylinder and flanged circular cylinder.

5.1.2   Influence of blade number

The un-loaded and the loaded experiments were carried out by using the stepped circular cylinder blade wind turbine with the optimum blade length determined in the preceding section l = 60mm (l/d = 3, $l_{total}/2$ = 107.5mm) and blade number of N = 2-12.

Figure 5-10 shows the relationship between the rotational speed n and the flow velocity U when the blade number is set at N = 2-12 through the un-loaded experiments. Black solid circles show the experimental result of single circular cylinder blade wind turbine. n was almost proportional with U for all N. The minimum flow velocity for steady rotation was $U_{min} \simeq$ 3m/s at N = 2, 4, and $U_{min} \leq$ 2m/s for the other N's. Fig. 5-11 shows the relationship between n and N at U = 10m/s with the result of the single circular cylinder blade. n gradually increased with the increase of N. When the interference effect by the wake for the rotational motion is negligible, the driving torque T_{NV} and the fluid resistance torque T_{drag} acting on a stepped circular cylinder

75

blade are independent of N. Moreover, when the frictional torque per one blade (T_{fric}/N) is negligibly small or constant, n at $U = 10$m/s is expected to be constant. The gradual increase of n with N in Fig. 5-11 is considered to be caused by the interference effect and/or the decrease of T_{fric}/N. Fig. 5-12 shows the relationship between U_{min} and N obtained from Fig. 5-10 with the result of single circular cylinder blade ($U_{min} = 3.3$m/s). Comparing the results of the stepped circular cylinder blade with that of the single circular cylinder blade, it was almost equal for $N \leq 4$, and was lower for $N \geq 6$. The reason is considered as follows: The interference effect by the wake for rotational motion was stronger in large N and was weaker in small n. Hence, the driving torque acting on the turbine T_{NV} at small n was proportional to N. On the other hand, since T_{fric} was proportional with the mass of turbine m, the increase of T_{fric} was not proportional to N. Since the condition for the steady rotation at $n \sim 0$ was given by $T_{NV} \geq T_{fric}/N$, it is expected that U_{min} for steady rotation decreases with the increase of N.
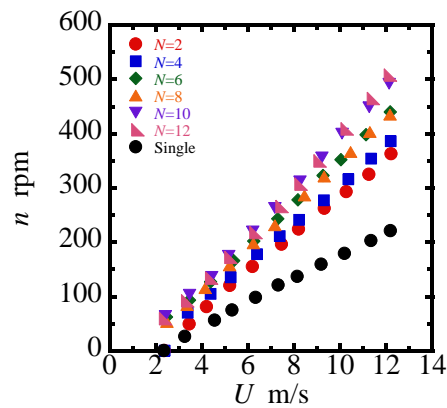
Fig. 5-10 Rotational speed vs. flow velocity at each value of effective blade length through un-loaded experiments at $d = 20$mm, $l = 60$mm, $l_{total}/2 = 107.5$mm compared with single circular cylinder ($d = 20$mm, $l_{total}/2 = 140$mm).
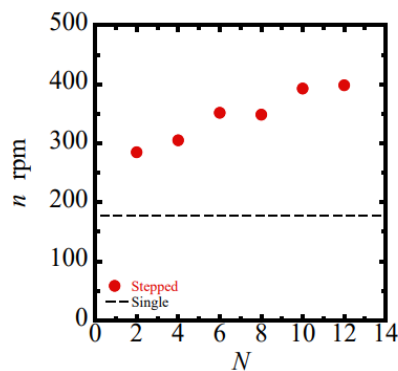
Fig. 5-11 Rotational speed at U=10m/s vs. blade number of stepped cylinder blade turbine through un-loaded experiment.
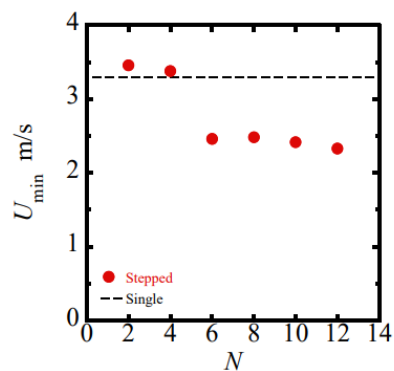
Fig. 5-12 Minimum velocity for rotation vs. blade number of stepped cylinder blade through un-loaded experiment.

Figure 5-13 shows the influence of the blade number on the relationship between T_{brake} and n at $U = 10$m/s in the loaded experiments using the stepped circular cylinder blade wind turbine with the optimum blade length $l = 60$mm ($l/d = 3$, $l_{total}/2 = 107.5$mm). The experimental results of the single circular cylinder ($l_{total}/2 = 140$mm) are also shown for comparison. T_{brake} decreased linearly with the increase of n for all N. For a fixed value of n, T_{brake} was larger at larger N. The gradient of T_{brake} reduction was smaller for $N = 2$ and larger for $N = 6$-12 than that of a single circular cylinder blade. The results of $[T_{brake}]_{max}$, n_{min} at $[T_{brake}]_{max}$, and n_{max} at $T_{brake} = 0$ obtained from Fig. 5-13 are plotted against N with those of the single circular cylinder blade in Figs. 5-14, 5-15, and 5-16. $[T_{brake}]_{max}$ for $N = 2$ was 1.6 times larger than that of the single circular cylinder blade and $[T_{brake}]_{max}$ increased nearly proportionally with N when $2 \leq N \leq 8$, then gradually decreased with N when $8 < N \leq 12$. The maximum value of $[T_{brake}]_{max}$ at $N = 8$ was about 4.2 times larger than that at $N = 2$.

In the stepped circular cylinder blade wind turbine, when the flow pattern around each cylinder blade is same, i.e., when there is no interference effect by the wake for the rotational motion, both T_{NV} and T_{drag} acting on per cylinder blade are independent on N, and therefore, the net driving torque of the wind turbine is considered to be proportional to N. Moreover, when T_{fric} is sufficiently smaller than $[T_{brake}]_{max}$ and can be ignored at $U = 10$m/s, the torque equilibrium is estimated as $T_{brake} = (T_{NV}\text{-}T_{drag})*N$. The experimental results showed that the interference effect does not occur when $N \leq 8$ and occurs when $N > 8$. The plots of n_{min} in Fig. 5-15 were scattered in $n_{min} < 50$rpm and were smaller than that of the single circular cylinder blade except $N = 6$ where a flaw in the experimental procedure may have occurred. As mentioned above, the interference effect is expected not to occur in $N \leq 8$, and T_{fric} becomes smaller relative to the driving torque T_{NV} which increases proportionally with the increasing N. Therefore, n_{min} is expected to decrease with N. This trend was observed in $N \leq 10$, but n_{min} increased sharply at $N = 12$. The change in n_{max} agreed well with the relationship between N and n at $U = 10$m/s shown in Fig. 5-11. It proves that the friction torque to the rotation by the torque meter and the electromagnetic brake is negligibly small.

From the results of Figs. 5-15 and 5-16, the operating velocity ratio λ_{ope} at each N was obtained by the Eqs. (5-1) to (5-3) and the results are shown in Fig. 5-17. λ_{ope} increased with the increase of N in $N \leq 10$ and became maximum at $N = 10$ and decreased at $N = 12$. λ_{ope} of the stepped circular cylinder blade was larger than that of the single circular cylinder blade by about 2 times at $N = 2$ and about 3 times at $N = 10$.
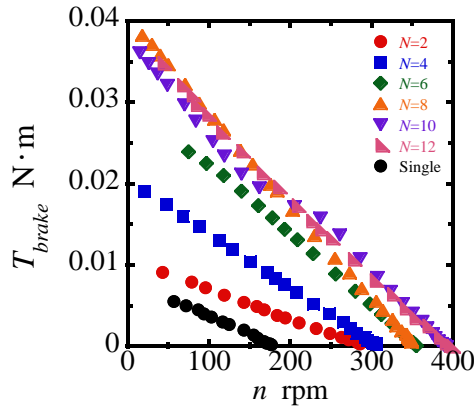
Fig. 5-13 Load torque vs. rotational speed at $U = 10$m/s for each value of blade number through loaded experiments at $d = 20$mm, $l = 60$mm, $l_{total}/2 = 107.5$mm, compared with single circular cylinder ($d = 20$mm, $l_{total}/2 = 140$mm).

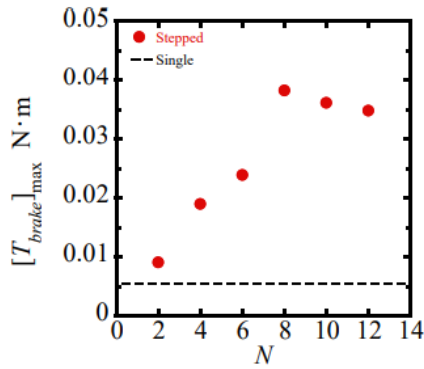
Fig. 5-14 Maximum load torque vs. rotational speed at $U=10$m/s for each value of blade number through loaded experiment.
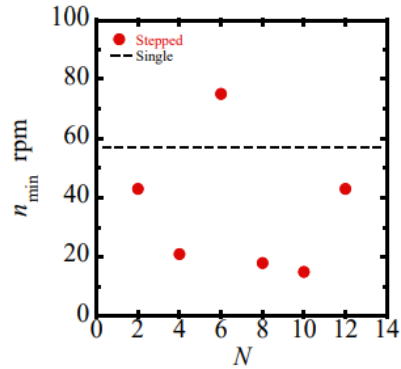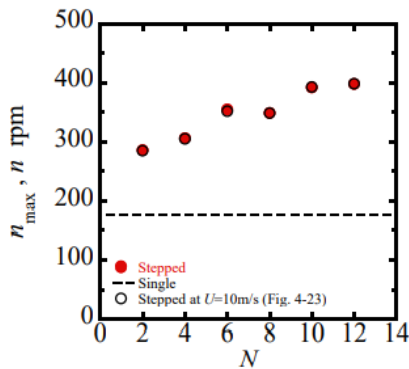

Fig. 5-15 Minimum rotational speed at $[T_{brake}]_{max}$ vs. rotational speed at $U=10$m/s for each value of blade number through loaded experiment.

Fig. 5-16 Maximum rotational speed vs. rotational speed at $U=10$m/s for each value of blade number through loaded experiment.
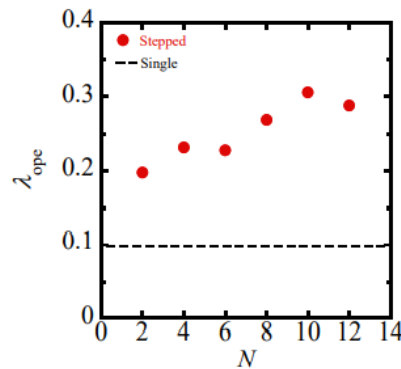
Fig. 5-17 Operating rotation range vs. rotational speed at $U=10$m/s for each value of blade number through loaded experiment.

78

5.1.3 Influence of blade diameter

The results of loaded and un-loaded experiments with different effective diameter d for the stepped circular cylinder blade wind turbine with effective $l = 60$mm and $N = 2$ are shown. Note that the values of l/d and W/d vary with d at constant $l = 60$mm and $W = 20$mm in these experiments. When the gap ratio is constant at $s/d = 0.35$, the geometric similarity of the cross-sectional diameter of NV to the cylinder diameter d is kept, as shown in the visualization results in Chapter 3.

Figure 5-18(a) shows the relationship between s/d and n for each blade diameter d at a constant flow velocity $U = 12$m/s. The stepped circular cylinder blade suddenly started rotating at certain s/d in all d. The critical condition for the gap ratio of $d = 20$mm for the single circular cylinder blade wind turbine was $s/d = 0.35$ as shown in Chapter 4, whereas the critical condition of s/d for the stepped circular cylinder blade wind turbine decreased with increasing d. With an increase in d, the periodicity of NV is considered to be lost at small s/d. The stepped circular cylinder blades rotate at least over $s/d = 0.25$ at all d. This indicates clearly that the stepped circular cylinder blades were driven by the lift force of NV.

Figure 5-18(b) shows the relationship between U and n in un-loaded experiments in each d. The gap ratio was set to $s/d = 0.35$ based on the visualization results shown in Chapter 3 in order to keep the geometric similarity of the cross-sectional diameter of NV to the blade diameter d. Similar to the results of the l and N changes described above, n increased lineally with the increase in U in all d. The relationship between U_{min} and d obtained from the experiments in Fig. 5-18(b) is shown in Fig. 5-19. U_{min} had a minimum at $d = 20$ and 25mm of $U_{min} \simeq 3$m/s and a maximum at $d = 28$ and 30mm of $U_{min} \simeq 6$m/s. U_{min} tended to increase in large diameters of $d = 28$ and 30mm but systematic change was not observed. As a result of the flow visualization experiments described in the Chapter 3, the size of NV formed at the intersection of the cylinder blade and the ring-plate (D_V) increased with increasing d at a constant $s/d = 0.35$, which was expected to increase T_{NV} acting on the stepped circular cylinder blade. However, at the same time, the formation of NV becomes unstable (SD) with increasing d, which may indicate that T_{NV} becomes unstable. In addition, T_{fric} to the rotational motion increases proportionally to the mass of the entire stepped circular cylinder blade, m, and T_{fric} increases with increasing d. From the above changes in T_{NV} and T_{fric}, it is considered that the minimum flow velocity U_{min}, which satisfies the condition $T_{NV} \geq T_{fric}/N$ for steady rotation, tended to increase with d. Fig. 5-20 shows the relationship between d and n at a constant flow velocity $U = 10$ and 12m/s in the un-load experiments. In order to evaluate the repeatability of the rotational speed for each d, the result for $s/d = 0.35$ in the relationship between n and s/d in Fig. 5-18(a) is also shown. The significant difference between the two results at $U = 12$m/s was not confirmed for each d, which indicates that the rotational speed at un-loaded has well repeatability for both d. n was maximum at $d = 30$mm and minimum at $d = 23$mm, but systematic change was not observed. At $N = 2$, the interference effect by the wake related to rotation did not occur on the stepped circular cylinder blades at all d, and the instability of NV formation was eliminated by increasing U and T_{NV} became stable. Therefore, for $U = 10$ and 12m/s, since T_{NV} and T_{drag} acting per stepped circular cylinder blade increased in proportion to the

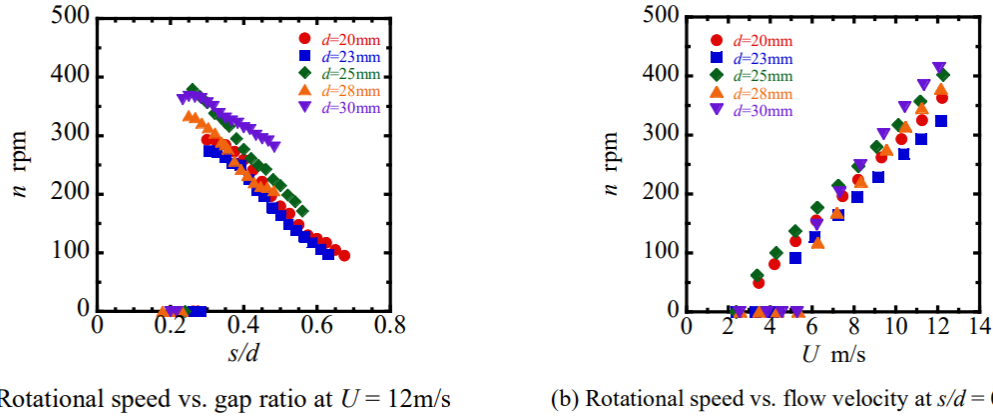increase in d, n tended to be nearly constant for all d.

(a) Rotational speed vs. gap ratio at $U = 12$m/s

(b) Rotational speed vs. flow velocity at $s/d = 0.35$

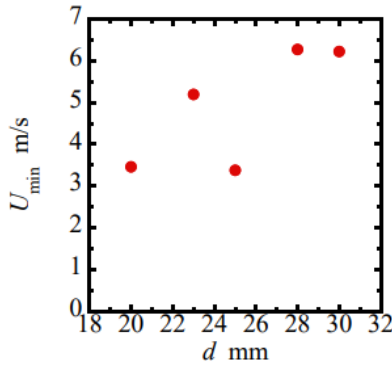Fig. 5-18 Results of un-loaded experiments each value of blade diameter. $d = 20\text{-}30$mm, $l = 60$mm, $N = 2$.

Fig. 5-19 Minimum flow velocity for rotation vs. blade diameter of stepped cylinder blade turbine through un-loaded experiment. d=20-30mm, l=60mm, N=2, s/d=0.35.
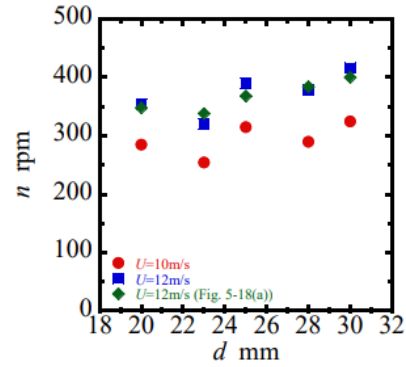
Fig. 5-20 Rotational speed vs. blade diameter of stepped cylinder blade turbine through un-loaded experiment at each U. d=20-30mm, l=60mm, N=2, s/d=0.35.

Figure 5-21 shows the relationship between n and T_{brake} of the stepped circular cylinder blade wind turbine with $l = 60$mm, $N = 2$, $d = 20\text{-}30$mm, and $U = 10$m/s. n increased with the decrease in T_{brake} for all d. The maximum load torque $[T_{brake}]_{max}$ at each d was maximum at $d = 25$mm and minimum at $d = 28$mm. The rotational speed when $[T_{brake}]_{max}$ is obtained (n_{min}) was less than $n_{min} < 50$ rpm for $d = 20$ and 25mm where $[T_{brake}]_{max}$ was higher, but the n_{min} for $d = 30$mm was about 5 times higher than that for $d = 20$ and 25mm.

$[T_{brake}]_{max}$, the rotational speeds n_{min} at $[T_{brake}]_{max}$, the rotational speed n_{max} at $T_{brake} = 0$, and λ_{ope} calculated by Eq. (5-1)-(5-3) are plotted against d in Figs. 5-22-5-25. As mentioned above, $[T_{brake}]_{max}$ was maximum at $d = 25$mm and minimum at $d = 28$mm, and the difference between these results was about 10 times. The systematic change in $[T_{brake}]_{max}$ was not confirmed with respect to the change in d. n_{min} tended to increase with increasing d except $d = 25$mm. This tendency means that the minimum rotational speed at which NV

is formed increases with increasing d. In order to compare the experimental results with the minimum rotational speed at which NV is steadily formed in the un-load condition, the rotational speed at U_{min} in Fig. 5-18(b) is also shown in Fig. 5-23. n was less than 50rpm at $d = 20$ and 25mm, and n_{min} and n at U_{min} for these were well agreed. That is, the NV is formed steadily at small n in both un-loaded and loaded condition at $d = 20$ and 25mm. On the other hand, at $d = 23$, 28, and 30mm, both n_{min} and n at U_{min} were larger than the results for $d = 20$ and 25mm, indicating that the minimum rotational speeds in which NV is formed steadily was larger in both the loaded and un-loaded conditions. Also, n_{min} was larger than n at U_{min} for these d.

  Assuming that T_{NV} increases proportionally with d at $s/d = 0.35$ and that the formation of NV is stable throughout the loaded experiments at all d and that T_{fric} is negligibly small compared to $[T_{brake}]_{max}$, $[T_{brake}]_{max}$ increases proportionally with the increasing d. In the actual loaded experiments, the decrease in n caused instability in the formation of NV at large d, and this instability of NV caused sudden stop of the steady rotation during the loaded experiments at $d = 23$, 28, and 30mm. However, the exact reason for the sudden stop of rotation at $d = 23$mm, while the continuous rotation was observed to the small speed below 50 rpm at $d = 25$mm, is unknown. The change in n_{max} was in good agreement with the relationship between d and n at un-loaded experiments in $U = 10$m/s shown in Fig. 5-20. λ_{ope} of each d was $\lambda_{ope} \simeq 0.2$ at $d = 20$ and 25mm and $\lambda_{ope} \simeq 0.07$ at other $d = 23$, 28 and 30mm.
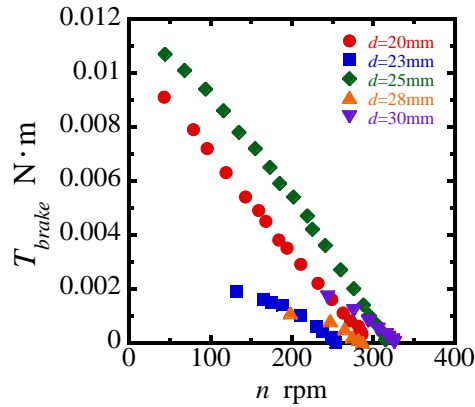

Fig. 5-21 Load torque vs. rotational speed at $U = 10$m/s for each value of blade diameter through loaded experiments. $d = 20$-30mm, $l = 60$mm, $N = 2$, $s/d = 0.35$.
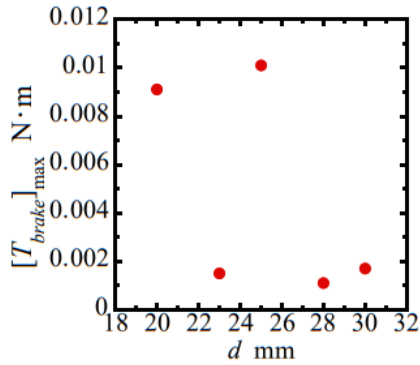
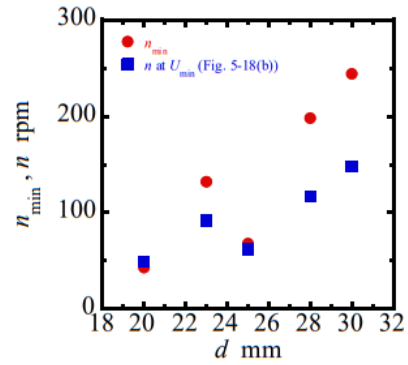Fig. 5-22 Maximum load torque vs. blade diameter through loaded experiment. d=20-30mm, l=60mm, N=2, s/d=0.35.

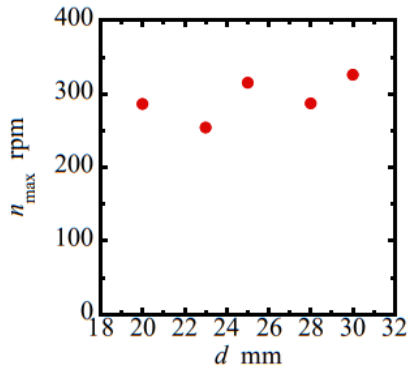Fig. 5-23 Rotational speeds vs. blade diameter through un-loaded and loaded experiment. d=20-30mm, l=60mm, N=2, s/d=0.35.

Fig. 5-24 Maximum rotational speed vs. blade diameter through loaded experiment. d=20-30mm, l=60mm, N=2, s/d=0.35.
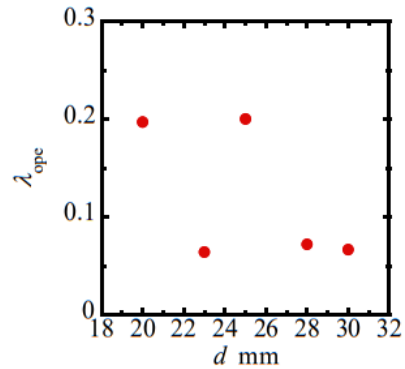

Fig. 5-25 Operating rotation range vs. blade diameter through loaded experiment. d=20-30mm, l=60mm, N=2, s/d=0.35.

Figure 5-26 shows the relationship between U and n in un-loaded experiments in each d at $N = 4$ and $l = 60$mm. Similar to the results of $N = 2$, n increased lineally with the increase in U in all d. The relationship between U_{min} and d is shown in Fig. 5-27. Similar to the results of $N = 2$, systematic change of U_{min} was not observed. Fig. 5-28 shows the relationship between d and n at $U = 10$m/s in the un-load experiments. n was maximum at $d = 30$mm and minimum at $d = 20$mm, but systematic change was not observed, and the rotational speed increased between 300-400rpm in all d ranges. The interference effect by the wake related to rotation did not occur at all d in $N = 4$ and the instability of NV formation was eliminated by increasing U, and T_{NV} became stable. Therefore, since T_{NV}, T_{drag}, and T_{drag} acting per stepped circular cylinder blade increased in proportion to the increase in d at $U = 10$m/s, n tended to be nearly constant for all d.
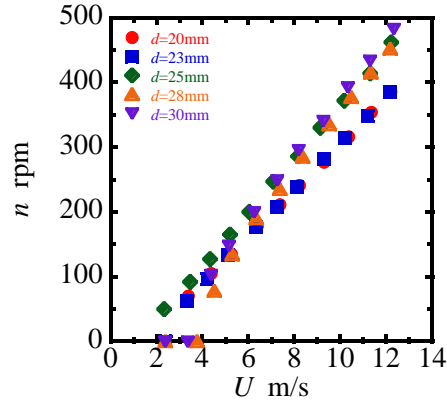
82

Fig. 5-26 Rotational speed vs. flow velocity at each value of blade diameter through un-loaded experiments. d = 20-30mm, l = 60mm, N = 4, s/d = 0.35.
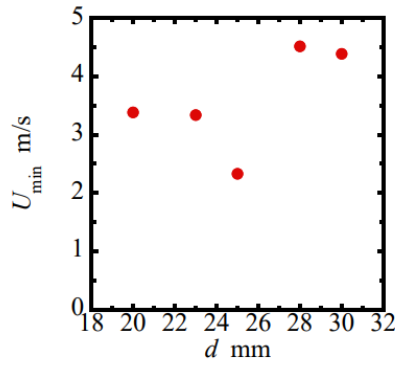

Fig. 5-27 Minimum flow velocity for rotation vs. blade diameter of stepped cylinder blade turbine through un-loaded experiment. d=20-30mm, l=60mm, N=4, s/d=0.35.
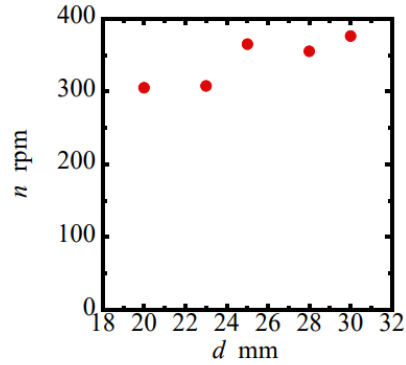

Fig. 5-28 Rotational speed at U=10m/s vs. blade diameter of stepped cylinder blade turbine through un-loaded experiment. d=20-30mm, l=60mm, N=4, s/d=0.35.

Figure 5-29 shows the relationship between n and T_{brake} of the stepped circular cylinder blade wind turbine with l = 60mm, N = 4, d = 20-30mm, and U = 10m/s. n increased with the decrease of T_{brake} for all d. The maximum load torque $[T_{brake}]_{max}$ at each d was maximum at d = 25mm and minimum at d = 30mm. The rotational speed when $[T_{brake}]_{max}$ is obtained n_{min} was less than $n_{min} < 50$ rpm for d = 20 and 25mm, where $[T_{brake}]_{max}$ was higher, but the n_{min} for d = 30mm was about 6-10 times higher than that for d = 20 and 25mm. $[T_{brake}]_{max}$, the rotational speeds n_{min} at $[T_{brake}]_{max}$, the rotational speed n_{max} at T_{brake} = 0, and λ_{ope} calculated by Eq. (5-1)-(5-3) are plotted against d in Figs. 5-30-5-33. $[T_{brake}]_{max}$ was maximum at d = 25mm and minimum at d = 30mm, and the systematic change in $[T_{brake}]_{max}$ was not confirmed with respect to the change in d. The systematic change in n_{min} was also not confirmed with respect to the increasing of d as shown in Fig. 5-31. Comparing these n_{min} with n at U_{min} in the un-loaded condition shown in Fig. 5-26, n_{min} were larger about 100rpm than n at U_{min} at d = 23, 28, and 30mm.

In the condition of $N = 4$, as same as $N = 2$, it is considered that the decrease in n caused the instability of formation of NV under large d conditions, and this instability of NV caused the sudden stop of the steady rotation during the loaded experiments at $d = 23$, 28, and 30mm. The change in n_{max} shown in Fig. 5-32 was in good agreement with the relationship between d and n at un-loaded experiments in $U = 10$m/s shown in Fig. 5-28. λ_{ope} of each d was $\lambda_{ope} > 0.2$ at $d = 20$ and 25mm and $\lambda_{ope} \simeq 0.1$ at other $d = 23$, 28 and 30mm, and the value of λ_{ope} was larger for all d compared to the case of $N = 2$.
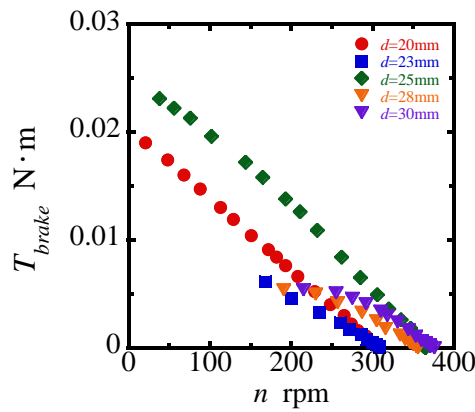

Fig. 5-29 Load torque vs. rotational speed at $U = 10$m/s for each value of blade diameter through loaded experiments. $d = 20$-30mm, $l = 60$mm, $N = 4$, $s/d = 0.35$.

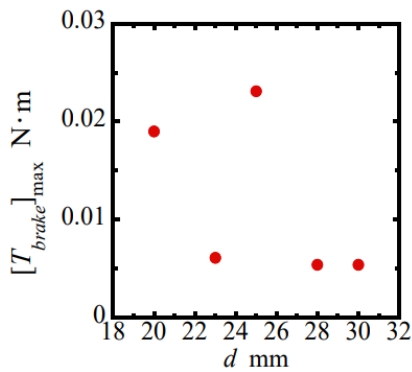Fig. 5-30 Maximum load torque vs. blade diameter through loaded experiment. d=20-30mm, l=60mm, N=4, s/d=0.35.
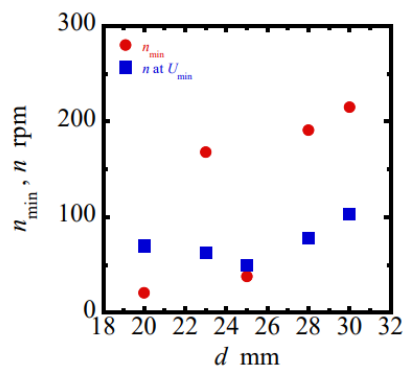
Fig. 5-31 Rotational speeds at $[T_{brake}]_{max}$ vs. blade diameter through un-loaded and loaded experiment. d=20-30mm, l=60mm, N=4, s/d=0.35.

84
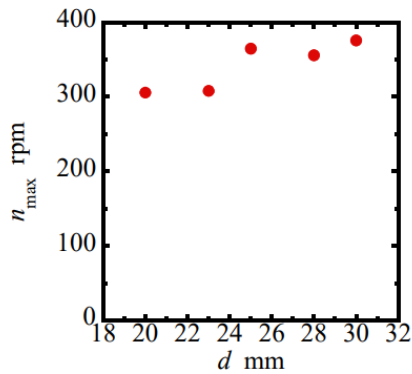
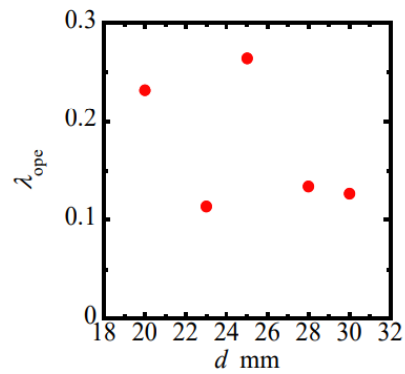Fig. 5-32 Maximum rotational speed vs. blade diameter through loaded experiment. d=20-30mm, l=60mm, N=4, s/d=0.35.

Fig. 5-33 Operating rotation range vs. blade diameter through loaded experiment. d=20-30mm, l=60mm, N=4, s/d=0.35.

Figure 5-34 shows the relationship between U and n in un-loaded experiments in each d at N = 8 and l = 60mm. n increased linearly with the increase in U in all d. The relationship between U_{min} and d is shown in Fig. 5-35. It was $U_{min} \simeq$ 2m/s in all d. This indicates that the rotation started at the lower flow velocity than the minimum wind speed of the wind tunnel, and exact minimum velocity for the start of rotation was obtained. For N = 2 and 4, the minimum velocity U_{min}, which satisfies the condition $T_{NV} \geq T_{fric}/N$ for steady rotation, tended to increase with d due to the instability of NV in small U and large d. At N = 8, U_{min} was almost constant for all d, indicating that T_{NV} and T_{fric} increased in proportion to the increase in d. As the pitch between stepped circular cylinder blades decreased with the increase of N, only the region for the formation of NV and suction flow occurred in the spacing between two blades, as shown in the visualization in Chapter 3 (Fig. 3-3(b)). As a result, the formation of NVs is considered to be stable at low flow velocities for N = 8. Fig. 5-36 shows the relationship between d and n at a constant flow velocity U = 10m/s. The rotational speed shifted in the range of 340-400 rpm for all d. This means that T_{NV} and T_{drag} acting per stepped circular cylinder blade, as well as T_{fric}, increased in proportion to the increase in d.
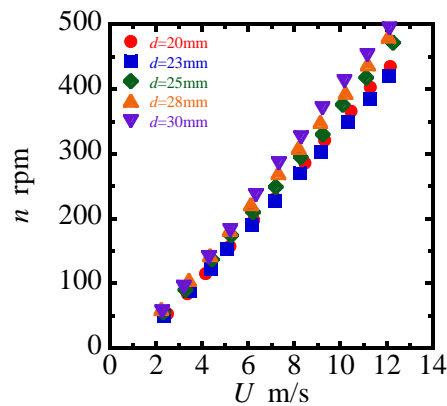

Fig. 5-34 Rotational speed vs. flow velocity at each value of blade diameter through un-loaded experiments. d = 20-30mm, l = 60mm, N = 8, s/d = 0.35.
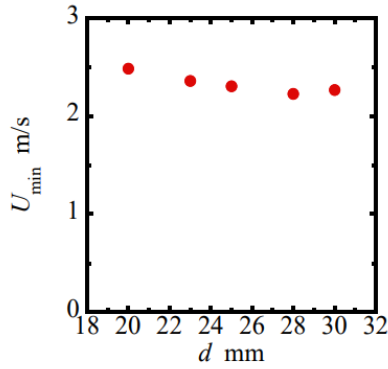
Fig. 5-35 Minimum flow velocity for rotation vs. blade diameter of stepped cylinder blade turbine through un-loaded experiment. d=20-30mm, l=60mm, N=8, s/d=0.35.

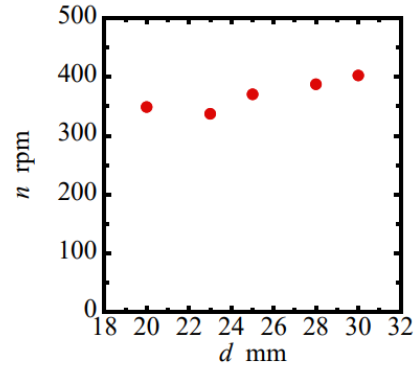

Fig. 5-36 Rotational speed at U=10m/s vs. blade diameter of stepped cylinder blade turbine through un-loaded experiment. d=20-30mm, l=60mm, N=8, s/d=0.35.

Figure 5-37 shows the relationship between n and T_{brake} of a stepped circular cylinder blade wind turbine with l = 60mm, N = 8, d = 20-30mm, and U = 10m/s. n increased with the decrease of T_{brake} for all d. The maximum load torque $[T_{brake}]_{max}$ at each d was maximum at d = 25mm and minimum at d = 20mm. The rotational speed n_{min} when $[T_{brake}]_{max}$ is obtained was close to zero for all d. $[T_{brake}]_{max}$, the rotational speeds n_{min} at $[T_{brake}]_{max}$, the rotational speed n_{max} at T_{brake} = 0, and λ_{ope} calculated by Eq. (5-1)-(5-3) are plotted against d in Figs. 5-38-5-41. As shown in Fig. 5-38, $[T_{brake}]_{max}$ increased in the range of $20 \leq d \leq 25$mm and decreased in the range of $25 \leq d \leq 30$mm. n_{min} shown in Fig. 5-39 remained constant around 15rpm in the range of $20 \leq d \leq 28$mm but increased rapidly to around 40rpm at d = 30mm. These n_{min} are compared with n at U_{min} in the un-loaded experiments shown in Fig. 5-34. n_{min} was less than n at U_{min} for all d, although it was suggested that the stepped circular cylinder blade rotates at the smaller flow velocity than that of the wind tunnel specification of U = 2m/s and exact n at U_{min} was not obtained. These values of n_{min} and n at U_{min} showed that the minimum rotational speed for the steady formation of NV was decreased by the multiple-blade design.

In the visualization of NV at d = 28mm and N = 8 shown in Chapter 3, the formations of NV from the cylinder blade forward of the rotational direction and the suction flow toward the rear cylinder blade were observed to occur side by side. The interference between NV formation and suction flow was not observed in the visualization. However, the formation of NV and suction flow occurred in a narrower range, which may have reduced the lift force although the NV is formed steadily. It is considered that $[T_{brake}]_{max}$ decreased at large d as the results. The change in n_{max} was in good agreement with the relationship between d and n at un-loaded condition in U = 10m/s shown in Fig. 5-36. λ_{ope} of each d was $\lambda_{ope} \simeq$ 0.25-0.3 for all d. The results show that the operating range of the stepped circular cylinder blade wind turbine with N = 8 is unaffected by the interference effects that would occur at d = 28 and 30mm.
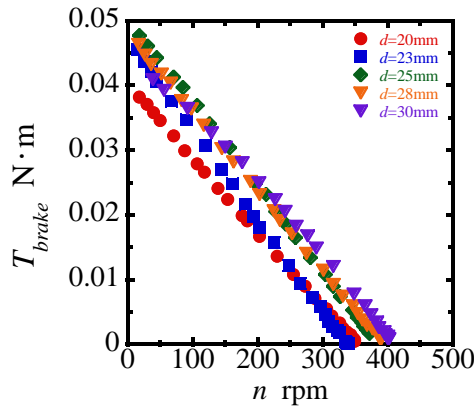
Fig. 5-37 Load torque vs. rotational speed at $U = 10$m/s for each value of blade diameter through loaded experiments. $d = 20$-30mm, $l = 60$mm, $N = 8$, $s/d = 0.35$.
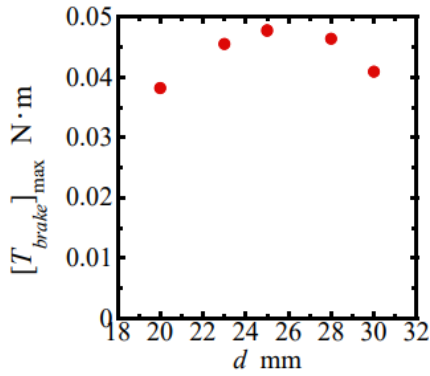

Fig. 5-38 Maximum load torque vs. blade diameter through loaded experiment. d=20-30mm, l=60mm, N=8, s/d=0.35.
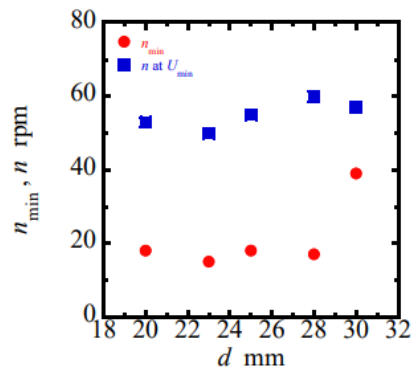

Fig. 5-39 Rotational speeds vs. blade diameter through un-loaded and loaded experiment. d=20-30mm, l=60mm, N=8, s/d=0.35.

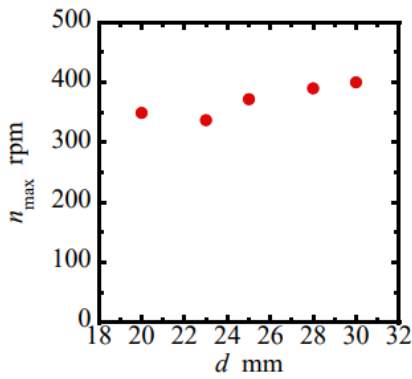Fig. 5-40 Maximum rotational speed vs. blade diameter through loaded experiment. d=20-30mm, l=60mm, N=8, s/d=0.35.
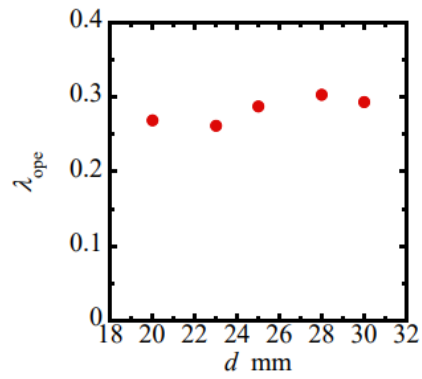

Fig. 5-41 Operating rotation range vs. blade diameter through loaded experiment. d=20-30mm, l=60mm, N=8, s/d=0.35.

Figure 5-42 shows the relationship between U and n in un-loaded experiments in each d at $N = 10$ and $l = 60$mm. n increased lineally with the increase in U at $d = 20, 23, 25$mm, and rapidly increased in the range of $U \geq 9$m/s at $d = 28, 30$mm. The relationship between U_{min} and d is shown in Fig. 5-43. It was $U_{min} \simeq 2$m/s in all d and this indicates that the rotation started at the lower flow velocity than the minimum flow velocity of the wind tunnel. Fig. 5-44 shows the relationship between d and n at $U = 10$m/s. n was almost constant around $370 \leq n \leq 390$rpm at $d = 20, 23, 25$mm, and around $n = 470$rpm at $d = 28, 30$mm. These results suggest that some effects of high rotation on the stepped circular cylinder blades occurs at high flow velocity of $d = 28$ and 30mm in addition to the interference effect by the wake for the rotational motion, and the drag coefficient of fluid resistance for rotation C_D, which determines the fluid resistance torque T_{drag} (see Eq. (4-3)).
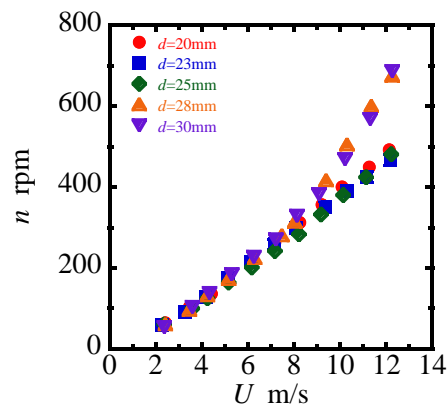
Fig. 5-42 Rotational speed vs. flow velocity at each value of blade diameter through un-loaded experiments. $d = 20\text{-}30$mm, $l = 60$mm, $N = 10$, $s/d = 0.35$.
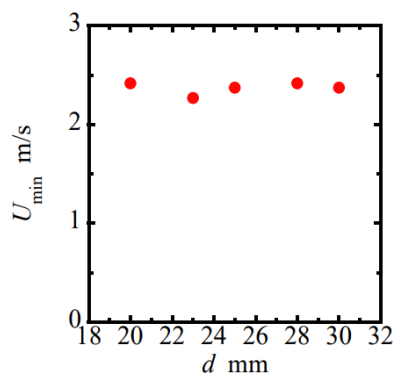
Fig. 5-43 Minimum flow velocity for rotation vs. blade diameter of stepped cylinder blade turbine through un-loaded experiment. d=20-30mm, l=60mm, N=10, s/d=0.35.
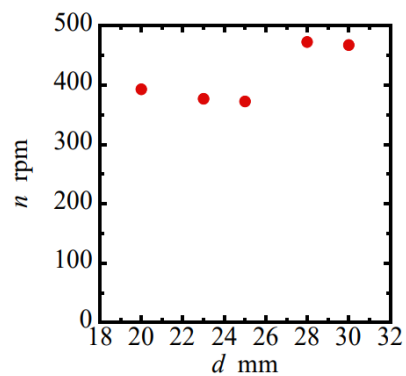
Fig. 5-44 Rotational speed at U=10m/s vs. blade diameter of stepped cylinder blade turbine through un-loaded experiment. d=20-30mm, l=60mm, N=10, s/d=0.35.

Figure 5-45 shows the relationship between n and T_{brake} of the stepped circular cylinder blade wind turbine with $l = 60$mm, $N = 10$, $d = 20$-30mm, and $U = 10$m/s. n increased linearly with the decrease of T_{brake} over the entire measurement range of n for $d = 20$, 23, 25mm, but the gradient of T_{brake} of $d = 28$ and 30mm differed between n_{max}-350rpm and 350rpm-n_{min}. The rotational speed at which the gradient changes $n \simeq$ 350rpm coincided with n just before that the sudden increase occurred at $d = 28$ and 30 mm in the relationship between U and n shown in Fig. 5-42. The maximum load torque $[T_{brake}]_{max}$ was maximum at $d = 28$mm and minimum at $d = 30$mm. The systematic change in n_{min}, in which $[T_{brake}]_{max}$ is obtained, was not observed. $[T_{brake}]_{max}$, n_{min}, n_{max}, and λ_{ope} are plotted against d in Figs. 5-46-5-49. As shown in Fig. 5-46, $[T_{brake}]_{max}$ was maximum at $d = 28$mm and minimum at $d = 30$mm, but the systematic change with the increase in d was not confirmed. n_{min} shown in Fig. 5-47 also did not show the systematic change with the increase in d. These n_{min} are compared with n at U_{min} in the un-loaded experiments shown in Fig. 5-42. n_{min} was about 70rpm higher at $d = 30$mm, but n_{min} was equal to or lower than n at U_{min} other d. These comparisons suggest that the formation of NVs is stable at small U at $N = 10$, although the interference effect by the wake for the rotational motion occurs for all d. Some effect of high rotation of the cylinder blade and the interference effect may cause the decrease of T_{NV} in the high flow velocity range from around $U \geq 9$m/s at $d = 28$ and 30mm, and in the high rotational speed range above $n = 350$rpm. The change in n_{max} was in good agreement with the relationship between d and n at un-loaded experiments in $U = 10$m/s shown in Fig. 5-44. λ_{ope} shown in Fig. 5-49 corresponded well to the increase or decrease in $[T_{brake}]_{max}$ for d shown in Fig. 5-46.

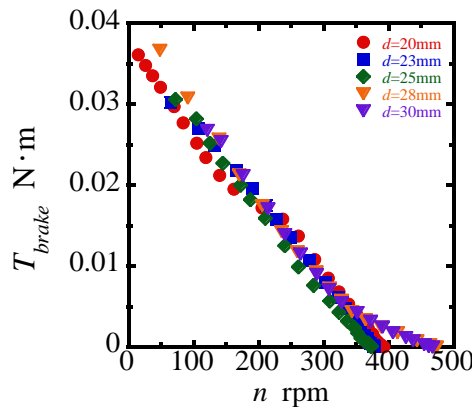Fig. 5-45 Load torque vs. rotational speed at $U = 10$m/s for each value of blade diameter through loaded experiments. $d = 20$-30mm, $l = 60$mm, $N = 10$, $s/d = 0.35$.
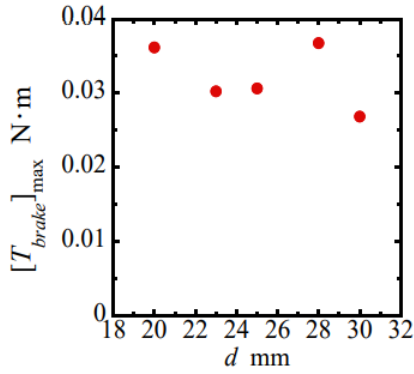
Fig. 5-46 Maximum load torque vs. blade diameter through loaded experiment. d=20-30mm, l=60mm, N=10, s/d=0.35.
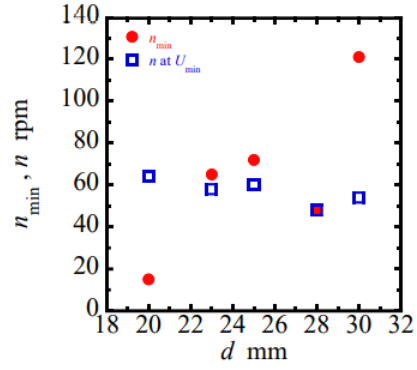
Fig. 5-47 Rotational speeds at $[T_{brake}]_{max}$ vs. blade diameter through un-loaded and loaded experiment. d=20-30mm, l=60mm, N=10, s/d=0.35.
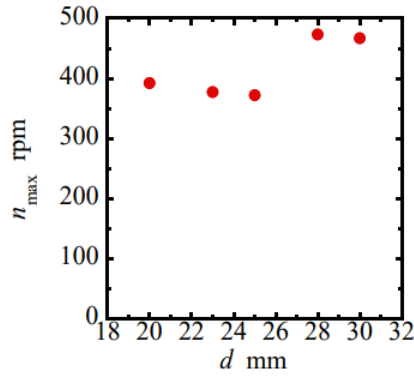
Fig. 5-48 Maximum rotational speed vs. blade diameter through loaded experiment. d=20-30mm, l=60mm, N=10, s/d=0.35.
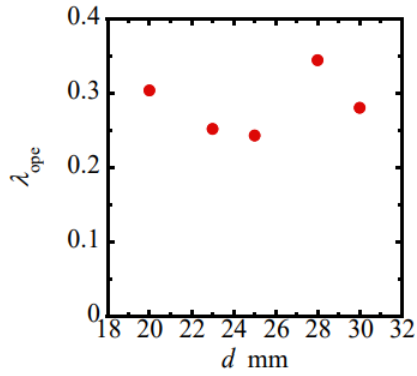
Fig. 5-49 Operating rotation range vs. blade diameter through loaded experiment. d=20-30mm, l=60mm, N=10, s/d=0.35.

5.1.4 Influence of pitch ratio of cylinder blades

The effect of the pitch ratio t/d, which was determined by dividing the pitch t between adjacent cylinder blades on the ring-plate diameter by the cylinder blade diameter d shown in Fig. 5-50, on the rotation and output torque characteristics was investigated. The experimental results for varying d at each N shown in the previous section are converted into a change in t/d. The pitch t between adjacent cylinder blades on the ring-plate diameter is defined as Eq. (5-4). That is, a large blade number N and blade diameter d make t/d smaller.

$$t = \frac{D\pi - Nd}{N} \qquad (5-4)$$

Figure 5-51 shows the relationship between t/d and n under un-load experiments at U = 10m/s. n increased gradually with the decrease in t/d in a wide range of $t/d \geq 1.5$, although there is some variation across the

90

entire range. n increased rapidly within the narrow range of $t/d < 1.5$. These results show that the interference effect due to the wake of the rotational motion of the stepped circular cylinder blade and the effect of high rotation occur in the region of $t/d < 1.5$.

Figire 5-52 shows the relationship between $[T_{brake}]_{max}$ and n_{min} with respect to t/d at $U = 10m/s$. The systematic change in $[T_{brake}]_{max}$ for t/d was not observed in the range of $t/d \geq 2.5$ where $N = 2$ and 4. On the other hand, in the range of $t/d \leq 2.5$, $[T_{brake}]_{max}$ increased with the decrease in t/d, reached a maximum around $t/d = 1.5$ and then decreased sharply, with unsystematic effect of t/d on n_{min}. The variation of n_{min} and $[T_{brake}]_{max}$ in the range of $t/d \geq 2.5$ is considered to be attributed to the instability of T_{NV} values due to the occurrence of instability of NV formation. In a very narrow range of $1.5 \leq t/d \leq 2.5$, the lift force by the NV acting on each stepped circular cylinder blade was stable, but in $1.5 \leq t/d$, the lift force reduced by the interference effect.

The effects of the conditions of t/d, flow velocity and rotational speed on the experimental results are summarized as below. In the un-loaded experiments, the formation of NV is unstable at small flow velocities and small notational speeds in many t/d, and the lift force by the NV is also unstable. This causes the variation of U_{min}. In the range of $t/d \leq 1.5$, the effect of the interference effect due to the wake of the rotational motion of the cylinder blade and the effect of high rotation cause the decrease of drag coefficient for rotating direction C_D. This decrease in C_D reduces the fluid resistance torque T_{drag}, and the rotational speed increases rapidly based on the equilibrium of the torques in Section 4.5. In the loaded experiments at $U = 10m/s$, the formation of NV becomes unstable with decreasing rotational speed by the increasing of the load at $t/d \geq 2.5$, and the rotation may stop suddenly. Due to this phenomenon, $[T_{brake}]_{max}$ does not change systematically. $[T_{brake}]_{max}$ decreases rapidly at $t/d \geq 1.5$ due to the effect of interference and the decrease in lift force, although the rotational speed is small, and the formation of NV is stable.
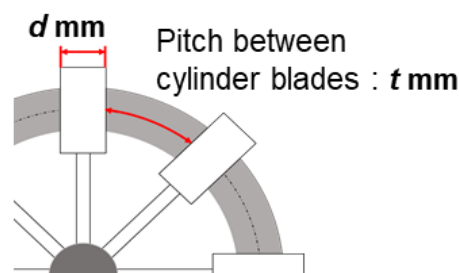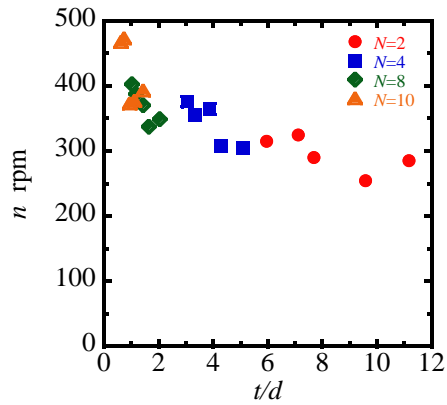

Fig. 5-50 schematic diagram of definition of pitch ratio t/d.

Fig. 5-51 Rotational speed vs. pitch ratio at $U = 10$m/s categorized by blade number ($W = 20$mm, $s/d = 0.35$, $l = 60$mm).

(a) $[T_{brake}]_{max}$ vs. pitch ratio

(b) n_{min} vs. pitch ratio
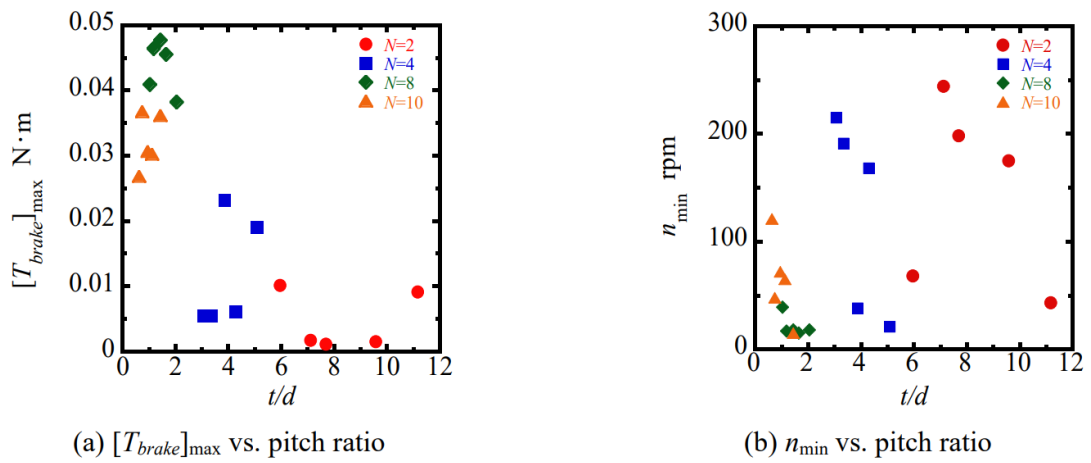
Fig. 5-52 Effect of pitch ratio on results of loaded experiments at $U = 10$m/s ($W = 20$mm, $s/d = 0.35$, $l = 60$mm).

5.2 Evaluation of the lift coefficient

The maximum driving torque (static torque) $[T_{NV}]_{max}$ by the NV and the lift coefficient C_{la} (see Fig. (4-8)) acting per stepped circular cylinder blade are obtained by approximating the results of loaded experiments as a linear function for each l, N and d. In the actual loaded experiments, the instability of the formation of NV with the decrease in the rotational speed caused the suddenly stop of the steady rotation without reaching n close to zero. But in this section, it is assumed that NV forms steadily even at small rotational speed under all conditions, and $[T_{NV}]_{max}$ and C_{la} are calculated assuming that the relationship between n and T_{brake} is completely linear. The equilibrium of the torques acting in the rotational direction of the stepped circular cylinder blade is expressed as follows Ep. (5-5), in the loaded experiments in which the load torque is applied to the driving shaft of the wind turbine by electromagnetic brakes.

$$T_{NV} = T_{drag} + \frac{T_{fric}}{N} + \frac{T_{brake}}{N} \qquad (5-5)$$

The relationship between n and T_{brake}, which was obtained by loaded experiments at $U = 10$m/s, was almost linear in most cases. This relationship is approximated by a linear function, and the T_{brake} at $n = 0$ ($[T_{brake}]_{n=0}$) is obtained by extrapolation. Since T_{drag} is zero at $n = 0$, the following relationship for T_{NV} is obtained.

$$[T_{NV}]_{max} = \frac{T_{fric}}{N} + \frac{[T_{brake}]_{n=0}}{N} \qquad (5-6)$$

T_{fric} in each condition is given by Eq. (5-7).

$$T_{fric} = \mu m r_{shaft} = \mu(m_{shaft} + N m_{blade}) r_{shaft} \qquad (5-7)$$

Where μ (= 0.002) is the coefficient of friction, m_{shaft} is the weight of the driving shaft and hub, m_{blade} is the weight of a stepped circular cylinder blade, and r_{shaft} is the radius of the driving shaft. The maximum driving torque $[T_{NV}]_{max}$ at $n = 0$ is calculated by using the value of $[T_{brake}]_{n=0}$ obtained by the above procedure and equations. The lift coefficient C_{la} is calculated by substituting $[T_{NV}]_{max}$ into Eq. (5-8).

$$[T_{NV}]_{max} = \frac{1}{2} C_{la} \rho d l_{NV} U^2 r_{NV} \qquad (5-8)$$

Where l_{NV} is the spanwise length of the forming region and r_{NV} is the distance of the point of application of the NV from the driving shaft.

5.2.1 Effective length ratio l/d

Figure 5-53 shows the changes in $[T_{NV}]_{max}$ and C_{la} with respect to the effective length ratio l/d of the stepped circular cylinder blade with $N = 2$ and $d = 20$mm. Since the optimum length of the forming region was determined to $l = l_{NV} = 60$mm ($l/d = 3$), l_{NV} is set to l at $l/d = 2$, 2.5 ($l = 40$, 50mm) and 60mm at $l/d = 3$-4.5 ($l = 60$-90mm). $[T_{NV}]_{max}$ and C_{la} reached maximum at $l/d = 3$ and $l/d = 2.5$, respectively. Since there is no significant difference between these l/d which $[T_{NV}]_{max}$ and C_{la} reach the maximum, the NV is formed in the range of $l/d = 2.5$-3, and the lift force of NV is efficiently obtained.

(a) $[T_{NV}]_{max}$ vs. l/d

(b) C_{la} vs. l/d
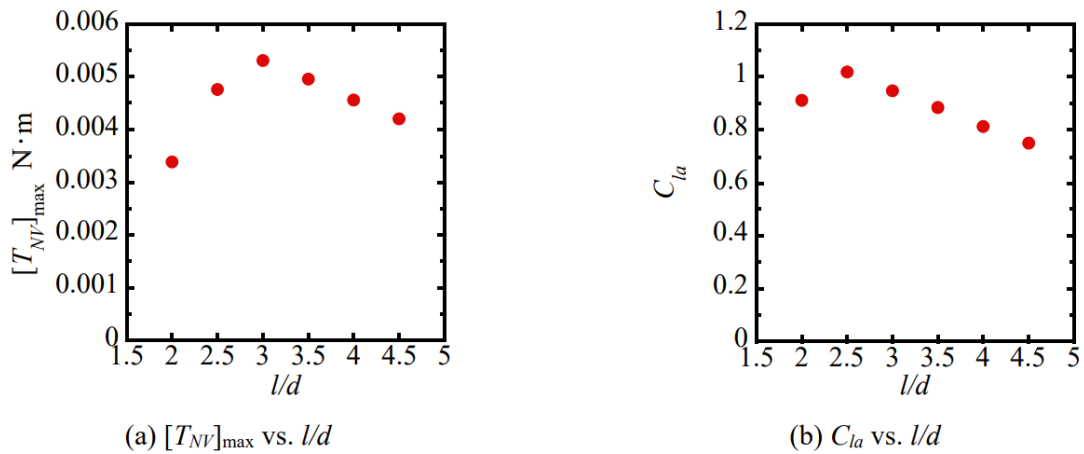
Fig. 5-53 Calculation results of maximum driving torque and lift force coefficient in each effective length ratio of stepped circular cylinder blade at $N = 2$, $d = 20$mm, $W = 20$mm.

5.2.2 Blade number N

Figure 5-54 shows the changes of $[T_{NV}]_{max}$ and C_{la} with the blade number for the stepped circular cylinder blade with $l/d = 3$ and $d = 20$mm. Both $[T_{NV}]_{max}$ and C_{la} were almost constant in the range of $2 \leq N \leq 8$, which means that the interference effect by the wake due to the rotational motion of the cylinder blade did not occur, and that the lift force by the NV increased in proportion to the increase in N. The decrease in $[T_{NV}]_{max}$ and C_{la} at $N = 10$ and 12 shows that the interference effect occurred.

(a) $[T_{NV}]_{max}$ vs. N

(b) C_{la} vs. N

Fig. 5-54 Calculation results of maximum driving torque and lift force coefficient in each blade number at $l/d = 3$ ($l = 60$mm), $d = 20$mm, $W = 20$mm.

5.2.3 Effective diameter d

The changes of $[T_{NV}]_{max}$ and C_{la} with respect to the effective blade diameter d of the stepped circular cylinder blade with $l = 60$mm and $N = 2$ are shown in Fig. 5-55. Both $[T_{NV}]_{max}$ and C_{la} varied with the increase of d. At $N = 2$, the pitch between the adjacent stepped circular cylinder blades is sufficiently large at all d. Therefore, the interference effect does not occur, and $[T_{NV}]_{max}$ acting on per stepped circular cylinder blade is expected to increase proportionally to d, and C_{la} is expected to be constant. Also, since the gradient of the relationship between n and T_{brake} at $d = 20$ and 25mm is almost constant as shown in Fig. 5-21, it can be assumed that at $d = 23$, 28, and 30mm, T_{brake} changes along the same gradient as at $d = 20$ and 25 mm if the NV is stable up to around $n = 0$ during the loaded experiments. Fig. 5-55 shows $[T_{NV}]_{max}$ and C_{la} calculated under the above assumption that the relationship between n and the T_{brake} at $d = 23$, 28 and 30mm changes at the same gradient as $d = 20$mm. $[T_{NV}]_{max}$ increased with increasing d and the range of variability of C_{la} narrowed compared to before the modification.
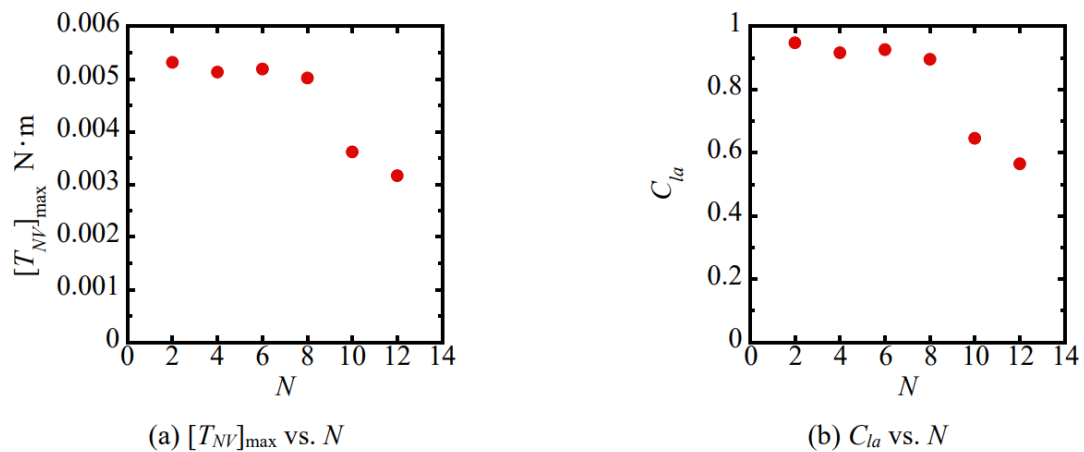

(a) $[T_{NV}]_{max}$ vs. d (b) C_{la} vs. d

Fig. 5-55 Calculation results of maximum driving torque and lift force coefficient in each blade diameter at $l = 60$mm, $N = 2$, $W = 20$mm.

The changes of $[T_{NV}]_{max}$ and C_{la} with respect to d of the stepped circular cylinder blade with $N = 4$ are shown in Fig. 5-56. The modified $[T_{NV}]_{max}$ and C_{la} for $d = 23$, 28, and 30mm, assuming that the relationship between n and T_{brake} varies with the same gradient as $d = 20$mm are also shown. As same as $N = 2$, it is expected that $[T_{NV}]_{max}$ acting on per stepped circular cylinder blade increased proportionally to d and C_{la} was constant, if the NV forms stably up to around $n = 0$ during the loaded experiments. The modified $[T_{NV}]_{max}$ increased with increasing d and the range of variability of modified C_{la} narrowed compared to before the modification.

(a) $[T_{NV}]_{max}$ vs. d (b) C_{la} vs. d

Fig. 5-56 Calculation results of maximum driving torque and lift force coefficient in each blade diameter at l = 60mm, N = 4, W = 20mm.

The changes of $[T_{NV}]_{max}$ and C_{la} with respect to d of the stepped circular cylinder blade with N = 8 are shown in Fig. 5-57. In the loaded experiments shown in Fig. 5-37, steady rotation continued up to n = 0 for all d. It is considered that the NV was stable over the entire measurement range of n. $[T_{NV}]_{max}$ acting on per stepped circular cylinder blade increased linearly with increasing d in the range $20 \leq d \leq 25$mm, while it decreased in the range of $25 \leq d \leq 30$mm. Since the lift force by the NV usually increases with the increase of d, this decreases in $[T_{NV}]_{max}$ mean that the interference effect due to the wake on the rotational motion had occurred. The occurrence of this interference effect reduced C_{la}, which was constant in the range $20 \leq d \leq 25$mm.

(a) $[T_{NV}]_{max}$ vs. d (b) C_{la} vs. d
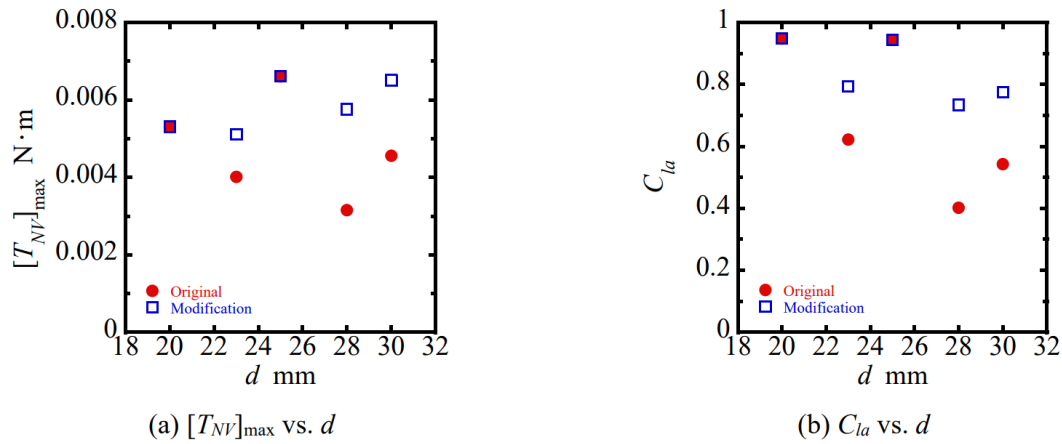
Fig. 5-57 Calculation results of maximum driving torque and lift force coefficient in each blade diameter at l = 60mm, N = 8, W = 20mm.

The changes of $[T_{NV}]_{max}$ and C_{la} with respect to d of the stepped circular cylinder blade with N = 10 are shown in Fig. 5-58. Both $[T_{NV}]_{max}$ and C_{la} decreased with increasing d. This phenomenon means that the

interference effect was increased by the decrease in the pitch between the stepped circular cylinder blades as d increases. The gradient of T_{brake} change differed between n_{min}-350rpm and 350rpm-n_{max} at $d = 28$ and 30mm in the loaded experiments shown in Fig. 5-45. In the former range (n_{min}-350rpm), only the interference effect by the wake for the rotational motion occurred in small pitch between cylinder blades, while in the later range (350rpm-n_{max}), the effect of high rotation of the cylinder blades may have occurred in addition to the interference effect. Therefore, modified $[T_{NV}]_{max}$ and C_{la} were calculated by using the relationships between n and T_{brake} in each rotational speed range. The results are shown in together as Large n (350rpm-n_{max}) and Small n (n_{min}-350rpm) in Fig. 5-58. The results of Large n show that $[T_{NV}]_{max}$ and C_{la} decrease significantly if the effect of high rotation could occur up to around $n = 0$. The results for Small n show that if the effect of high rotation does not occur but only interference effects occur, $[T_{NV}]_{max}$ is almost constant for d and C_{la} decreases slightly.
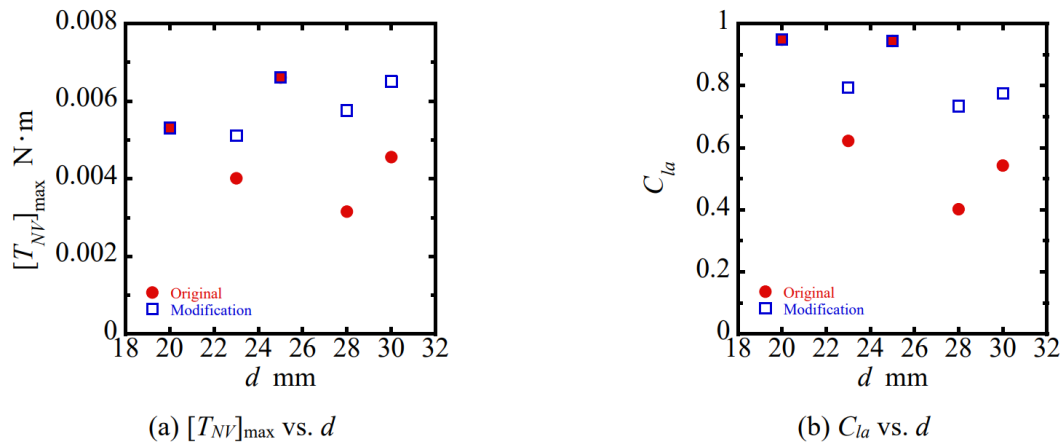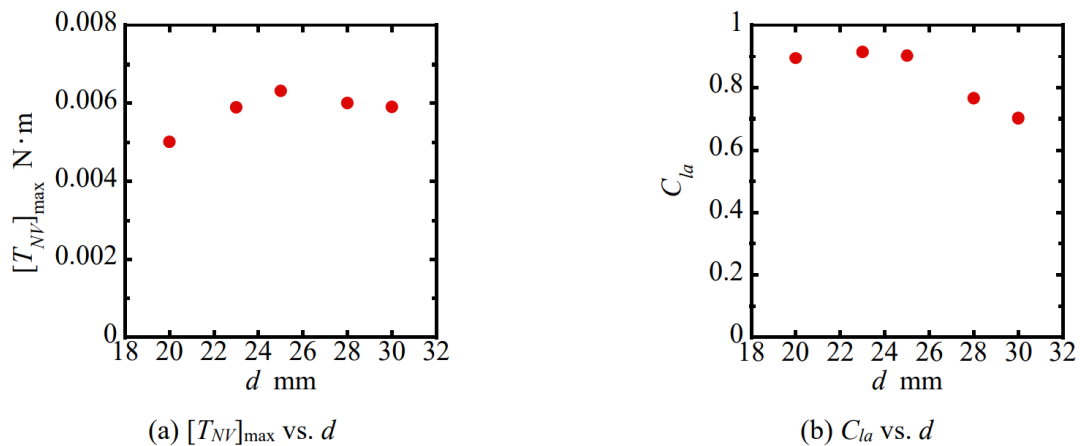

Fig. 5-58 Calculation results of maximum driving torque and lift force coefficient in each blade diameter at $l = 60$mm, $N = 10$, $W = 20$mm.

5.2.4   Pitch ratio t/d

Using the relationship between d and $[T_{NV}]_{max}$ and C_{la} for each N in the previous subsection, $[T_{NV}]_{max}$ and C_{la} for the pitch ratio t/d of the stepped circular cylinder blade are organized. The results for $d = 23$, 28, 30mm at $N = 2$ and 4 are based on the modified gradient of the $n \sim T_{brake}$ relationship. The results are shown in Fig. 5-59. The systematic change in $[T_{NV}]_{max}$ for the decrease in t/d was not observed. As shown in Section 5.2.2, when the stepped circular cylinder blades maintain the sufficient pitch that does not cause the wake interference effects on the rotational motion, $[T_{NV}]_{max}$ remains constant with increasing N for the certain d. Therefore, it is shown that the instability of NV formation by the increase in d had the significant effect on the variability of $[T_{NV}]_{max}$. C_{la} varied in the range of $t/d > 2$ but decreased continuously with the decrease in t/d in the range of $t/d < 2$. In the range of $t/d < 2$, the lift force by NV acting on the stepped circular cylinder

blade decreased by the interference effect by the wake for the rotational motion. As shown in Fig. 3-3(c) in Chapter 3, when t/d is small, the formation of NV and suction flow occurred next to each other in the narrow pitch between the two blades. It is shown that the NV was formed more stably in the range of $t/d < 2$ than in the case of $t/d > 2$ by above phenomenon, by the continuously reduce of C_{la}.

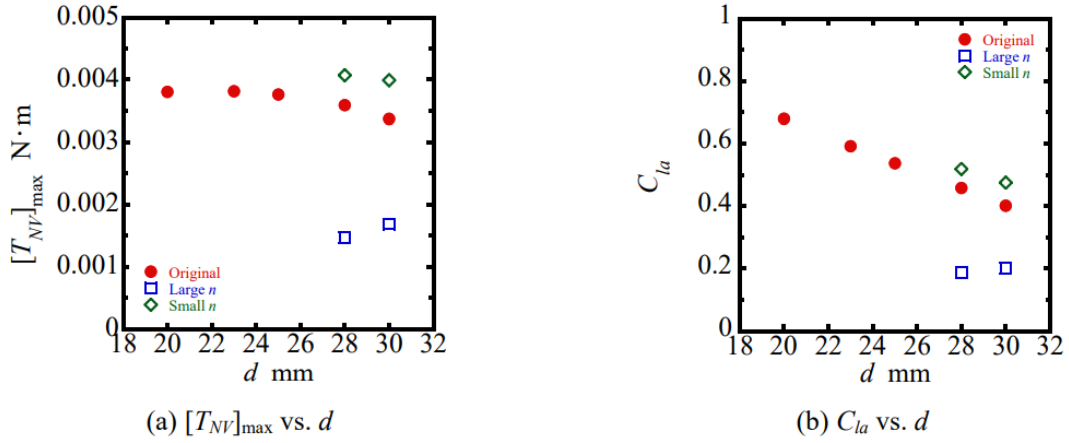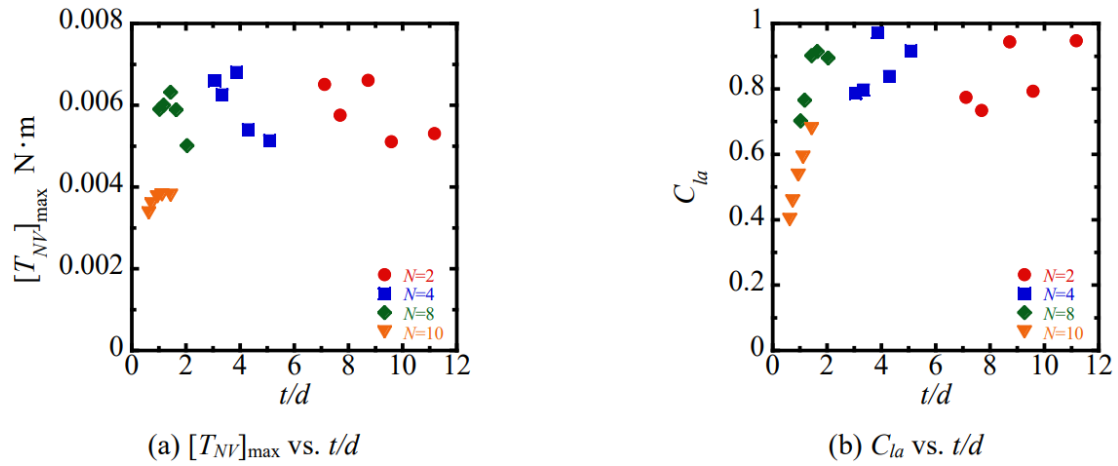(a) $[T_{NV}]_{max}$ vs. t/d (b) C_{la} vs. t/d

Fig. 5-59 Calculation results of maximum driving torque and lift force coefficient in each blade diameter at $l = 60$mm, $N = 2$-10, $W = 20$mm.

5.3 Effect of blade configuration on wind turbine performance

In order to evaluate the performance of the stepped circular cylinder blade wind turbine, the power coefficient C_p is obtained by using the results of the loaded experiments under each condition. The power coefficient C_p is defined by the following equation.

$$C_p = \frac{\omega T_{brake}}{0.5 \rho A U^3} \qquad (5-9)$$

Where ω (= $2\pi n/60$) is the angular velocity of the driving shaft and A (= $\pi l_{total}^2/4$) is the swept area of the rotating cylinder blade.

5.3.1 Effective length ratio l/d

Figure 5-60(a) shows the relationship between C_p and λ calculated from the results of the loaded experiments for each effective length ratio l/d shown in Fig. 5-5. C_p had an upwardly convex curve for all l/d, and C_p took a maximum value at certain λ. The maximum value of C_p ($[C_p]_{max}$) was maximum at l/d = 2.5 and minimum at l/d = 4.5 and was about 2.4 times difference between these C_p values of two l/d. For the range of λ, about 1.4 times difference was observed. Fig. 5-60(b) shows $[C_p]_{max}$ and $\lambda_{[Cp]max}$ for each l/d. As mentioned above, $[C_p]_{max}$ took a maximum value at l/d = 2.5 and then decreased continuously with increasing l/d. $\lambda_{[Cp]max}$ tends to be larger for large $[C_p]_{max}$ and smaller for small $[C_p]_{max}$. $\lambda_{[Cp]max}$ is maximum at l/d = 3, but not at l/d = 2.5 where $[C_p]_{max}$ took maximum value. These results indicate that the performance of the wind turbine is maximized by setting the effective length l/d = 2.5-3.

(a) C_p vs. λ
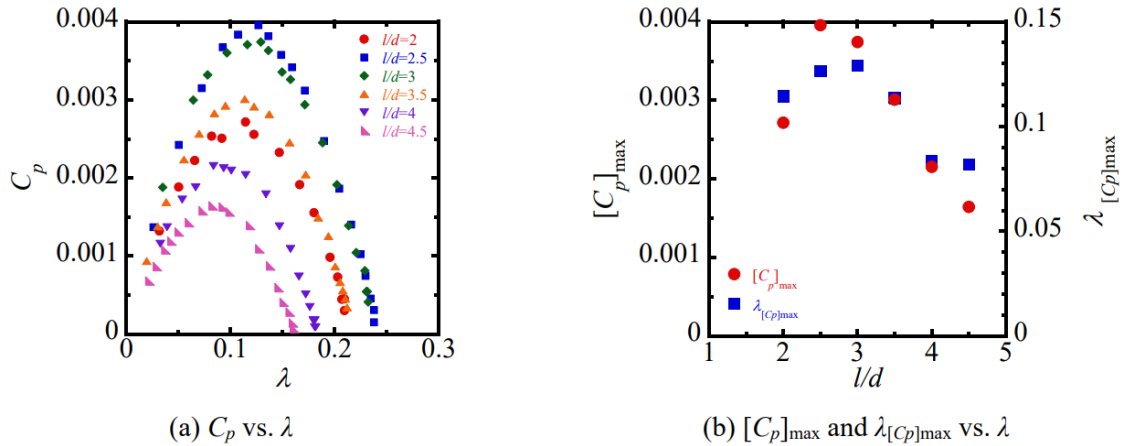
(b) $[C_p]_{max}$ and $\lambda_{[Cp]max}$ vs. λ

Fig. 5-60 Evaluation of wind turbine performance at each value of l/d.

5.3.2 Blade number N

Figure 5-61(a) shows the relationship between C_p and λ calculated from the results of the loaded

experiments for each blade number N. C_p had an upwardly convex curve for almost N, and C_p took a maximum at $N = 12$. The range of λ was minimum at $N = 2$ and maximum at $N = 10$, resulting in a difference of about 1.5 times. Fig. 5-61(b) shows $[C_p]_{max}$ and $\lambda_{[Cp]max}$ for each N. $[C_p]_{max}$ increased almost linearly with increasing N in the range of $2 \leq N \leq 8$. When the blade number increased from $N = 2$ to 4, $[C_p]_{max}$ also increased about 2.0 times, and when the blade number increased from $N = 4$ to 8, $[C_p]_{max}$ increased about 2.2 times. That is, $[C_p]_{max}$ increased almost as much as the rate of increase of N in the range of $2 \leq N \leq 8$. $[C_p]_{max}$ in $N \geq 8$ was almost constant for N. $\lambda_{[Cp]max}$ increased gradually with increasing N. That is, $\lambda_{[Cp]max}$ became large under conditions where $[C_p]_{max}$ is large.

(a) C_p vs. λ (b) $[C_p]_{max}$ and $\lambda_{[Cp]max}$ vs. λ
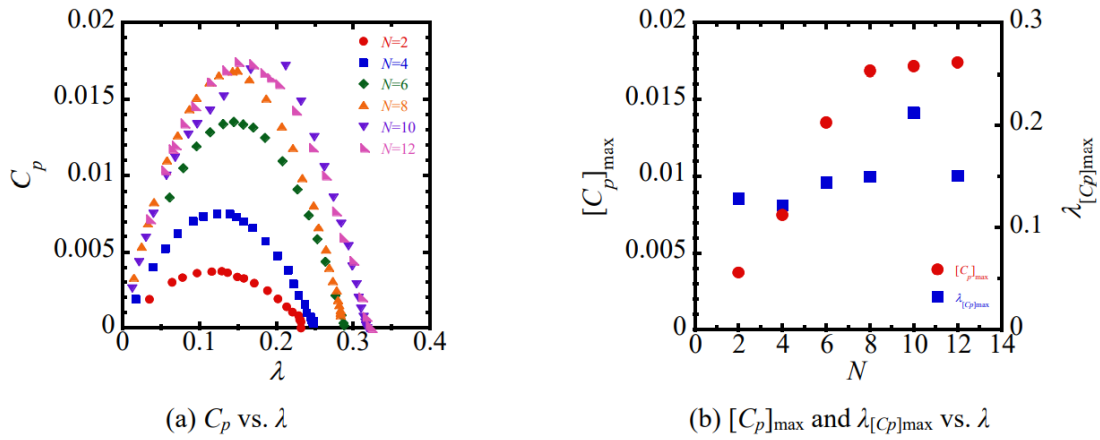
Fig. 5-61 Evaluation of wind turbine performance at each value of l/d.

5.3.3   Effective blade diameter d

Figure 5-62(a) shows the relationship between C_p and λ calculated from the results of the loaded experiments for each blade diameter d of the stepped circular cylinder blade at $l = 60$mm and $N = 2$. C_p had an upwardly convex curve for $d = 20$ and 25mm, but the rotation suddenly stopped for $d = 23, 28, 30$mm by the instability of formation of NV. Fig. 5-62(b) shows $[C_p]_{max}$ and $\lambda_{[Cp]max}$ for each d. For $N = 2$, $[C_p]_{max}$ is expected to increase with increasing d, assuming the interference effect by the wake does not occur. The actual $[C_p]_{max}$ varied with increasing d due to the instability in the formation of NV. $\lambda_{[Cp]max}$ tended to increase with increasing d.

(a) C_p vs. λ (b) $[C_p]_{max}$ and $\lambda_{[Cp]max}$ vs. λ

Fig. 5-62 Evaluation of wind turbine performance at each value of d at $N = 2$.

Figure 5-63(a) shows the relationship between C_p and λ calculated from the results of the loaded experiments for each d at $N = 4$. C_p had an upwardly convex curve for $d = 20$ and 25mm. Although parabolic maximums were obtained at $d = 23$, 28, and 30 mm, the rotation stopped suddenly at large λ. Fig. 5-63(b) shows $[C_p]_{max}$ and $\lambda_{[Cp]max}$ for each d. $[C_p]_{max}$ varied with increasing d by the instability in the formation of NV, and $\lambda_{[Cp]max}$ tended to increase with increasing d.

(a) C_p vs. λ (b) $[C_p]_{max}$ and $\lambda_{[Cp]max}$ vs. λ

Fig. 5-63 Evaluation of wind turbine performance at each value of d at $N = 4$.

Figure 5-64(a) shows the relationship between C_p and λ calculated from the results of the loaded experiments for each d at $N = 8$. C_p had an upwardly convex curve for all d. Fig. 5-64(b) shows $[C_p]_{max}$ and $\lambda_{[Cp]max}$ for each d. Both $[C_p]_{max}$ and $\lambda_{[Cp]max}$ increased with increasing d. As the loaded experiments shown in Fig. 5-37, the maximum load torque $[T_{brake}]_{max}$ decreased at $d = 28$ and 30mm by the interference effect by the wake on the rotational motion. On the other hand, the relationship between U and n in the un-load experiments shown in Fig. 5-34 showed that n at an arbitrary U increased with increasing d in the range of

$U \geq 5$m/s. By this large rotational speed at the large d, $[C_p]_{max}$ increased with increasing d.

(a) C_p vs. λ
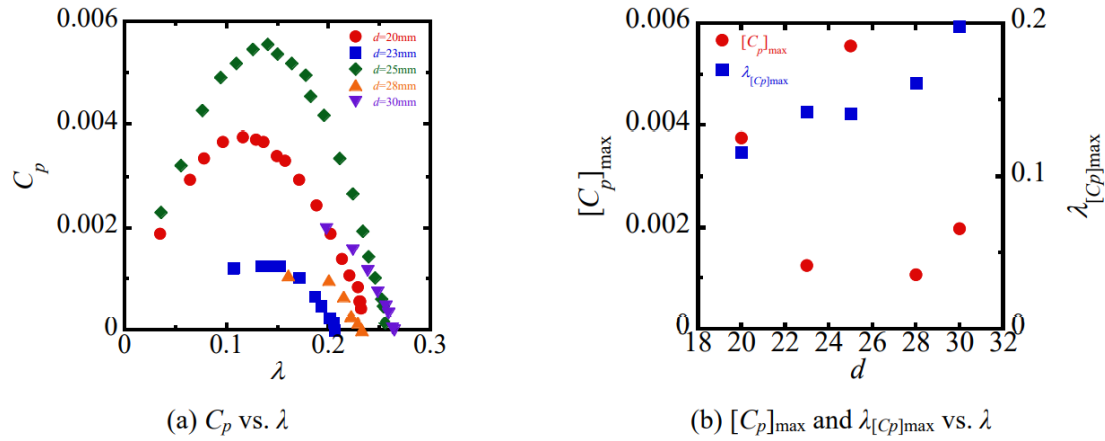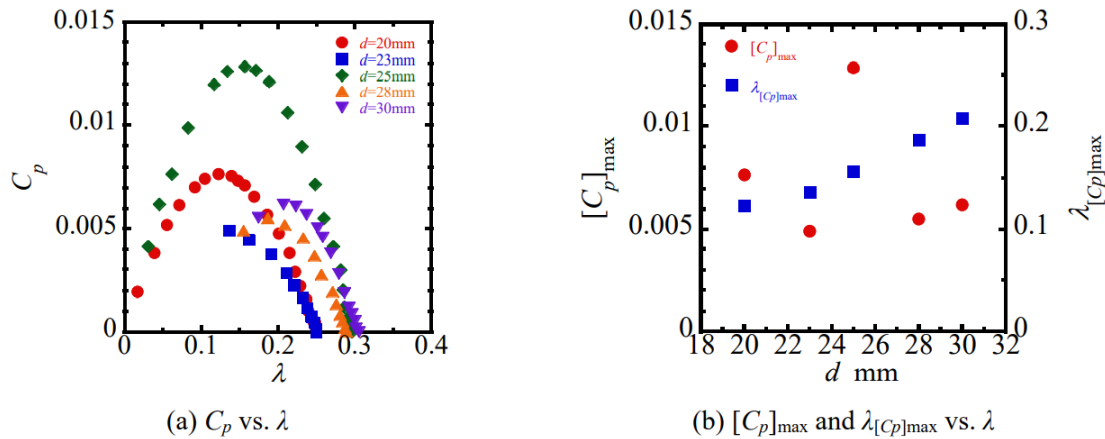
(b) $[C_p]_{max}$ and $\lambda_{[Cp]max}$ vs. λ
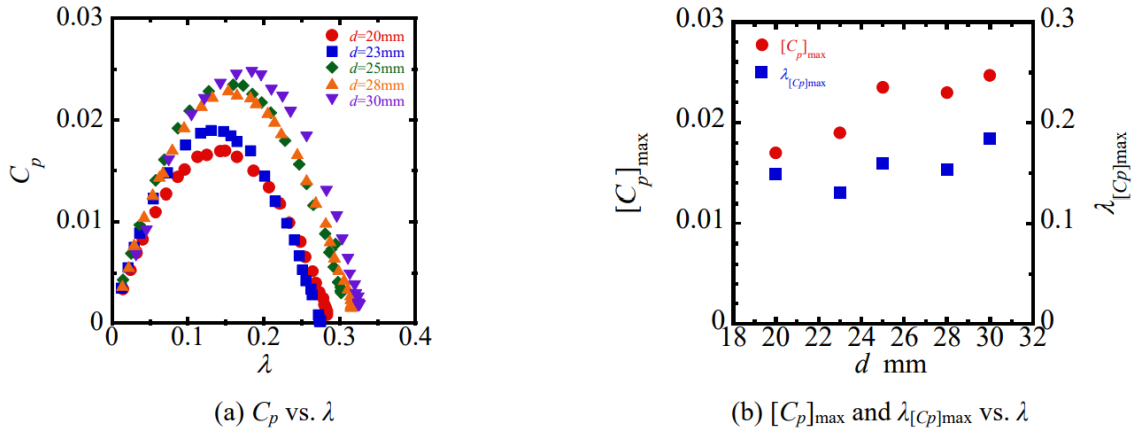
Fig. 5-64 Evaluation of wind turbine performance at each value of d at $N = 8$.

Figure 5-65(a) shows the relationship between C_p and λ calculated from the results of the loaded experiments for each d at $N = 10$. C_p changed to be an upwardly convex curve with respect to changes in λ for all λ ranges for $d = 20$, 23, and 25mm. For $d = 28$ and 30mm, C_p increased linearly with decreasing λ in the range of $0.3 \leq \lambda \leq 0.35$ by the effect of high rotational speed. In the range of $0.3 \geq \lambda$, where the effect of the high rotational speed disappeared, and C_p changed to become a convex curve upward as in the other d cases. The results of Fig. 5-65(b) showed that $[C_p]_{max}$ becomes constant for the same N when the interference effect by the wake on the rotational motion occurs, and $\lambda_{[Cp]max}$ becomes also almost constant except for $d = 20$mm.

(a) C_p vs. λ

(b) $[C_p]_{max}$ and $\lambda_{[Cp]max}$ vs. λ
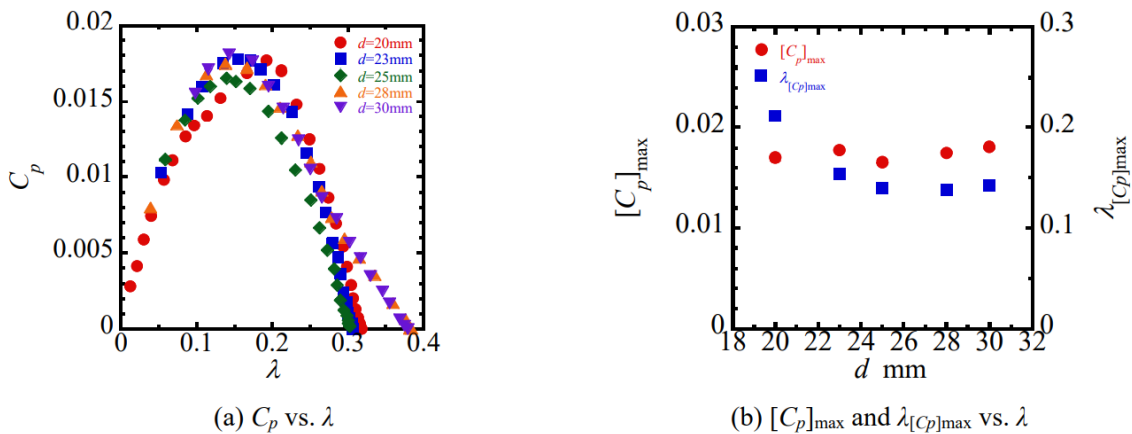
Fig. 5-65 Evaluation of wind turbine performance at each value of d at $N = 10$.

5.3.4　Pitch ratio t/d

$[C_p]_{max}$ and $\lambda_{[Cp]max}$ for the pitch ratio t/d were organized by using the relationship between of d and $[C_p]_{max}$ and $\lambda_{[Cp]max}$ for each N in the previous subsection. The results are shown in Fig. 5-66. Although $[C_p]_{max}$ varied, it increased with the decrease in t/d and decreased rapidly in $t/d > 1$. This result means that although the performance of the wind turbine is greatly improved by setting a narrower t/d, the interference effect by the wake on the rotational motion, which occurred by the extremely small t/d, reduced the performance. The increase in d seemed to have a significant effect on the variation of $\lambda_{[Cp]max}$.

(a) C_p vs. λ　　　　　(b) $[C_p]_{max}$ and $\lambda_{[Cp]max}$ vs. λ

Fig. 5-66 Evaluation of wind turbine performance using t/d.

5.4 Conclusions

The stepped circular cylinder blade is considered to be a most promising and practical configuration for the cylinder blade wind turbine at the present stage. The influences of the effective length l, the number N, and diameter d on the rotation, output torque, and performance characteristics of the stepped circular cylinder blade wind turbine are investigated.

The conclusions obtained from the experimental results and discussions are summarized as follows.

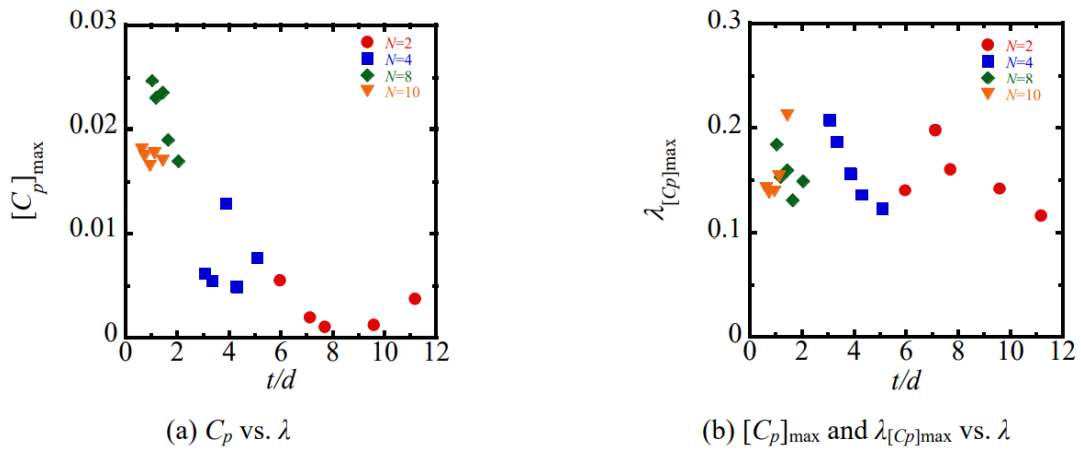1. The performance of cylinder blade wind turbine such as the output torque and power coefficient are largely improved by the stepped circular cylinder blade with the effective length ratio $l = 60$mm ($l/d = 3$) at $d = 20$mm. This is because the generation of driving torque by NV is unaffected while the fluid resistance against the rotation is reduced by decreasing the sizes of ineffective parts of the cylinder blade.

2. The lift coefficient of NV per stepped circular cylinder blade C_{la} was constant at the range of blade number of $N \leq 8$ at $d = 20$mm and $l = 60$mm ($l/d = 3$), but C_{la} decreased at $N \geq 10$ due to interference effects by the wake on the rotational motion.

3. In the range of the pitch ratio of $t/d < 2$, C_{la} was reduced due to the interference effect by the wake on the rotational motion of the cylinder blades. By further narrowing the range of t/d at high flow velocities, the effect of high rotation occurred, and the rotational speed of the cylinder blade increased rapidly.

4. The formations of NV and the suction flow was stable at the narrow t/d of $t/d < 2$, and this effect was seen as a continuous decrease in the C_{la}.

5. $l = 60$mm and $t/d \simeq 2$ is recommended as the optimum configuration for the stepped circular cylinder blade wind turbine.

References

[1] Hemsuwan, W., Sakamoto, K., Takahashi, T., 2018a. Lift force generation of a moving circular cylinder with a strip-plate set downstream in cruciform arrangement: flow field improving using tip ends, International Journals of Aeronautical and Space Sciences, Vol. 19, Issue 3, 606-617.

[2] Hemsuwan, W., Sakamoto, K., Nakada, S., Takahashi, T., 2018b. A longitudinal vortex wind turbine: numerical study, Journal of Wind Engineering and Industrial Aerodynamics, Vol. 180, 213-230.

6. Axial drag force in the mainstream direction

When the longitudinal vortex (LV) is formed stably behind the moving direction of the circular cylinder blade, a strong negative pressure region is generated between the circular cylinder blade and the ring-plate placed downstream, and the force acts on the circular cylinder blade. This force is thought to act on the circular cylinder blade as a lift force in the rotational direction and a drag force (thrust force) in the mainstream direction. The effects of the configurations and structural parameters on characteristics of the axial drag force in the mainstream direction were investigated. The axial drag force is measured for the continuous increase in the flow velocity and gap ratio, and the drag force characteristics are investigated. The relationship between the axial drag coefficient and Reynolds number is obtained from the experimental results, and the stability of the LV due to the changes in the experimental conditions and structural parameters is evaluated from the behavior of axial drag coefficient.

6.1   Objectives of axial drag force measurement

The lift coefficient (C_L) and the drag coefficient (C_D) against the rotation of the single circular cylinder blade under steady rotating was approximated from the result of the loaded experiments in Chapter 4. Assuming C_L as the linear function of the velocity ratio λ ($C_L = C_{la}-C_{lb}\lambda$) and C_D as the constant value, the relationships between rotational seed n and flow velocity U under un-loaded condition and between the power coefficient C_p and the velocity ratio λ are fairly well predicted for the widely varying conditions. C_L and C_D in these chapters are the dimensionless forces for the rotating circular cylinder blade.

The forces acting on the circular cylinder blade due to the longitudinal vortices (LVs) are mainly classified into two forces: the lift force acting in the rotational direction and the drag force acting in the mainstream direction (thrust force). This drag force is called as the axial drag force in this chapter. When the force of LVs increases by changes in structural parameters and experimental conditions, i.e., when the negative pressure region generated in the moving direction of circular cylinder blade expands or becomes stronger, the two forces are expected to increase.

In both numerical calculations for circular-cylinder/strip-plate cruciform system and circular cylinder blade wind turbine by our research team, the lift force of the moving or rotating direction of the cylinder (C_L) and the drag coefficient on the mainstream direction, i.e., the axial drag coefficient ($C_{D.U}$) were evaluated. In the numerical simulation for the circular-cylinder/strip-plate system, where the upstream circular cylinder moves parallel to the strip-plate with a constant velocity while keeping the constant gap ratio s/d, the effect of velocity ratio VR (= V_{cy}/U, V_{cy}: moving velocity of the cylinder, $Re = 1.3*10^4$) on the distribution of the local lift coefficient ($C_{L\,local}$) and the local axial drag coefficient ($C_{D.U\,local}$) on the spanwise direction of the circular cylinder was investigated [1]. In the all range of VR = 0.05-0.2, $C_{D.U\,local}$ was a minimum at the center of the cross-section of the circular cylinder and the strip-plate, increased as receding from the cross-section and reached a maximum near the rim of the strip-plate, and then rapidly decreased toward the tip-end of the cylinder. This distribution of $C_{D.\,U\,local}$ was symmetrical to the center of the cross-section. The integrated value of the local axial drag coefficient ($C_{D.U}$) in all range of VR was $C_{D.U}$ = 1.2-1.4. Since the axial drag coefficient of the common cylinder at the same Re is 1.0-1.2 [2], $C_{D.U}$ slightly increased by the formation of the LVs. In order to investigate the effect of the velocity ratio λ on the distribution of the local lift coefficient ($C_{L\,local}$) and the local axial drag coefficient ($C_{D.U\,local}$) on the spanwise direction of the stepped circular cylinder blade, the numerical calculation was carried out in the range of λ = 0.05-0.2 for the simulated stepped circular cylinder blade wind turbine with $N = 2$ [3]. λ (= V_{cy}/U) is a dimensionless number determined by dividing the moving velocity of the circular cylinder blade at the center diameter of the ring-plate ($V_{cy} = 0.5D\omega$, $\omega = 2\pi n/60$) by the flow velocity $U = 10$m/s, and the stepped circular cylinder blade rotated at a constant λ along the downstream ring-plate with a constant s/d. The tendency of distribution of $C_{D.U\,local}$ was similar for the above circular-cylinder/strip-plate system with a slight difference between inside and outside of the ring-plate. The relationship between λ and the integrated axial drag coefficient was $C_{D.U}$ = 1.2-1.3 at any λ.

The high axial drag force of the circular cylinder blades and the ring-plate placed downstream is a disadvantage of the circular cylinder blade wind turbines, and the axial drag force needs to be reduced for the robustness of the wind turbine for practical use. Therefore, this chapter evaluates the effects of changes in structural parameters and experimental conditions on the characteristics of axial drag force. The reduction in axial drag force are also evaluated in the stepped circular cylinder blade wind turbine which the unnecessary regions for the forming of NV was removed. The relationship between the axial drag coefficient and the Reynolds number is obtained from the experimental results, and the behavior of forces acting on the mainstream direction (thrust direction) by the LVs is investigated.

6.2   Drag force for single circular cylinder blade wind turbine

The validity of the axial drag force measured by the experimental apparatus was evaluated from the measurement result of the drag force at cylinder only condition. Fig. 6-1 shows the transition of the axial drag force $F_{D.U}$ with increasing flow velocity U at cylinder only, and the relationship between the axial drag coefficient $C_{D.U}$ and the Reynolds number Re calculated by the following equations.

$$Re = \frac{Ud}{\nu} \qquad (6-1)$$

$$C_{D.U} = \frac{F_{D.U}}{0.5\rho U^2 dL} \qquad (6-2)$$

The kinematic viscosity ν and the density ρ in air at 20°C were used in this chapter. $F_{D.U}$ acting on the single circular cylinder blade increased exponentially with the increase of U. The drag coefficient gradually increased in the range of $C_{D.U} = 0.8$-1.0 with the increase of Re. This measured value of $C_{D.U}$ was slightly smaller compared with the theoretical value $C_{D.U} = 1.0$-1.2 of a long cylinder placed perpendicular to the flow in the same range of Re [2]. It is considered that the Karman vortex (KV) forming from the single circular cylinder blade was disordered by some factors such as the driving shaft attached to the center of the single circular cylinder blade and the tip effect acting on the tip-ends of blade tips, and $C_{D.U}$ became smaller than the theoretical value. However, since the difference between the experimental and the theoretical drag coefficients was very small, this experimental result is considered to be valid and the experiments described later were carried out.
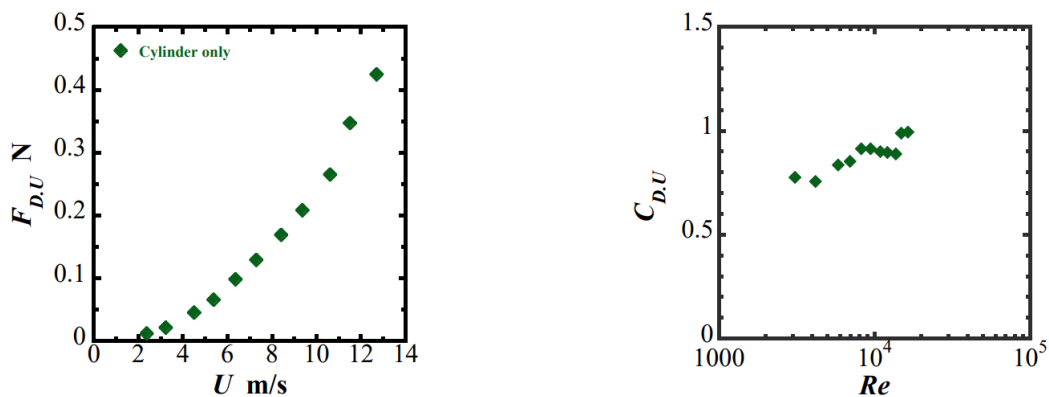
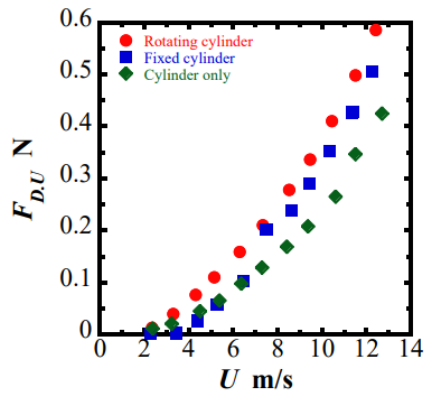(a) Drag force vs. flow velocity   (b) Drag coefficient vs. Reynolds number

Fig. 6-1 Drag force and Reynolds number at cylinder only.

Figure 6-2 shows the relationships between $F_{D.U}$ and U, $C_{D.U}$ and Re at the three conditions shown in Subsection 2.3.5 and the relationship between the rotational speed n and U at rotating cylinder. At all conditions, $F_{D.U}$ increased exponentially with the increase of U. The value of $F_{D.U}$ in each U was the largest

at rotating cylinder and the smallest at cylinder only throughout the measurement range of U. The axial drag coefficients $C_{D.U}$, which is a normalized $F_{D.U}$, showed complex behavior in the low Re at rotating and fixed cylinders, and tends to be constant in the high Re of $Re > 10^4$. $C_{D.U}$ were stable at $C_{D.U} \simeq 1.5$ in rotating cylinder, at $C_{D.U} \simeq 1.3$ in fixed cylinder, and at $C_{D.U} \simeq 0.9$ in cylinder only. It is considered that the following phenomena occur at each condition of the single circular cylinder blade in the wind turbine apparatus installed in a uniform flow.

(1)   Rotating cylinder: The LVs forms stably with the rotating single circular cylinder blade.

(2)   Fixed cylinder: The LVs irregularly forms from the top and bottom of the single circular cylinder blade. At these two conditions, KV also forms at the same time in the outside region of the LVs forming on the single circular cylinder blade.

(3)   Cylinder only: Only KV regularly forms from the top and bottom of the single circular cylinder blade. From the difference in these phenomena on the single circular cylinder blade, $F_{D.U}$ by the LVs was larger than that by the KV only. The complex behavior of $C_{D.U}$ in small Re in rotating and fixed cylinders is thought to be related to the unstable forming of LVs and the tip-effect and so on.

  In the experiments for the rotating cylinder, the rotational speed n was measured simultaneously with the measurement of the axial drag force. The single circular cylinder blade started steady rotating at the minimum flow velocity of wind tunnel of $U \simeq 2$m/s, and n increased linearly with increasing U. Therefore, the relative attack angle α, determined by the rotating velocity of the single circular cylinder blade and U as shown in Eq. (2-3), is assumed to be constant. Considering the change of the flow velocity which the single circular cylinder blade starts steady rotating U_0, the converted relative attack angle α' was calculated from the relationship between the converted flow velocity $U' (= U-U_0)$ and n. The relationship between U' and α' is shown in Fig. 6-2(d). The converted relative attack angle α' was almost constant throughout all U', but slight fluctuation of α' was observed in small U' around $6 \leq U'$ m/s. The range of converted velocities at $6 \leq U'$ m/s corresponds to the region where $C_{D.U}$ fluctuates in the relationship between $C_{D.U}$ and Re shown in Fig. 6-2(b), it is suggested that α' was also affected by the complex flow by LVs and the tip-effect.
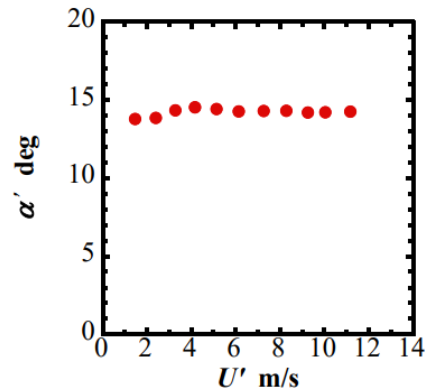
(a) Drag force vs. flow velocity
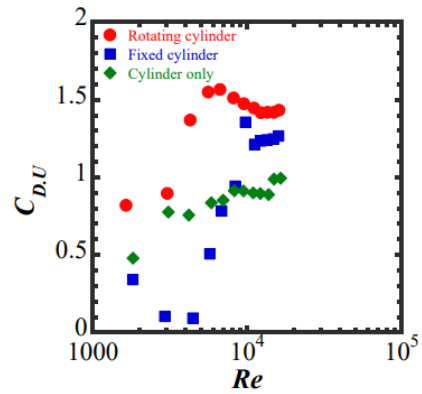
(b) Drag coefficient vs. Reynolds number
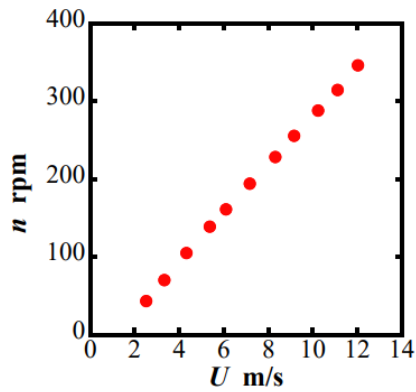
(c) Rotational speed vs. flow velocity

(d) Relative attack angle vs. flow velocity

Fig. 6-2 Drag force and drag coefficient at three conditions and rotational speed at rotating cylinder.

The effect of s/d on $F_{D.U}$ at a constant flow velocity was investigated. Fig. 6-3(a) shows the transition of $F_{D.U}$ with the stepwise increase of s/d from 0.2 to 0.5 at $U = 12$m/s at rotating cylinder and fixed cylinder in which LVs form. The result of $F_{D.U}$ at cylinder only at $U = 12$m/s is also shown as a broken line. The relationship between n and s/d at rotating cylinder is shown in Fig. 6-3(b). $F_{D.U}$ at both rotating cylinder and fixed cylinder were almost equal as that at cylinder only in $s/d = 0.2$-0.3 and rapidly increased at $s/d = 0.325$ at rotating cylinder and $s/d = 0.35$ at fixed cylinder, and then decreased with the increase of s/d. $F_{D.U}$ at rotating cylinder was larger than that at fixed cylinder in $s/d \geq 0.325$. n at rotating cylinder became maximum when the single circular cylinder blade started rotating at $s/d = 0.325$, and then decreased continuously with the increase of s/d. These experimental results show that only KVs were formed at $s/d > 0.325$ in both rotating and fixed cylinders, and the LVs, especially the necklace vortex (NV) were formed near $s/d = 0.325$. The increase in s/d caused the decrease of the lift force by the NV and n decreased. As the result, the drag force by LVs acting on the single circular cylinder blade also decreased. The difference of the value of $F_{D.U}$ between rotating cylinder and fixed cylinder was due to the difference of the forming condition of LVs.

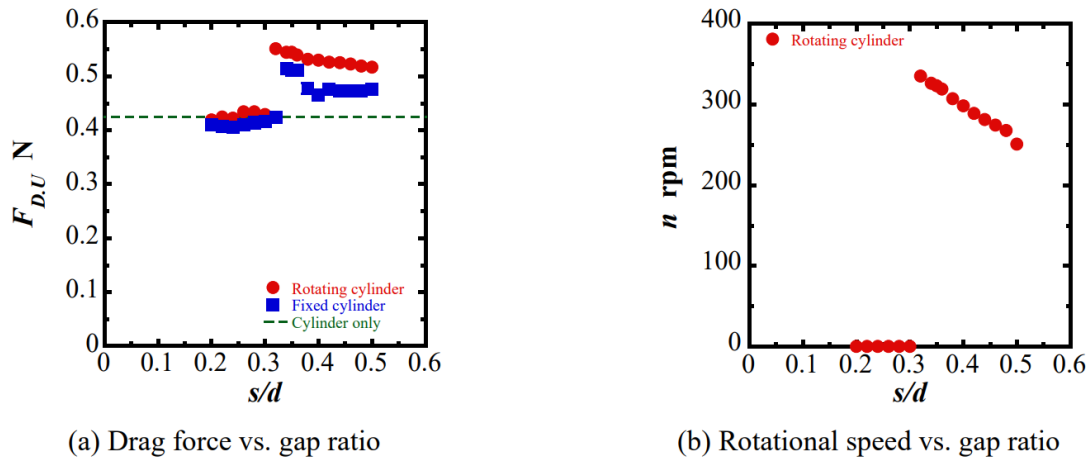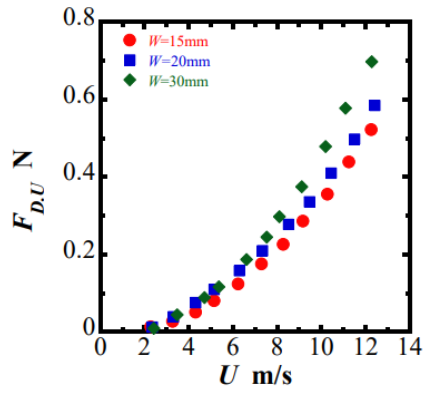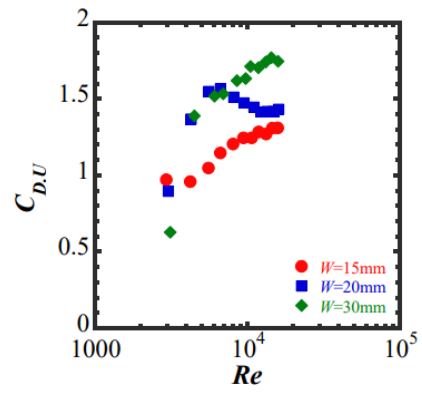(a) Drag force vs. gap ratio | (b) Rotational speed vs. gap ratio

Fig. 6-3 Drag force and rotational speed at increasing gap ratio at three condition.

Figure 6-4 shows the transition of $F_{D,U}$ and n with the increase of U and the relationship between $C_{D,U}$ and Re, and the relationship between α' and U' for each ring-plate width of $W = 15, 20, 30$mm at rotating cylinder. $F_{D,U}$ increased exponentially with the increase of U for all W. $F_{D,U}$ also increased with increasing W in the constant U in the range of $U \geq 6$m/s. $C_{D,U}$ increased monotonically with increasing Re at $W = 15$ and 30mm, and tended to be constant in large Re. In the case of $W = 20$mm, $C_{D,U}$ was close to the value of $C_{D,U}$ of $W = 30$mm for $Re < 5000$ but was close to the value of $C_{D,U}$ of $W = 15$mm in large Re. The following phenomena are considered to be related to the change in $C_{D,U}$; the ratio of acting region where lift force by LVs and drag force was changed by changing of the ring-plate in fixed single circular cylinder blade length, the LVs steadily formed by the increase of U, and the tip-effect. Fig. 6-4(c) shows the relationship between W and $F_{D,U}$ at $U = 12$m/s. $F_{D,U}$ increased almost linearly with the increase of W. The NV that generates the steady lift forms along the ring-plate. Therefore, it is considered that when W was increased on a single circular cylinder blade with the same diameter and total length, the spanwise length of NV increased, and $F_{D,U}$ acting in the mainstream direction increased as well as the lift force acting in the rotational direction.

Figure 6-5 show the rotational speed n of the rotating cylinder and the converted relative angle of attack α' measured simultaneously with the axial drag force. n increased linearly with the increase of U for all W but α' shown in Fig. 6-5(b) had slight fluctuation while remaining almost constant. In particular, α' tended to fluctuate up to large U' at lower W suggests that the force by the LV was unstable at small W and stabilized with the increase of flow velocity. However, the significant correlation between the change in $C_{D,U}$ and W shown in Fig. 6-4(b) was not confirmed.

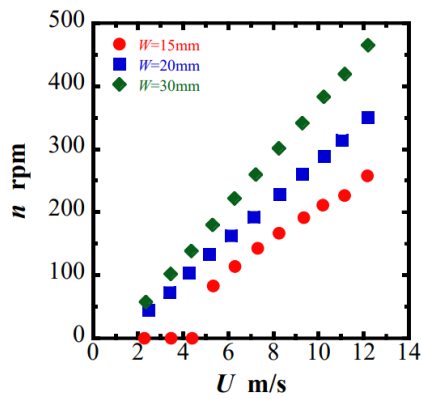(a) Drag force vs. flow velocity

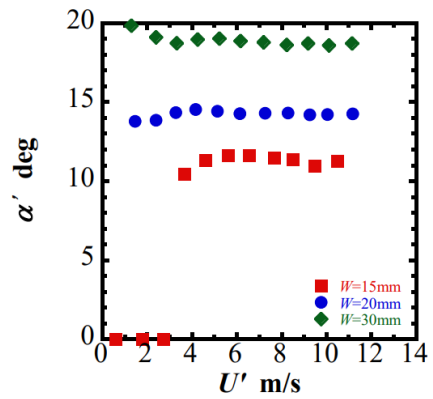(b) Drag coefficient vs. Reynolds number
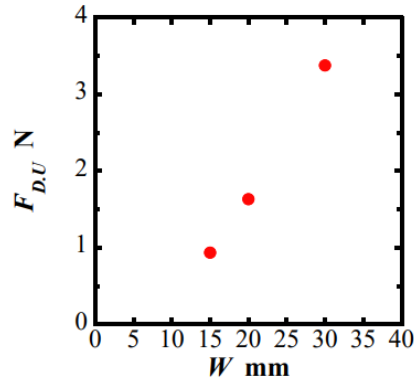
(c) Drag force vs. ring-plate width

Fig. 6-4 Characteristics of drag force for each ring-plate width.

(a) Rotational speed vs. flow velocity

(b) Relative attack angle vs. flow velocity

Fig. 6-5 Characteristics of rotational speed for each ring-plate width.

112

6.3 Drag force for stepped circular cylinder blade wind turbine

Figure 6-6 shows the transition of $F_{D.U}$ and n with the increase of U in each blade number N and the relationship between $C_{D.U}$ and Re at rotating cylinder condition of stepped circular cylinder blade wind turbine. $C_{D.U}$ for stepped circular cylinder blade was calculated following equation.

$$C_{D.U} = \frac{F_{D.U}}{0.5\rho U^2 dlN} \tag{6-3}$$

$F_{D.U}$ increased exponentially with increasing U for all N, and $F_{D.U}$ at a given U was larger for larger N in the range of $U \geq 4$m/s. The comparison with the relationship between $F_{D.U}$ and U of the rotating cylinder of the single circular cylinder blade wind turbine shown in Fig. 6-2(a) indicated that the axial drag force also decreases by removing the ineffective region where the lift force by NV does not generate. As shown in Fig. 6-6(b) $C_{D.U}$ for each N in $Re > 10^4$ decreased with increasing N until $N = 6$-8 but increased with increasing N when N is larger than $N = 6$. The behavior of the change in $C_{D.U}$ for the increase in Re tended to be large or be more complex as N increased. As shown in Fig. 6-6(c), n increased linearly with the increase of U for all N. Comparison with the relationship between n and U for the rotating cylinder of the single circular cylinder blade wind turbine shown in Fig. 6-2(c) showed that the stepped circular cylinder blade is almost ineffective for the change of the rotational speed. Fig. 6-7 shows the relationship between n and N and the relationship between α' and U' at constant flow velocities of $U = 6$, 9 and 12m/s. The systematic change in n with increasing N was not observed in any of U, and n scattered over the wide range with increasing U. α' for each N tended to be constant as U' increased, but the systematic change of α' with the increase of N was not confirmed. Comparing the relationship between α' and U' at each N with the relationship between $C_{D.U}$ and Re shown in Fig. 6-6(b), it was found that α' and $C_{D.U}$ varied for small U' (Re) and became stable with increasing U' (Re). Fig. 6-8 shows the relationship between $F_{D.U}$ and N and the relationship between the drag force acting per stepped circular cylinder blade ($F_{D.U}/N$) and N at a constant flow velocity $U = 12$m/s. $F_{D.U}$ increased linearly with increasing N and $F_{D.U}/N$ became constant for almost all N except $N = 2$.

These results indicated that the axial drag force is reduced by using the stepped circular cylinder blade while keeping the rotational speed. On the other hand, the force by the LVs, which is unstable at low flow velocities in also the stepped circular cylinder blade wind turbine, was stabilized by increase of flow velocity. The axial drag force characteristics of the stepped circular cylinder blade wind turbine are considered to be affected by the tip effect, instability of formation of LVs on each blade, and the pitch distance between the cylinder blades. The LVs forms from each stepped circular cylinder blade independently of each other at small N. However, the formation of the LVs is affected by the adjacent stepped circular cylinder blades as N increases as shown in Chapter 5. This interference effect by the wake on the rotational motion of the cylindrical blade affected the stability of the LVs formation, resulting in the large change and complex behavior of $C_{D.U}$ with increasing Re for large N, and the decrease of $C_{D.U}$ with increasing N for $Re > 10^4$ and $N \geq 8$.
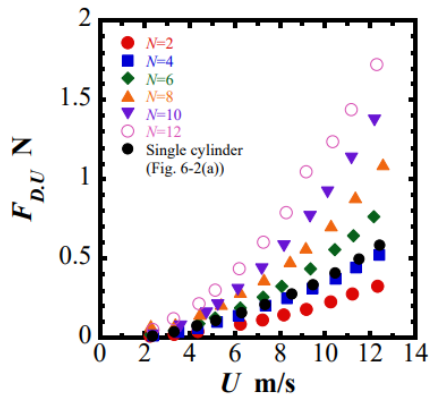
(a) Drag force at rotating cylinder
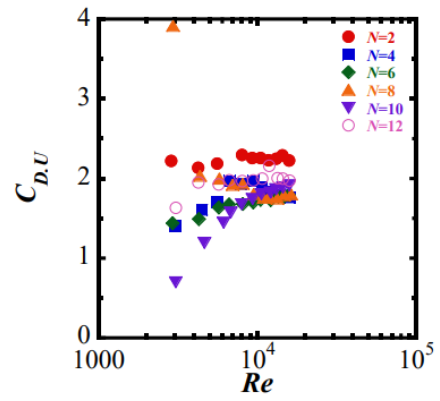
(b) Drag coefficient at rotating cylinder
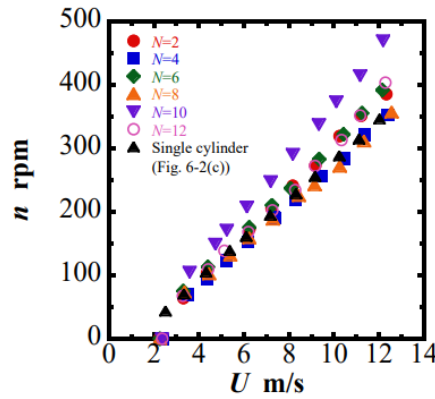
(c) Rotational speed vs. flow velocity

Fig. 6-6 Drag force and rotation characteristics of rotating stepped circular cylinder blade for each blade number.
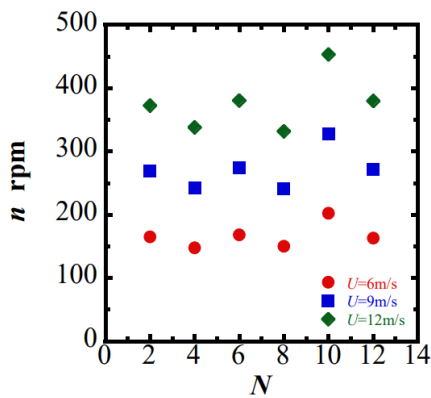
(a) Rotational speed vs. blade number
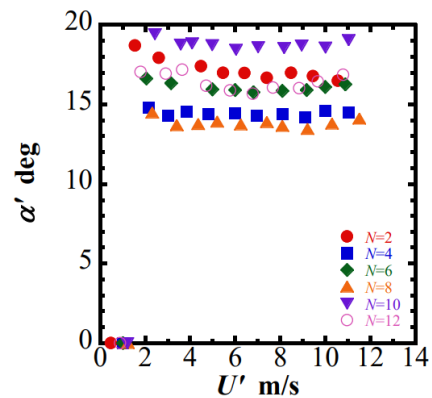
(b) Relative attack angle vs. flow velocity

Fig. 6-7 Rotational characteristics of stepped circular cylinder blade for each blade number.

Fig. 6-8 Drag force characteristics of stepped circular cylinder blade in each blade number at $U = 10$m/s.

6.4　Conclusions

The axial drag force (thrust force) $F_{D.U}$ by the forming of the longitudinal vortices (LVs) acting on the circular cylinder blade wind turbines was measured and its characteristics were investigated. The conclusions obtained from the experimental results and discussion are below.

1. When the LV, especially necklace vortex (NV) was formed behind the moving direction of circular cylinder blade, the strong 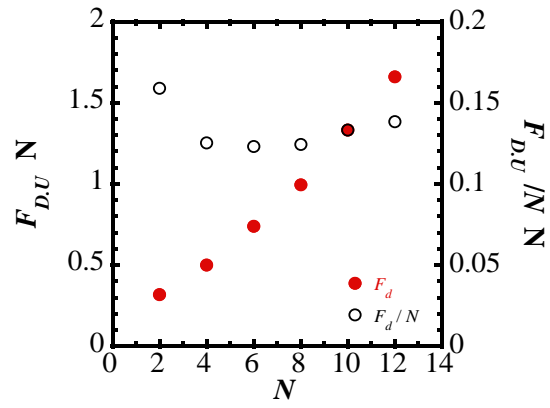negative pressure region was generated between the circular cylinder blade and the ring-plate, and the lift force acted in the rotational direction and axial drag force (thrust force) acted in the mainstream direction on the circular cylinder blade.

2. The axial drag was reduced while the rotational speed was maintained by replacing the single circular cylinder blade with the stepped circular cylinder blade.

3. The rotational speeds of the circular cylinder blades increased linearly with the increase in flow velocity, while the axial drag force increased exponentially. However, at low flow velocities, the relative attack angle calculated from the rotational speed and flow velocity showed slight variation and the axial drag coefficient showed a complicated behavior. Each of these values became constant with the increase of flow velocity.

4. The behavior of the drag coefficient and relative attack angle with increasing flow velocity was expected to be related to the stability of the LVs and occurrence of tip vortices.

References

[1] Hemsuwan, W., Sakamoto, K., Takahashi, T., Lift force generation of a moving circular cylinder with a strip-plate set downstream in cruciform arrangement: flow field improving using tip ends, International Journals of Aeronautical and Space Sciences, Vol. 19, Issue 3 (2018a), pp.606-617.

[2] Schlichting, H., Gersten, K., Boundary layer theory 9th edition (2017), pp.18-19, Springer.

[3] Hemsuwan, W., Sakamoto, K. and Takahashi, T., Numerical investigation of lift-force generation on a moving circular cylinder in a uniform flow driven by longitudinal vortex, Journal of Fluids and Structures, Vol. 83, Issue 20(2018b), pp.448-470.

7. Effect of ring-plate configuration on the performance enhancement

In order to enhance the performance of the cylinder blade wind turbines, dual ring-plate consisted by the two different diameter ring-plates are installed in the downstream of the cylinder blades and this influence is evaluated. The optimum value of the gap between the two ring-plates is determined and this effect is compared with the case of a single ring-plate with $W/d = 1$ and 2 for the single circular cylinder blade wind turbine. The effect of the dual ring-plate of the stepped circular cylinder blade wind turbine is compared with the effect of increasing of blade number at single ring-plate. Based on the experimental results, the structural parameters, by which the effect of dual ring-plate is maximized, is proposed.

7.1   Objectives of the dual ring-plate

In order to investigate the conditions under which large lift force by necklace vortex (NV) is obtained, the loaded and un-loaded experiments were conducted with various structural parameters and shape factors for the single circular cylinder blade wind turbine in Chapter 4 and for the stepped circular cylinder blade wind turbine in Chapter 5. It was suggested that the lift force by the NV was most effectively increased by optimizing the width ratio of the ring-plate W/d for the single circular cylinder blade wind turbine and the pitch ratio t/d for the stepped circular cylinder blade wind turbine and the large performance is obtained. In particular, for the blade number N, which is the parameter determines the pitch ratio t/d in the stepped circular cylinder blade wind turbine, the maximum power coefficient $[C_p]_{max}$ increased almost as much as the rate of increase of N in the absence of the interference effect by the wake on the rotational motion. As the blade number increased and the pitch ratio became below 1, $[C_p]_{max}$ decreases rapidly. Therefore, the blade number attached to the stepped circular cylinder blade wind turbine was limited.

We considered the arrangement of two ring-plates with different diameters as the methods to forming NV without the interference effects of the wake on the rotational motion. Since the NV forms along the downstream ring-plate, the number of NVs formed from one circular cylinder blade becomes double, and the lift force acting on the circular cylinder blade is assumed to be improved. Fig. 7-1 shows the schematic diagram of the flow pattern of NVs between the upstream single circular cylinder blade and the downstream dual ring-plate. When the distance between the dual ring-plates (W_{ring}) is narrow, the NVs or the effective area where lift force is generated at the inside and outside ring-plates interfere with each other, which is thought to affect the various characteristics of the circular cylinder blade wind turbines. The un-load and loaded experiments are conducted on the circular cylinder blade wind turbines with the dual ring-plate as shown in Fig. 2-4(a). In order to confirm the validity of the dual ring-plate, the experimental results are compared to the case where the single ring-plate with the same width as each ring-plate ($W = 20$mm) and the total width of the inside and outside of ring-plates ($W = 40$mm) is attached, and with the same number of NVs formed, i.e., $N = 2$ in the dual ring-plate and $N = 4$ in the single ring-plate.
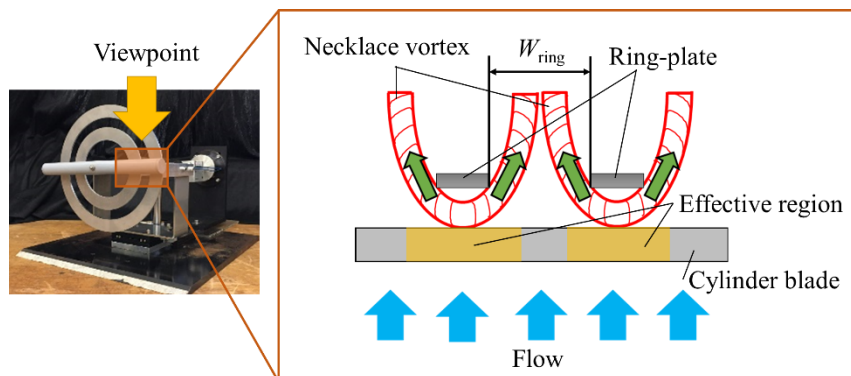

Fig. 7-1 Schematic diagram of formation and shedding of necklace vortex between single circular cylinder blade and dual ring-plate.

7.2 Single circular cylinder blade wind turbine

Figure 7-2 shows the relationship between the rotational speed n and increasing flow velocity U obtained through the un-loaded experiments and the relationship between the load torque T_{brake} and rotational speed n obtained through the loaded experiments for the single circular cylinder blade wind turbine with single ring-plate with $D = 155$mm and $W = 20, 40$mm ($W/d = 1, 2$), shown in Figs. 4-11 and 4-13 in Chapter 4. In the result of un-loaded experiments, the single circular cylinder blade attained the stable rotation at the minimum flow velocity of the wind tunnel $U \simeq 2$m/s, and n increased almost proportionally to U. The difference of the rotational speed between the two W was about 10rpm at $U = 2$m/s and about 190rpm at $U = 12$m/s. In the result of loaded experiments, T_{brake} increased linearly with the decrease of n at $W = 20$mm, but the increase of T_{brake} slightly curved at $W = 40$mm. The comparisons of (1) minimum rotational speed of single circular cylinder blade n_{min}, (2) maximum load torque $[T_{brake}]_{max}$ obtained at n_{min}, and (3) rotational speed range of stable rotation n_{ope} ($= n_{max}-n_{min}$) between $W = 20$ and 40mm are as follows.

(1) n_{min} at $W = 20$mm was about half of $W = 40$mm.

(2) $[T_{brake}]_{max}$ at $W = 20$mm was about 4/5 of $W = 40$mm.

(3) n_{ope} at $W = 20$mm was about 2/3 of $W = 40$mm.

Even if W is doubled, $[T_{brake}]_{max}$ increases only 1.2 times and the lift force by the NV is not simply proportional to W. And since n_{min} increases with the increase of W, it is shown that the increase of W destabilizes the lift force generation by the NV when the load is large and the rotational speed is small.
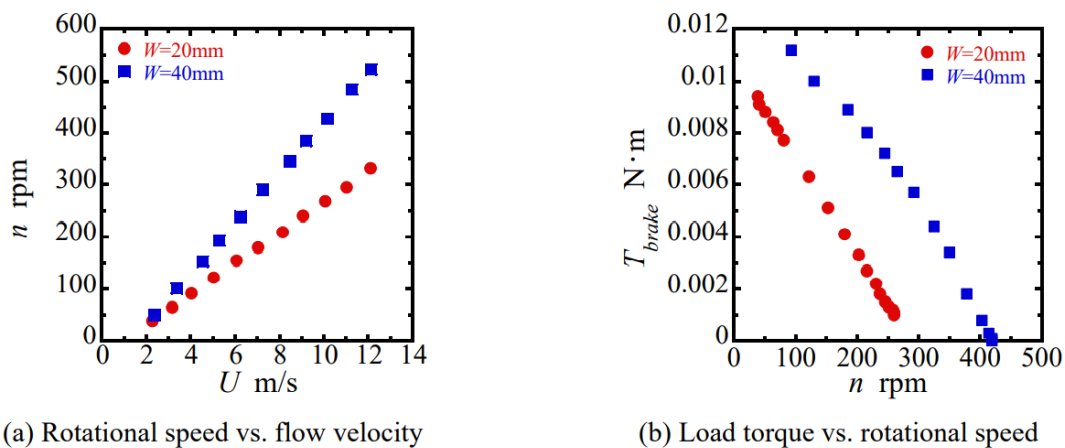

(a) Rotational speed vs. flow velocity

(b) Load torque vs. rotational speed

Fig. 7-2 Results of un-loaded and loaded experiments for single circular cylinder blade wind turbine with single ring-plate. $d = 20$mm, $l_{total} = 220$mm, $W = 20, 40$mm, $D = 155$mm, $s/d = 0.35$.

Figure 7-3 shows the relationship between the rotational speed n and increasing flow velocity U obtained through the un-loaded experiments for the single circular cylinder blade wind turbine with dual ring-plate with the gap between the two ring-plate W_{ring} is 5-30mm. The experimental results of the single ring-plate with $W = 20$ and 40mm shown in Fig. 7-2 are also plotted for comparison. n increased proportionally to U

in each W_{ring}. The minimum flow velocity at which the single circular cylinder blade rotates steadily U_{min} was $U_{min} = 4$m/s at $W_{ring} = 5$ and 10mm, and $U_{min} = 3$m/s at other W_{ring}, i.e., U_{min} did not depend on the change of W_{ring}. In the range of $U_{min} \leq U \leq 6$m/s, the value of n was similar in each W_{ring} in any U, but the difference of n was confirmed with increasing U in the range of $U \geq 7$m/s. When the single ring-plate is placed, U_{min} was $U_{min} = 2$m/s at both $W = 20$ and 40mm and the single circular cylinder blade rotated at lower flow velocity than that of the dual ring-plate. After the start of the rotation, n of $W = 20$mm was lower than that in all W_{ring} of the dual ring-plate in the range of $U \geq 6$m/s, and n of $W = 40$mm was higher than that in all W_{ring} of the dual ring-plate in all U ranges. Fig. 7-4 shows the relationship between W_{ring} and n at $U = 10$m/s obtained through the un-loaded experiments. The experimental results of single ring-plate with $W = 20$ and 40mm are also shown by broken lines for the comparison. n tended to decrease with the increase of W_{ring}. The difference of n was the largest between $W_{ring} = 5$ and 25 mm, which was about 55rpm. The largest difference of n (116 rpm) occurred between the result of the single ring-plate at $W = 20$mm and the result at $W_{ring} = 5$mm and it was confirmed that n increased about 1.4 times by placing the dual ring-plate. On the other hand, the largest difference of n (91 rpm) occurred between the result of $W = 40$mm and the result of $W_{ring} = 25$mm, and n decreased to about 4/5 by separating the width of ring-plate.

In the range of the optimum effective length $l = 50$-60mm of the cylinder blade in the stepped circular cylinder blade wind turbine as determined in Subsection 5.1.1, the protruding length of the stepped circular cylinder blade from the edge of the ring-plate is $l_P = 15$-20mm. It is considered that the lift force by NV does not act outside of this protruding length region. That is, for the dual ring-plate, the effective parts where NV and lift force are generated by the inside and outside ring-plates are considered to be independent of each other under the condition of W_{ring} ($= 2l_P$) $>$ 30-40mm. However, in the W_{ring} range in this study, the above-mentioned interference of the NV and effective part are considered to occur. Furthermore, the comparison between the results of the single ring-plate at $W = 40$mm and the double ring-plate suggests that the separation of the ring-plate, as well as the interference of NVs in the spanwise direction of the single circular cylinder blade, increases the fluid resistance against the direction of rotation.
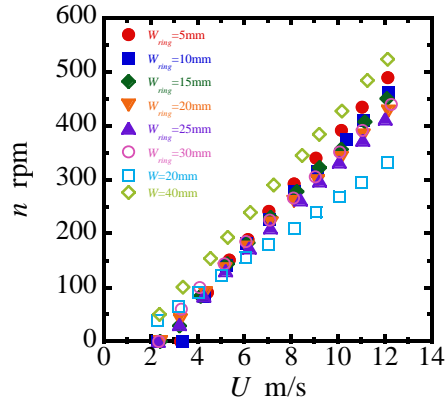
Fig. 7-3 Rotational speed vs. flow velocity through un-loaded experiments for each value of gap between ring-plates compared with single ring-plate with $W = 20$ and 40mm. $d = 20$mm, $l_{total} = 220$mm, $s/d = 0.35$.
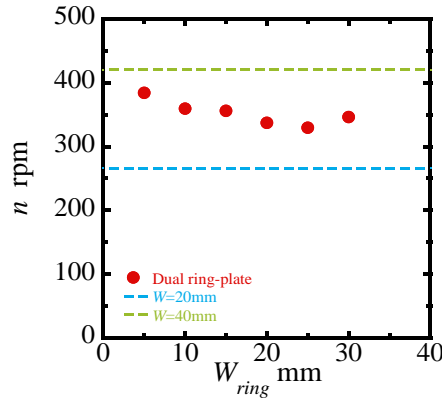

Fig. 7-4 Rotational speed at $U = 10$m/s vs. gap between ring-plates compared with single ring-plate with $W = 20$ and 40mm.

Figure 7-5 shows the relationship between T_{brake} and n at $U = 10$m/s for each W_{ring} obtained through the loaded experiments. The experimental results of single ring-plate with $W = 20$ and 40mm shown in Fig. 7-2(b) are plotted for comparison. T_{brake} increased linearly with the decrease of n except for the slight curvilinear changes at $W_{ring} = 10$mm. The maximum value of T_{brake} ($[T_{brake}]_{max}$) in each W_{ring} was maximum at $W_{ring} = 20$mm and was the minimum at $W_{ring} = 30$mm. In the range of the rotational speed of $100 \leq n \leq 200$rpm, there was no significant difference of T_{brake} of each W_{ring} at a given n. The minimum value of the rotational speed (n_{min}) at $[T_{brake}]_{max}$ tended to decrease at which the large $[T_{brake}]_{max}$ was obtained and increase at which the small $[T_{brake}]_{max}$ was obtained. The result of the loaded experiments of the single ring-plate with $W = 20$mm showed a narrower rotational range and a smaller value of T_{brake} at given n than the results of the dual ring-plate under all conditions of W_{ring}. For the results of the single ring-plate with $W = 40$mm, T_{brake} was larger than that for all conditions of W_{ring} in the range of $n > 200$rpm, but T_{brake} tended to increase with the slight curvilinear changes with the decreasing n and it was similar to the result of $W_{ring} =$

20mm at $n < 150$rpm.

Figure 7-6 shows the transitions of maximum load torque $[T_{brake}]_{max}$ and minimum rotational speed n_{min} at each experimental result for W_{ring}. The experimental results of single ring-plate with $W = 20$ and 40mm are shown as broken lines. $[T_{brake}]_{max}$ increased with increasing W_{ring} in the range of $5 \leq W_{ring} \leq 20$mm and decreased after reaching the maximum value at $W_{ring} = 20$mm. This transition was different from the rotational speed at un-loaded experiments n shown in Fig. 7-4, where n decreased with increasing W_{ring}. The value of $[T_{brake}]_{max}$ for the dual ring-plate exceeded the result of $W = 20$mm for single ring-plate at $5 \leq W_{ring} \leq 25$mm and was 1.4 times larger than that of $W = 20$mm at $W_{ring} = 20$mm. This result showed that the doubling of the number of NVs by the dual ring-plate did not double the driving force by NVs. In the comparison of the experimental results of the single ring-plate with $W = 40$mm and the dual ring-plate, $[T_{brake}]_{max}$ of dual ring-plate exceeded the results of $W = 40$mm in the range of $5 \leq W_{ring} \leq 20$mm and was 1.2 times larger at $W_{ring} = 20$mm.

At $W_{ring} = 20$mm, the protruding length of the cylinder blades from the inside and outside ring-plates is $l_P = 10$mm, respectively, and the NVs formed from each ring-plate are considered to interfere with each other. In other words, the interference of NVs in this W_{ring} condition increased the lift force. When the W_{ring} is larger than $W_{ring} = 20$mm, the formations of NV are independent of each other and the NV formed from the inside ring-plate may be affected by the driving shaft and other factors. On the other hand, when W_{ring} is smaller than $W_{ring} = 20$mm, the flow field approaches that of the case where the single ring-plate with $W = 40$mm is attached. However, the small gap between the ring-plates makes the configuration of the ring-plate that is slit into a single ring plate with a large width. This slit affects the suction flow and NV formation between the single circular cylinder blade and the ring-plate and is considered to reduce the lift force by NV.

The minimum rotational speed n_{min} decreased with increasing W_{ring} in the range of $5 \leq W_{ring} \leq 20$mm, reached the minimum at $W_{ring} = 20$mm, and then increased. That is, n_{min} tends to decrease under the condition that $[T_{brake}]_{max}$ increases. It was only $W_{ring} = 20$mm where n_{min} of the dual ring-plate became smaller than that of single ring-plate of $W = 20$mm. Also, n_{min} of the dual ring-plate became smaller than that of single ring-plate of $W = 40$mm in the range of $10 \leq W_{ring} \leq 20$mm and it almost agreed with the range where $[T_{brake}]_{max}$ is larger than that of $W = 40$mm.
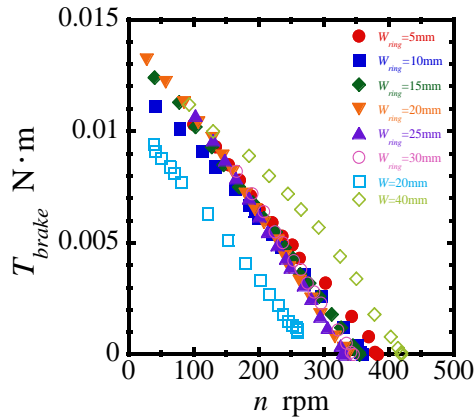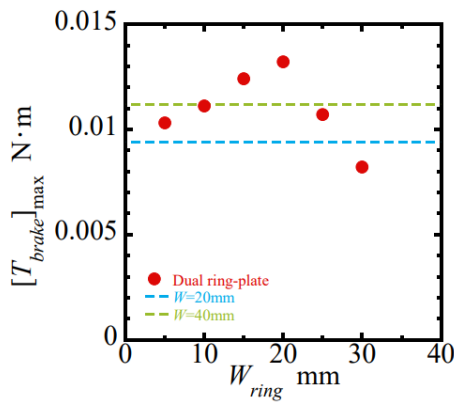
Fig. 7-5 Load torque vs. rotational speed at $U = 10$m/s through loaded experiments for each value of gap between ring-plates compared with single ring-plate with $W = 20$ and 40mm. $d = 20$mm, $l_{total} = 220$mm, $s/d = 0.35$.

(a) $[T_{brake}]_{max}$ vs. gap between ring-plates
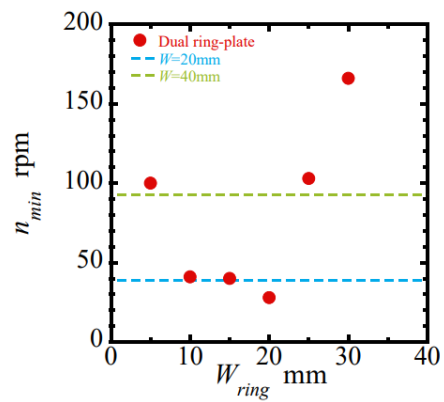
(b) n_{min} vs gap between ring-plates

Fig. 7-6 Effect of gap between ring-plates of dual ring-plate on maximum load torque and minimum rotational speed.

7.3 Stepped circular cylinder blade wind turbine

7.3.1 Effect of ring-plate configuration at $N = 2$

Figure 7-7 shows the relationship between the rotational speed n and increasing flow velocity U for the gap between the two ring-plate W_{ring} for the stepped circular cylinder blade wind turbine of $N = 2$ with dual ring-plate. The steady rotation was not observed at $W_{ring} = 25$mm and n increased proportionally to U in other W_{ring}. The minimum flow velocity at which the stepped circular cylinder blade rotates steadily U_{min} was $U_{min} = 4$m/s at $W_{ring} = 5$mm, $U_{min} = 7$m/s at $W_{ring} = 35$mm, and $U_{min} = 3$m/s at other W_{ring}, U_{min} at $W_{ring} = 35$mm was larger than other conditions. In $5 \leq W_{ring} \leq 20$mm, the significant difference in n was not confirmed in the given U in the range of $U \leq 8$m/s, and n tended to decrease with the increasing of W_{ring} in $U \geq 9$m/s.

Figure 7-8 shows the relationship between W_{ring} and n at $U = 10$m/s obtained through the un-loaded experiments. The experimental results of single circular cylinder blade wind turbine with dual ring-plate shown in Fig. 7-4 are also plotted for the comparison. n tended to slightly decrease with the increasing of W_{ring} in $5 \leq W_{ring} \leq 20$mm and n at $W_{ring} = 30$mm was about 45% smaller than that in above range of W_{ring}. Compared with the results for the single circular cylinder blade wind turbine shown in the red plots, the significant difference in n was not confirmed at $5 \leq W_{ring} \leq 20$mm. This result means that the lift forces acting on the two type of cylinder blades at un-loaded experiments are almost equal in the above range of W_{ring}. In other words, in the un-loaded experiments, it is considered that the fluid resistance force to the rotation acting on the cylinder blades is almost equal in the same W_{ring} at the two types of cylinder blades. The formation of NVs was close to the driving shaft and the hub and these attachments may affect the formation of the NVs and reduced the lift force in $W_{ring} = 25$ and 30mm.
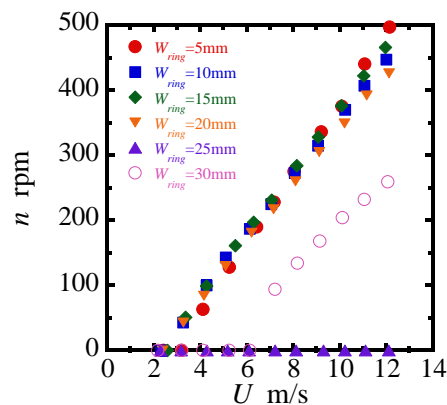

Fig. 7-7 Rotational speed vs. flow velocity through un-loaded experiments for each value of gap between ring-plates of stepped circular cylinder blades wind turbine with dual ring-plate. $d = 20$mm, $s/d = 0.35$.
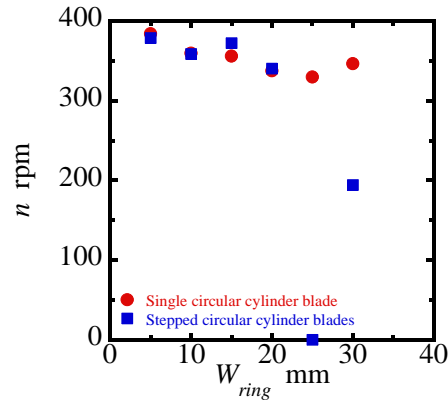
Fig. 7-8 Rotational speed at $U = 10$m/s vs. gap between ring-plates of stepped circular cylinder blades wind turbine with dual ring-plate.

Figure 7-9 shows the relationship between T_{brake} and n at $U = 10$m/s for W_{ring} obtained through the loaded experiments. At, $W_{ring} = 25$mm the steady rotation was not observed at the un-loaded experiments, the loaded experiments were not carried out. T_{brake} increased linearly with the decrease of n in any W_{ring}. Also, at the same rotational speed, T_{brake} decreased with the increase of W_{ring} in $n \geq 150$rpm and increased with the increase of W_{ring} in $n \leq 150$rpm. The maximum value of T_{brake} at $W_{ring} = 30$mm was about 1/4-1/5 and the range of steady rotation was about 1/3 compared to other W_{ring}.

Figure 7-10 shows the transitions of maximum load torque $[T_{brake}]_{max}$ and the minimum rotational speed n_{min} for W_{ring}. The experimental results of single circular cylinder blade wind turbine with dual ring-plate shown in Fig. 7-6 are plotted for the comparison. $[T_{brake}]_{max}$ increased with increasing W_{ring} in the range of $5 \leq W_{ring} \leq 20$mm but decreased sharply at $W_{ring} = 30$mm. Comparing the result with that of the single circular cylinder blade, the tendency that $[T_{brake}]_{max}$ increased with increasing W_{ring} in $5 \leq W_{ring} \leq 20$mm agreed and the value of $[T_{brake}]_{max}$ of the stepped circular cylinder blade exceeded that of the single circular cylinder blade. It means that the effect of the stepped circular cylinder blade which removing the unnecessary region for the lift force generation by NV was confirmed. n_{min} of the stepped circular cylinder blade decreased with increasing W_{ring} in $5 \leq W_{ring} \leq 20$mm and increased sharply at $W_{ring} = 30$mm. That is, n_{min} decreased when $[T_{brake}]_{max}$ increases. This tendency agreed with the transition of $[T_{brake}]_{max}$ and n_{min} for the single circular cylinder blade. Comparing the value of n_{min} with the result of the single circular cylinder blade, n_{min} of the stepped circular cylinder blade was 10-20rpm larger than that of the single circular cylinder blade at $10 \leq W_{ring} \leq 20$mm, and was 50-70 rpm smaller at $W_{ring} = 5, 30$mm.
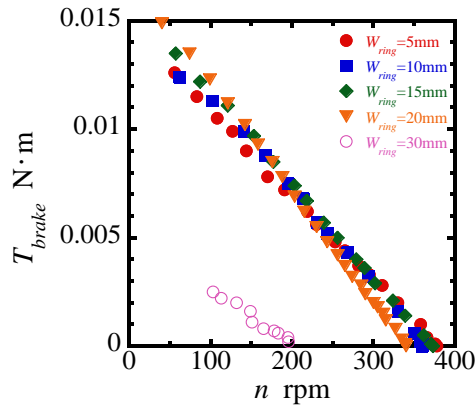
Fig. 7-9 Load torque vs. rotational speed at $U = 10$m/s through loaded experiments for each value of stepped circular cylinder blades wind turbine with dual ring-plate.

(a) $[T_{brake}]_{max}$ vs. gap between ring-plates

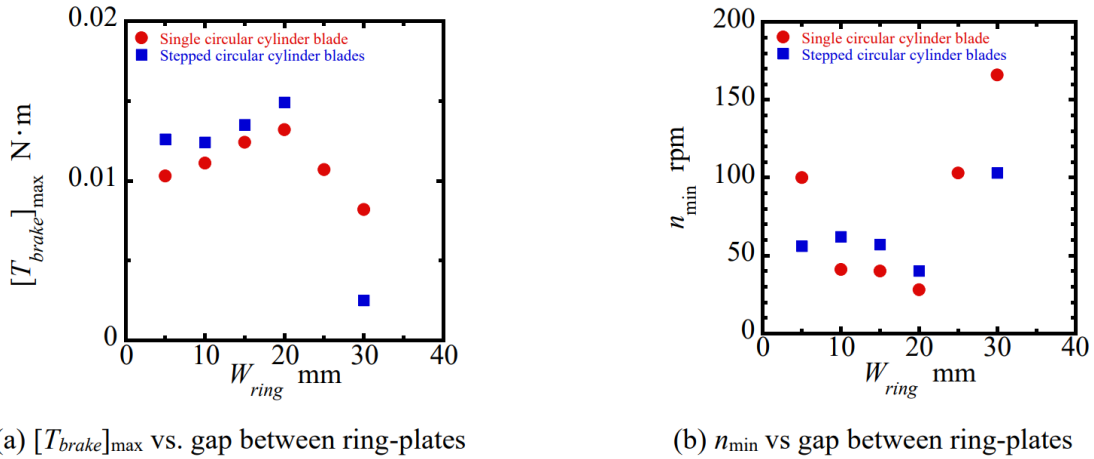(b) n_{min} vs gap between ring-plates

Fig. 7-10 Effect of gap between ring-plates on maximum load torque and minimum rotational speed.

7.3.2   Influence of blade number at a fixed gap between ring-plates

From the results of the single circular cylinder blade and the stepped circular cylinder blade with $N = 2$, W_{ring} = 10mm which is arbitrary determined and W_{ring} = 20mm where $[T_{brake}]_{max}$ was maximum were adopted and the effect of the blade number N is examined.

Figure 7-11(a) shows the relationship between the rotational speed n and increasing flow velocity U in each blade number N obtained through the un-loaded experiments for the stepped circular cylinder blade wind turbine with dual ring-plate of W_{ring} = 10mm. n increased proportionally to U in each N. The minimum wind speed at which the stepped circular cylinder blade rotates steadily U_{min} was U_{min} = 3m/s at $N = 2$, and U_{min} = 2m/s which is the minimum flow velocity measured by the wind tunnel at the other N. The significant difference in n at the given U was not observed in $4 \leq N \leq 8$. Fig. 7-11(b) shows the relationship between n and U in each N for the stepped circular cylinder blade wind turbine with dual ring-plate of W_{ring} = 20mm.

126

The tendencies of n which increases with the increase of U and the value of U_{min} at each N agreed with the results of W_{ring} = 10mm. The slight difference in n in the given U was confirmed in the range of $U \geq$ 8m/s in $4 \leq N \leq 8$.

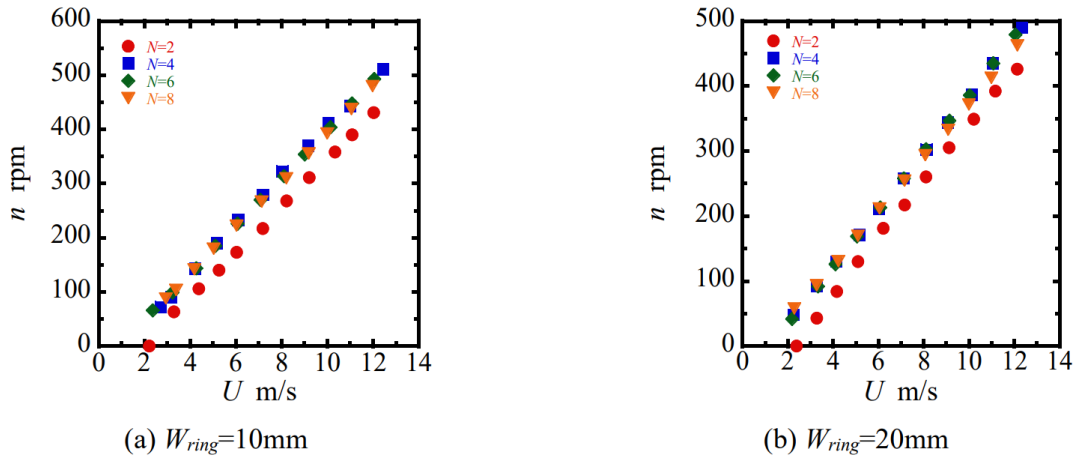(a) W_{ring}=10mm   (b) W_{ring}=20mm

Fig. 7-11 Rotational speed vs. flow velocity through un-loaded experiments for each blade number of stepped circular cylinder blades wind turbine with dual ring-plate. d = 20mm, l_P = 15mm, N = 2-8, s/d = 0.35.

Figure 7-12(a) shows the relationship between T_{brake} and n at U = 10m/s for N obtained through the loaded experiments for the stepped circular cylinder blade wind turbine with dual ring-plate of W_{ring} = 10mm. T_{brake} increased linearly with the decrease of n in each N. In $4 \leq N \leq 8$, the significant difference in T_{brake} was not observed around $n > $ 350rpm, but this difference increased with the decrease of n, and the maximum value of T_{brake} at N = 8 was about twice of that of N = 4. The minimum rotational speed which the maximum load torque ($[T_{brake}]_{max}$) is obtained was about 20-50rpm at each N. Fig. 7-11(b) shows the relationship between T_{brake} and n in each N for W_{ring} = 20mm. Similar to the result for W_{ring} = 10mm, T_{brake} increased linearly with the decrease of n in each N. In $2 \leq N \leq 6$, the maximum value of T_{brake} increased and the minimum rotational speed decreased with the increase of N.
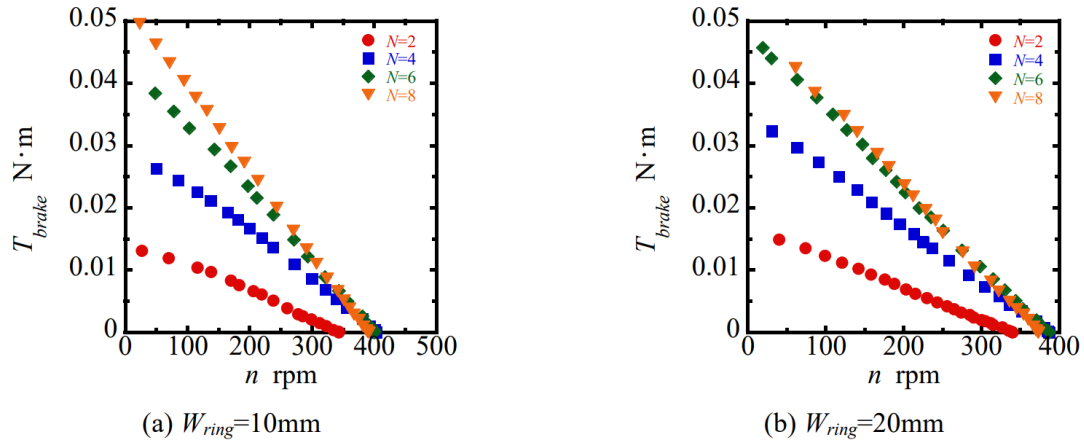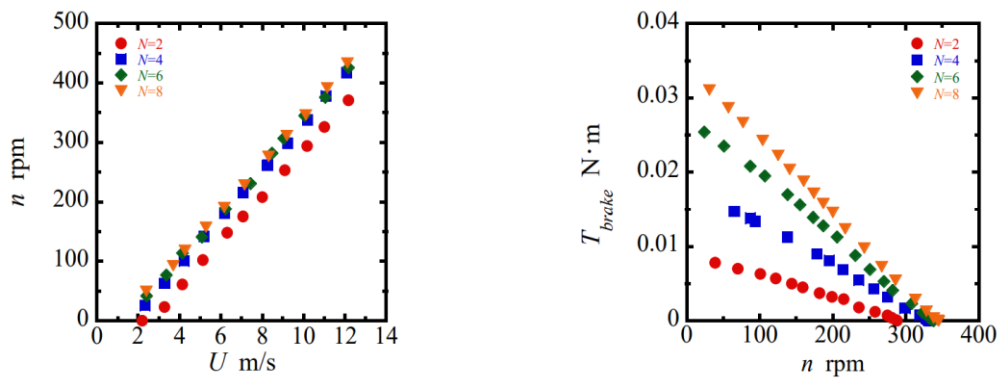
(a) W_{ring}=10mm

(b) W_{ring}=20mm

Fig. 7-12 Load torque vs. rotational speed at U=10m/s through loaded experiments for each blade number of stepped circular cylinder blades wind turbine with dual ring-plate. d = 20mm, l_P = 15mm, N = 2-8, s/d = 0.35.

Figure 7-13 shows the relationship between n and U and the relationship between T_{brake} and n in each N for the stepped circular cylinder blade wind turbine with the downstream single ring-plate with D = 155mm and W = 20mm and the stepped circular cylinder blades with the protruding length of l_P = 15mm are placed. n increased proportionally to U in each N. The minimum flow velocity at which the stepped circular cylinder blade rotates steadily U_{min} was U_{min} = 3m/s at N = 2 and U_{min} = 2m/s at other N. The difference in the rotational speed at the given U was not confirmed in $4 \leq N \leq 8$. T_{brake} increased linearly with the decrease of n for all N. The maximum values of T_{brake} and T_{brake} for the given n increased with the increase of N. The minimum value of the rotational speed (n_{min}) was less than 50 rpm in each N except at N = 4.


(a) Rotational speed vs. flow velocity through un-loaded experiment

(b) Load torque vs. rotational speed at U=10m/s through loaded experiment

Fig. 7-13 Results of loaded and un-loaded experiments for stepped circular cylinder blade wind turbine with single ring-plate. d = 20mm, l_P = 15mm (l = 60mm), N = 2-8, W = 20mm, D = 155mm, s/d = 0.35.

Figure 7-14 shows the relationship between n and N at $U = 10$m/s at the un-loaded experiments and the relationship between $[T_{brake}]_{max}$, n_{min} and N at $U = 10$m/s at the loaded experiments in three conditions for the ring-plate (dual ring-plate of $W_{ring} = 10$, 20mm and single ring-plate of $W = 20$mm). For n at un-loaded experiments in Fig. 7-14(a), the maximum difference of about 20rpm was confirmed in each N at the two conditions of the dual ring-plate. n of the dual ring-plate was larger compared to that of the single ring-plate in all N, and they were 1.2 times for $N = 2$ and 4, 1.18 times for $N = 6$, and 1.08 times for $N = 8$. These increase rates show that the effect of the dual ring-plate on n appears in smaller N. For the transition of n with the increase of N in each condition of the ring-plate, n slightly decreased with the increase of N at $N \geq$ 4 when the dual ring-plate is placed, and n decreased with the increase of N when the single ring-plate is placed. For $[T_{brake}]_{max}$ at loaded experiments in Fig. 7-14(b), the values of $[T_{brake}]_{max}$ at $W_{ring} = 20$mm was larger than those at $W_{ring} = 10$mm except at $N = 8$. $[T_{brake}]_{max}$ of the dual ring-plates was larger than that of the single ring-plate in all N, and they were 1.7 times at $N = 2$ ($W_{ring} = 20$mm), 2.2 times at $N = 4$ and 6 ($W_{ring} = 20$mm), and 1.6 times at $N = 8$ ($W_{ring} = 10$mm). These increase rates showed that $[T_{brake}]_{max}$ increases about twice by installing the dual ring-plate in all N, and the effect of the dual ring-plate is larger compared with n at the un-loaded experiments. $[T_{brake}]_{max}$ increased almost linearly with the increase of N in all conditions of the ring-plate except for the decrease at $N = 8$ at $W_{ring} = 20$mm. For the result of the single ring-plate, the increase rates of $[T_{brake}]_{max}$ compared with at $N = 2$, were 1.9 times at $N = 4$, 3.3 times at $N =$ 6, and 4.0 times at $N = 8$, therefore, $[T_{brake}]_{max}$ increased with the same rate as the increase rate of N. Also, in the result of the dual ring-plate of $W_{ring} = 10$mm, the increase rates of $[T_{brake}]_{max}$ compared with at $N = 2$, were 2.0 times at $N = 4$, 2.9 times at $N = 6$, and 3.8 times at $N = 8$, and $[T_{brake}]_{max}$ also increased with the same rate as that of N. In the result of the dual ring-plate of $W_{ring} = 20$mm, the increase rates of $[T_{brake}]_{max}$ compared with at $N = 2$, were 2.2 times at $N = 4$, 3.1 times at $N = 6$, and 2.9 times at $N = 8$, and $[T_{brake}]_{max}$ increased with the same rate as that of N expect at $N = 8$. These results of the increase rate of $[T_{brake}]_{max}$ indicated that the driving torque by the lift force of NV increases equally as the increase rate of N at the dual ring-plate of $W_{ring} = 10$ and 20mm. The decrease of $[T_{brake}]_{max}$ at $N = 8$ and $W_{ring} = 20$mm is thought to be due to the interference effect of the wake on the rotational motion caused by the narrow pitch distance between the stepped circular cylinder blades on the inside ring-plate. As shown in Fig. 7-14(c), n_{min} at W_{ring} $= 20$mm decreased with the increase of N, and then increased at $N = 8$. However, the systematic change of n_{min} for the increase of N was not observed in the other conditions, and the effect of the installation of the dual ring-plate was not confirmed.
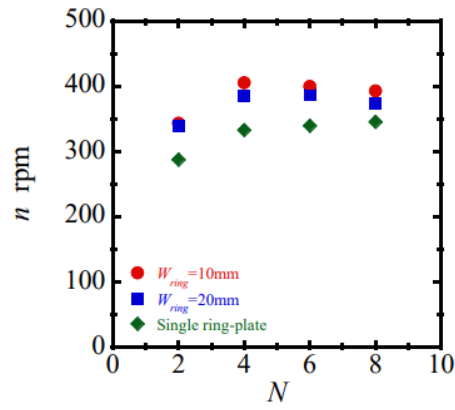
(a) *n* vs *N*
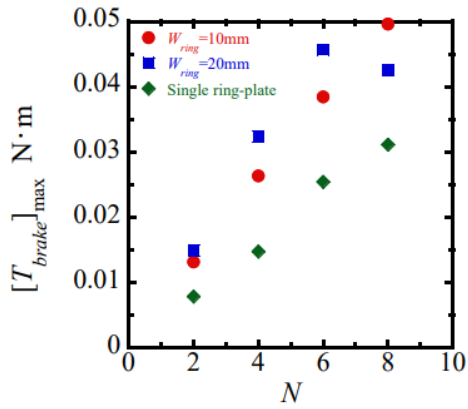
(b) [*T*$_{brake}$]$_{max}$ vs. *N*
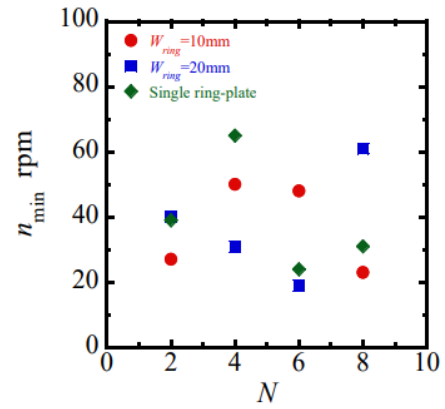
(c) *n*$_{min}$ vs *N*

Fig. 7-14 Effect of number of stepped circular cylinder blade on rotational speed at $U = 10$m/s, maximum load torque and minimum rotational speed.

130

7.4 Effect of dual ring-plate on power coefficient of stepped circular cylinder blade wind turbine

In order to evaluate the performance of the wind turbine, the power coefficient C_p is determined using the results of loaded experiments. The power coefficient is defined by the following equation as same in Chapter 4 and 5,

$$C_p = \frac{\omega T_{brake}}{0.5\rho AU^3} \qquad (7-1)$$

where, ω (= $2\pi n/60$) is the angular velocity of the turbine, and A (= $\pi l_{total}^2/4$) is the swept area when the cylinder blades rotate.

Figure 7-15 shows the relationship between C_p and the tip speed ratio of the cylinder blade λ {= $\pi n l_{total}/(60U)$} in each N for the stepped circular cylinder blade wind turbine with the dual ring-plate with $W_{ring} = 10, 20$mm. C_p is the product of the load torque T_{brake} and the rotational speed n which are measured in the loaded experiments. Therefore, C_p changed like an upwardly convex curve as λ changes. In the results for $W_{ring} = 10$mm shown in Fig. 7-15(a), the maximum value of C_p ($[C_p]_{max}$) increased with the increase of N. The maximum power coefficient $[C_p]_{max}$ was obtained in the range of $0.2 \leq \lambda \leq 0.26$, but systematic change of this λ with increasing N was not confirmed. The range of λ where the stepped circular cylinder blade rotates steadily was minimum at $N = 2$ and maximum at $N = 8$, and this range of λ at $N = 4$ and 6 was almost equal. In the results for $W_{ring} = 20$mm shown in Fig. 7-15(b), $[C_p]_{max}$ increased with the increase of N, similar to the result of $W_{ring} = 10$mm. λ when $[C_p]_{max}$ is obtained was $\lambda = 0.19$ at $N = 2$ and $\lambda \simeq 0.21$ at other N. The range of λ increased in the order of $N = 2, 8, 4$, and 6, so the systematic change with the increase of N was not confirmed. Fig. 7-16 shows the relationship between C_p and λ in each N for the stepped circular cylinder blade wind turbine with the single ring-plate of $W = 20$mm and $D = 155$mm. C_p changed like an upwardly convex curve as λ changes and $[C_p]_{max}$ increased with the increase of N. λ when $[C_p]_{max}$ is obtained was in the range of $0.16 \leq \lambda \leq 0.19$ and the range of λ where the stepped circular cylinder blade rotates steadily increased with the increase of N.

Figure 7-17 shows the transition of $[C_p]_{max}$ with increasing N for the stepped circular cylinder wind turbine at the three conditions of the ring-plates (dual ring-plate of $W_{ring} = 10, 20$mm, and the single ring-plate of $D = 155$mm, $W = 20$mm). $[C_p]_{max}$ increased with the increase of N in any conditions of ring-plate. In the results of dual ring-plate of $W_{ring} = 10$mm and $W_{ring} = 20$mm, the values of $[C_p]_{max}$ were almost equal in each N except $N = 8$. Comparing the results of the dual ring-plate and single ring-plate, $[C_p]_{max}$ of the former was larger than that of the latter for all N, the former were 1.6 times at $N = 2$ ($W_{ring} = 20$mm), 1.7 times at $N = 4$ ($W_{ring} = 20$mm), 1.5 times at $N = 6$ ($W_{ring} = 20$mm), and 1.4 times at $N = 8$ ($W_{ring} = 10$mm) as large as the latter, respectively. These comparison results showed that even if the NVs generated on the wind turbine is doubled by the dual ring-plate, $[C_p]_{max}$ increases less than double. In order to evaluate the trend of increase of $[C_p]_{max}$ when the number of NVs formed is doubled by using different methods, $[C_p]_{max}$ at $N = 2$ in the single ring-plate is compared with $[C_p]_{max}$ at $N = 4$ in the single ring-plate and $[C_p]_{max}$ at $N = 2$ in

the dual ring-plate (W_{ring} = 20mm). $[C_p]_{max}$ increased 2.2 times for N = 4 in the single ring-plate and 1.6 times for N = 2 in the dual ring-plate (W_{ring} = 20mm), i.e., $[C_p]_{max}$ was improved by doubling of N in the single ring-plate. On the other hand, $[C_p]_{max}$ at N = 4 in the single ring-plate is compared with $[C_p]_{max}$ at N = 8 in the single ring-plate and $[C_p]_{max}$ at N = 4 in the dual ring-plate (W_{ring} = 20mm). By the doubling of these stepped circular cylinder blades and the installation of the dual ring-plate, the formation number of NVs were doubled and $[C_p]_{max}$ increased 1.9 times at N = 8 in the single ring-plate and 1.8 times at N = 4 in the dual ring-plate (W_{ring} = 20mm), i.e., the increase rate of the two $[C_p]_{max}$ was almost equal. These comparisons of experimental results indicate that the doubling of the NVs by attaching the dual ring-plate is effective for improving the performance at large N.

The increase rates of $[C_p]_{max}$ of the single ring-plate compared with at N = 2, they were 2.2 times at N = 4, 3.4 times at N = 6, and 4.3 times at N = 8, and $[C_p]_{max}$ increased more than the increase rate of N. Also, in the dual ring-plate of W_{ring} = 10mm, the increases rate were 2.4 times at N = 4, 3.3 times at N = 6, and 3.7 times at N = 8 compared with N = 2. In addition, at W_{ring} = 20mm, the increases rate were 2.3 times at N = 4, 3.1 times at N = 6, and 3.2 times at N = 8 compared with N = 2 and $[C_p]_{max}$ increased more than the increase rate of N expect N = 8.
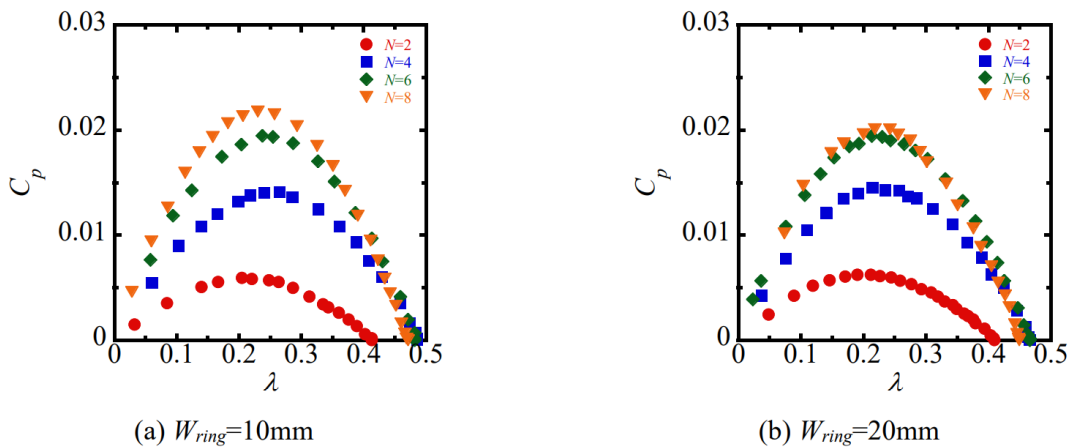

(a) W_{ring}=10mm   (b) W_{ring}=20mm

Fig. 7-15 Power coefficient vs. velocity ratio each blade number of stepped circular cylinder blades wind turbine with dual ring-plate. d = 20mm, l_P = 15mm, l_{total} = 230mm, N = 2-8, s/d = 0.35.
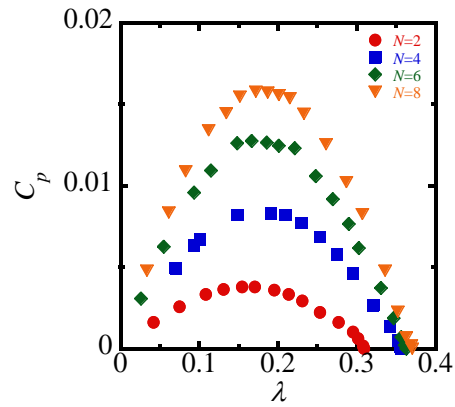
Fig. 7-16 Power coefficient vs. velocity ratio of for each blade number of stepped circular cylinder blades wind turbine with single ring-plate. $d = 20$mm, $l_P = 15$mm, $l_{total} = 205$mm, $N = 2$-8, $s/d = 0.35$.
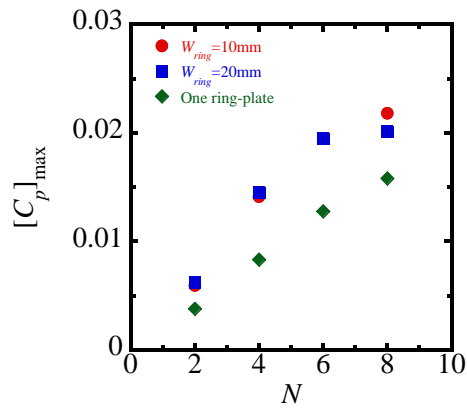

Fig. 7-17 Maximum power coefficient vs. blade number of stepped circular cylinder blades for each configuration of ring-plate.

7.5　Conclusions

In this chapter, in order to improve the performance of cylinder blade wind turbines, the double downstream ring-plate with a width of $W = 20$mm is installed on the single and stepped circular cylinder blade wind turbine, and the effects of the distance between the two ring-plates (W_{ring}) and the blade number (N) of the stepped circular cylinder blade on the rotation, output torque, and the performance characteristics were investigated. The conclusions obtained from the experimental results and discussion are shown below.

1. For both single and stepped circular cylinder blade wind turbines with dual ring-plate, the optimum gap between the two ring-plate, where the maximum load torque $[T_{brake}]_{max}$ was obtained, was about one-cylinder blade diameter ($W_{ring} = 20$mm).

2. For both single and stepped circular cylinder blade wind turbines with dual ring-plate, the results of n and $[T_{brake}]_{max}$ of the dual ring-plate exceeded those of the sing ring-plate of $W = 20$mm in almost all W_{ring}, but compared with the result of $W = 40$mm, the effect of the dual ring-plate was limited to $[T_{brake}]_{max}$ at the certain W_{ring}.

3. In each N of the stepped circular cylinder blade, the effect of the dual ring-plate on n at un-loaded experiments was not confirmed, but $[T_{brake}]_{max}$ became 2.2 times larger at maximum than that at single ring-plate of $W = 20$mm placed.

4. In the experiments in this chapter, the effect of the installment of dual ring-plate on the increase in the maximum power coefficient $[C_p]_{max}$ did not exceed the effect of doubling the blade number in the single ring-plate. However, it was also shown that the doubling of the necklace vortices (NVs) by the installation of the dual ring-plate could improve the performance of the wind turbines at large N.

8. Conclusions

The conclusions from the experimental results in Chapters 3-7 are summarized, and the basic knowledge for improving the performance of circular cylinder blade wind turbines is clarified. The performance of the circular cylinder blade wind turbines obtained in the above chapters is compared with that of conventional wind turbines, and the status and prospects of the circular cylinder blade wind turbine in wind power generation are clarified.

8.1   Summary of conclusions in each chapter

The objective of this research work was to develop the circular cylinder blade wind turbine driven by the steady lift force of the longitudinal vortex (LV). In order to achieve this objective, the following three experiments were conducted.

1. Visualization of the necklace vortex (NV) at the intersection of the circular cylinder blade and the ring-plate.

2. Investigations of the rotation and output torque characteristics of the circular cylinder blade wind turbine for various structural parameters, and the characteristics of axial drag force acting in the mainstream direction.

3. Suggestions of the configurations of circular cylinder blade and ring-plate for the enhance methods of performance of the wind turbines.

The circular cylinder blade wind turbines are classified into two types: single circular cylinder blade and stepped circular cylinder blade wind turbines. A single long cylinder blade was adopted for the single circular cylinder blade wind turbine and the influence of the basic structural parameters on each characteristic were investigated. The stepped circular cylinder blades, that had thick portions for only the effective regions for the lift force generation by NV and this for others, were adopted to the stepped circular cylinder blade wind turbine and the mechanism for improving the performance were investigated. All experiments were conducted in the test section of the wind tunnel, and measuring devices were attached to the end of the driving shaft of each wind turbine, depending on the objects to be measured. Conclusions to the objectives in each chapter are as follows:

In Chapter 3, the process of formation and shedding of the NV at the intersection of the rotating circular cylinder blade and ring-plate was observed by the smoke visualization. Using the images of NVs obtained from visualizations, the cross-section diameter of the NV was determined. By the evaluation of the cross-section diameter of the NV, the influence of the experimental conditions such as the diameter of the circular cylinder blade and the pitch between the circular cylinder blades on the formation of the NV was investigated. The NV was stably formed in the gap on the opposite side of the moving direction of circular cylinder blade, which agreed with the results of the numerical analysis. The cross-section diameter of the NV was highly dependent on the diameter of circular cylinder blade and increased almost as much as the increase rate of the circular cylinder blade diameter. On the other hand, the effect of increasing the number of the circular cylinder blades on the cross-section diameter of NV was small, but the increase in the blade number induced ununiformity in the size of cross-section diameter of NV.

In Chapter 4, the steady lift forces acting on the single circular cylinder blade wind turbine under forced rotation at constant flow velocity were measured, and the relationship with the relative attack angle was investigated. The rotation and output torque characteristics were investigated by varying the structural parameters that were considered to affect the magnitude of the lift force by the LV. The lift and drag coefficients acting on the single circular cylinder blades were calculated using the output torque

characteristics obtained by the loaded experiments. The aerodynamic force coefficient C_z acting on the single circular cylinder blade increased monotonically with the increase of the relative attack angle, which was geometrically determined by the moving velocity of single circular cylinder blade and the mainstream velocity. When C_z was negative, the single circular cylinder blade accelerated in the rotating direction when an initial motion was given. The attack angle increased with the rotational speed and when C_z reached zero, the acceleration also became zero and the single circular cylinder blade rotated steadily. When the gap ratio was $s/d \geq 0.35$, C_z became negative and the single circular cylinder blade rotated steadily at un-loaded condition, but when the gap ratio was $s/d < 0.35$, the single circular cylinder blade did not rotate steadily at any flow velocity. The rotational speed n for the increasing flow velocity U was determined to be a constant α in which C_z was 0 regardless of U. The lift coefficient C_L of NV was well approximated by a decreasing linear function of the velocity ratio λ and the drag coefficient C_D against the rotation was assumed to be constant by properly defining the span wise lengths of their acting region on the single circular cylinder blade. Using the values of C_L and C_D, the relationships between n and U under un-loaded condition and between the power coefficient C_p and the velocity ratio λ were fairly well predicted for the widely varying conditions. The wide ring-plate and attachment of the flanges were shown to be promising technique to improve the performance of the wind turbine.

In Chapter 5, in the stepped circular cylinder blade wind turbine, which was thought to have a practical wind turbine configuration, the effects of the effective length l, number N and diameter d of the stepped circular cylinder blade on the rotation, output torque, and power characteristics were investigated. By setting the effective length of the stepped circular cylinder blade equal to the formation region of NV, the fluid resistance to rotation was reduced without decreasing the lift force of NV. The lift force acting on per blade was almost constant at $N \leq 8$, but decreased by the interference effect by the wake related to rotation at $N \geq 10$. This interference effect also occurred at $d = 28$ and 30 mm for $N = 8$ and at all d for $N = 10$. The instability of NV formation was induced at small rotational speeds for the large blade diameter d, leading to an increase in the minimum flow velocity which steady rotation was obtained in un-loaded experiments and an unexpected stop of rotation in the loaded experiments. The effects of the blade pitch ratio t/d on rotation and output torque characteristics were extensively investigated by combining the conditions of blade number N and blade diameter d. In the range of the pitch ratio of $t/d < 2$, the lift force by NV per stepped circular cylinder blade was reduced by the interference effect of the wake on the rotational motion of the cylinder blades. By further narrowing the range of t/d at high flow velocities, the effect of high rotation occurred, and the rotational speed of the stepped circular cylinder blade increased rapidly. From the above conclusions, $l = 60$mm and $t/d \simeq 2$ was recommended as the optimum configuration for the stepped circular cylinder blade wind turbine.

In Chapter 6, The effects of basic structural parameters such as gap ratio s/d and ring-plate width W on the axial drag force characteristics in the mainstream direction were investigated. The effects of the blade number on the drag force characteristics of the entire circular cylinder blade wind turbine and per

circular cylinder blade were clarified by the experiments with the stepped circular cylinder blade wind turbine. When the LV was formed stably behind the moving direction of the circular cylinder blade, the strong suction flow (negative pressure region) was generated between the circular cylinder blade and the downstream ring-plate, which caused a large drag force in the mainstream direction to the circular cylinder blade at the same time as the lift force. The axial drag acting on the entire circular cylinder blade wind turbine at constant flow velocity increased almost in proportion to the increase in the ring-plate width W and the blade number N. The rotational speeds of the cylinder blades increased linearly with the increase in flow velocity so that the relative attack angle α kept constant, while the axial drag force increased exponentially. The axial drag coefficient showed complex behavior in several experimental conditions. This behavior of the axial drag coefficient was considered to be related to the generation of tip vortices by the increase in rotational speed, the destabilization of the LV formation by the change in the ring-plate width at the same total blade length, and the effect of the interference of the wake on the rotational motion of the cylinder blade by the increase in the blade number.

In Chapter 7, in order to enhance the performance of the circular cylinder blade wind turbines, dual ring-plate consisted of the two different center diameter ring-plates were installed in the downstream of the circular cylinder blades and this influence on the rotation, output torque, and performance was investigated, and the effectiveness of dual ring-plate was evaluated by comparison with the case of the single ring-plate with $W = 20$ and 40mm. For both single and stepped circular cylinder blade wind turbines with dual ring-plate, the effect of gap between the two ring-plate W_{ring} was investigated and the optimum condition was determined. For both single and stepped circular cylinder blade wind turbines, the experimental results of the dual ring-plate improved those of the sing ring-plate of $W = 20$mm in almost all W_{ring}, but compared with the result of $W = 40$mm, the effect of the dual ring-plate was limited to the output torque characteristics at certain W_{ring}. The effect of blade number of the stepped circular cylinder blade wind turbine was investigated. In each N of the stepped circular cylinder blade wind turbine, the effect of the dual ring-plate on n at un-loaded experiments was not confirmed, but $[T_{brake}]_{max}$ became 2.2 times larger at maximum than that at single ring-plate of $W = 20$mm placed. The effect of dual ring-plate on the increase in the maximum power coefficient $[C_p]_{max}$ did not exceed the effect of doubling the blade number in a single ring-plate. However, it was also shown that the doubling of the NVs formation by the installation of the dual ring-plate can improve the performance of the wind turbines at large N.
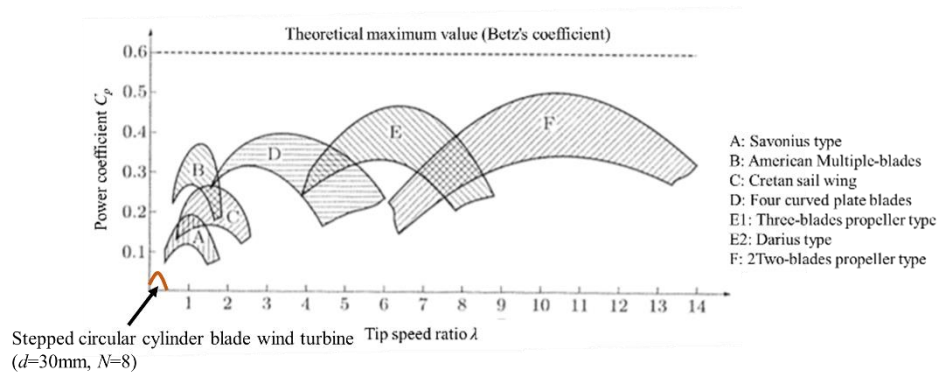
8.2 Status of circular cylinder blade wind turbines in wind power generation

The performance of the circular cylinder blade wind turbines in this research work (relationship between C_p and λ) was highest for the stepped circular cylinder blade wind turbine with the blade diameter $d = 30$mm and the blade number $N = 8$ as shown in Subsection 5.3.3 (Fig. 5-64). This condition is hereafter called to as the "maximum condition". The relationship between C_p and λ under the maximum condition is shown again in Fig. 8-1(a), which is added to the figure (Fig. 1-3(b)) showing the power coefficient of the conventional wind turbines. The torque coefficient C_q is calculated by the following Eq. (8-1) using the results of the loaded experiments of the maximum condition (Fig. 5-37), and the relationship between C_q and λ is shown in Fig. 8-1(b), which is the same figure shown in Fig. 1-3(a) adding to the torque coefficient of the maximum condition of the circular cylinder blade wind turbines.

$$C_q = \frac{T_{brake}}{0.5 \rho A U^2 l_{total}} \qquad (8-1)$$

The range of λ at the maximum condition is $0.05 < \lambda < 0.35$, and λ at the maximum C_p is 0.2, which is remarkably small compared with the conventional wind turbines. The power coefficient is also much smaller than that of conventional wind turbines. However, in this research work, the maximum power coefficient could be improved by more than 8 times by changing the structural parameters from the prototype model of single circular cylinder blade wind turbine to the optimum conditions described above (see Figs. 4-21 and 5-64). In Chapter 4, it was shown that the installation of a wide ring-plate is effective in improving the performance. Furthermore, as shown in Chapter 7, it was expected that the performance can be improved by installing the dual ring-plate. There is a lot of possibility for improving the performance of circular cylinder blade wind turbines and the methods. The torque coefficient C_q of the circular cylinder blade wind turbine decreases linearly with the increase of λ. This change in C_q is similar to that of Savonius-type wind turbines (drag force type) and multi-wing wind turbines (lift force type), and also exceeds the C_q of many conventional lift force type wind turbines.

Based on the characteristics of the circular cylinder blade wind turbine described above, and the rotational and output torque characteristics investigated in each chapter, the circular cylinder blade wind turbine is currently suited to the medium or small size wind turbine that can be installed in residential areas or the living area. It is easy to start and stop the rotation instantaneously and simply by controlling the gap between the circular cylinder blade and the ring-plate, compared with applying the brake or controlling the angle of rotor blade. And the problem for the popularization of wind turbines in residential areas can be solved by eliminating the fear of wind turbines by the low rotational speed and the absence of wind noise.

(a) Power coefficient
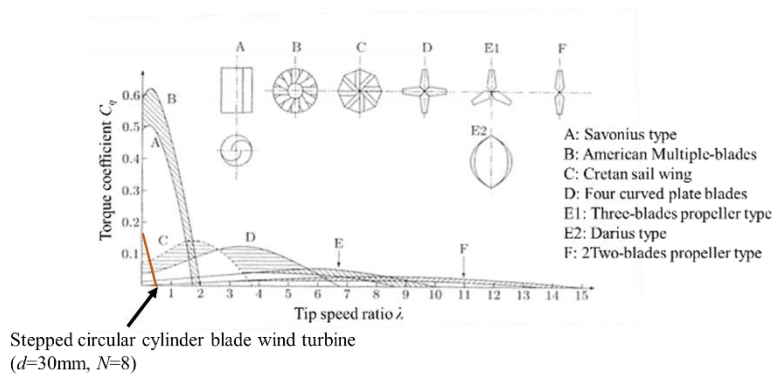
(b) Torque coefficient calculated by Eq. (8-1).

Fig. 8-1 Comparison of performance of stepped circular cylinder blade wind turbine with $d = 30$mm, $N = 8$ and conventional wind turbines.

Publications and conference data

International journal

Sakamoto, K., Hemsuwan, W. and Takahashi, T., 2021, "Development of a circular blade wind turbine driven by longitudinal vortex: Wind tunnel experiment to investigate the basic characteristics of the wind turbine using a single circular cylinder blade", Journal of Wind Engineering and Industrial Aerodynamics, Vol. 210, 104492.

Domestic journal

Sakamoto, K., Udaka, K., Hemsuwan, W. and Takahashi, T., 2021, "Development of circular cylinder blade wind turbine driven by longitudinal vortex", Transactions of the JSME, Vol. 87, No.894.

Sakamoto, K., Hemsuwan, W. and Takahashi, T., 2021, "Drag force of a circular cylinder blade wind turbine driven by longitudinal vortex", Transactions of the JSME, Vol. 87, No.894.

International conference

Sakamoto, K., Hemsuwan, W. and Takahashi, T., 2017, "Lift and drag forces on circular cylinder blades wind turbine", Proc. The 1st International Symposium on Wind and Tidal Power.

Sakamoto, K., Hemsuwan, W. and Takahashi, T., 2017, "Study on Performance Improvement of the Horizontal Axis Type Circular Cylinder Blades Wind Turbine Driven by Longitudinal Vortex", Proc. The 6th International GIGAKU Conference in Nagaoka, RD-015.

Sakamoto, K., Hemsuwan, W. and Takahashi, T., 2017, "Enhancement of efficiency of a new horizontal type turbine driven by longitudinal vortex", Proc. the 9th JSME-KSME Thermal and Fluids Engineering Conference, TFEC9-1421.

Sakamoto, K., Hemsuwan, W. and Takahashi, T., 2018, "INFLUENCE OF PITCH OF BLADES ON EFFICIENCY CHARACTERISTIC OF WIND TURBINE DRIVEN BY LONGITUDINAL VORTEX", Proc. The 17th International Conference on Fluid Flow Technologies.

Sakamoto, K., Hemsuwan, W. and Takahashi, T., 2018, "Effect of Ring Plate Configuration on a Circular Cylinder Blades Wind Turbine Driven by Longitudinal Vortex", Proc. Grand Renewable Energy 2018.

Domestic conference

Sakamoto, K., Hemsuwan, W., Yoshitake, Y. and Takahashi, T., 2016, "Performance test of a novel wind turbine propeller with circular cylinder blades driven by longitudinal vortex", Proc. the 94th Annual Conference of the JSME in Fluid Engineering Division, 0618.

Sakamoto, K., Hemsuwan, W. and Takahashi, T., 2017, "Influence of wing configuration on a circular cylinder blades wind turbine driven by longitudinal vortex", Proc. the 22nd Symposium on Power and Energy Technologies, E131.

Sakamoto, K. and Takahashi, T., 2017, "Study on performance characteristics on the vertical axis type circular cylinder blades wind turbine driven by longitudinal vortex", Proc. the 2017 Annual Conference of the JSME, J0540306.

Sakamoto, K., Hemsuwan, W. and Takahashi, T., 2018, "Influence of blade length on kinematic feature of cylinder blade wind turbine driven by longitudinal vortex", Proc. the 96th Annual Conference of the JSME in Fluid Engineering Division, OS6-2.

Acknowledgement